



Radio Controlled
SoaringDigest

July 2017

Vol. 34, No. 7



Front cover: Markus Portmann's 5.33m ASK-18. Construction photos begin on page 11 of this edition. Olympus FE-140,X-725, ISO 80, 1/1000 sec., f3.1

- 4 Contest Tips & Lessons Learned**
Paul Naton, Radio Carbon Art, picked up a few valuable lessons at the 2016 "Polecat" ALES event.
- 10 A Phil Cooke photo**
Andy Meade's PSS BAe Hawk makes a low pass.
- 11 Markus Portmann's 1:3 scale ASK-18**
Construction photos of a beautiful scale project.
- 17 Alessandro (Alex) Villa's KA-7**
Construction notes, including changes made, and flying report for the 2m Jamara all wood kit.
- 25 Dust Buster LiPo hack**
Paul Nation, Radio Carbon Art, replaces the classic shop vacuum NiCd batteries with a Lithium pack. Cool!

- Balsa Stripper and Balsa Fence** **29**
Barrie Russell describes two valuable shop tools designed by David Plumpe. Purloined from the Model Flying Hawkes Bay, New Zealand, web site <<http://www.mfhb.org.nz>>. Plans included!
 - NRL Tests Autonomous "Soaring with Solar" Concept** **32**
A U.S. Naval Research Laboratory project.
 - Identifying the flow physics and modeling transient forces on two-dimensional wings** **35**
AFRL-0250, Air Force Research Laboratory.
 - The Landing Area Penalty Rule** **91**
Gordy Stahl explains the new AMA RC soaring rule.
 - Slope candidate Northrop YA-9A** **93**
The alternative to the A-10 Thunderbolt/Warthog.
-

Back cover: Paul Marshall launches his own design 2 meter TNT for a dynamic soaring session north of Perth, Western Australia, May 2017. Photo by Gavin Tilson. Apple iPhone 6s, ISO 25, 1/2400 sec., f2.2

R/C Soaring Digest

July 2017

Volume 34 Number 7

Managing Editors, Publishers
Contributing Editor

Bill & Bunny (B²) Kuhlman
Spencer Webster

Contact

bsquared@rcsoaringdigest.com
<http://www.rcsoaringdigest.com>
Yahoo! group: RCSoaringDigest
FaceBook: <https://www.facebook.com/RCSoaringDigest/>

R/C Soaring Digest (RCSD) is a reader-written monthly publication for the R/C sailplane enthusiast and has been published since January 1984. It is dedicated to sharing technical and educational information. All material contributed must be original and not infringe upon the copyrights of others. It is the policy of *RCSD* to provide accurate information. Please let us know of any error that significantly affects the meaning of a story. Because we encourage new ideas, the content of each article is the opinion of the author and may not necessarily reflect those of *RCSD*. We encourage anyone who wishes to obtain additional information to contact the author.

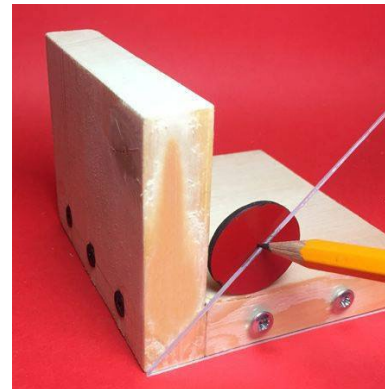
Copyright © 2017 *R/C Soaring Digest*
Published by B²Streamlines
<http://www.b2streamlines.com>
P.O. Box 975, Olalla WA 98359
All rights reserved

RC Soaring Digest is published using Adobe InDesign CS6

July 2017

In the Air

This edition of *RC Soaring Digest* includes a technical report from the Air Force Research Laboratory. It demonstrates the tremendous strides made in the areas of computational fluid dynamics, data collection and interpretation, and modeling of dynamic systems. Our hope is that readers will appreciate this material and we welcome feedback, positive or negative, on the inclusion of this paper in *RCSD*.



Aaron Donovan posted this image of an inexpensive center finder on the Balsa Model Aircraft Builders Association FaceBook page. It uses two pieces of 3/4" pine and a 45° triangle; easily made and quite accurate.

We just received word that William "Bill" Foshag passed away in late April. Bill was an aeronautical engineer employed by Fairchild and involved in Sikorsky aircraft development in the 1950s and 60s. He was also a long-time reader of *RCSD* and contributed material to our book, "On the 'Wing... Volume 2," concerning various mechanical methods for achieving rudder differential.

Our sincere thanks to Curtis Suter for the background image on the Contents page. It's very much appreciated.

Time to build another sailplane!

ALES & F5J

Contest Tips & Lessons Learned

Paul Naton / Radio Carbon Art Productions, pnatonrca@gmail.com, <http://www.radiocarbonart.com>

In 2016 I won the “Polecat,” a big two-day Altitude Limited Electric Soaring (ALES) contest held in south central Pennsylvania. Even though I’ve been flying contests for over 25 years, I learned a few valuable lessons at this event and wanted to share some tips and techniques that will help others do better in their next competition and improve their flying techniques in general. These tips should be useful even if you don’t fly electric launched gliders or compete.

For the past five years the Polecat has been the premiere North American e-soaring event with a full matrix of over 70 pilots from the U.S., Canada, and South America attending. While guys come to the Polecat for the challenging soaring, it’s really the whole roast pig BBQ dinner Saturday night they dream about.

Contest Preparation Lesson

If you want to just fly for fun, your preparations can be lax, just remember to charge your batteries and don’t forget the post-contest beer. If you want to place well however, your head has to be more in the game and detailed preparation is vital.

My prep starts with some practice the week before, and shooting some (lots) of landings as the contest will unfortunately be decided by landing points among the top pilots. A little practice against the clock will greatly focus your mind and attitude. I will even fly a few official full rounds, practicing a routine of getting the plane ready to fly, reading the air before the round starts, and having a game plan for launch.

I also start to look at the weather forecasts as they will determine which planes I might bring and how much ballast and larger motor packs I might take. This year the Polecat forecast was for hot conditions with light winds so I left the heavy planes at home and took minimal ballast for the planes I took.

A day or so before the contest, I hit the workshop and go through the gliders nose to tail with FAA Inspector-like thoroughness to find any potential failures in the airframe, linkages or the wiring/radio system. I always find an item or two that needs preventative maintenance or repair, especially after a week of landing practice which is really hard on your systems.

I first make sure the entire motor system is in good running condition. Most of the contest-losing tech issues I see others having at an event are power system related and could have been prevented easily. I’ve seen props and spinners come off, ESCs failing to initialize, loose motors and wires, and battery charging failures.

I tighten or reset the spinner collets or set screws, check the prop for damage, and torque the motor mount screws to spec. I also make sure the prop folding bands are in good shape, check the motor wire to ESC connections and the ESC to battery connections for any fatigue. Of course I also check the servos, radio, and test the altitude limiter for correct operation.

I really hate having technical issues at a contest (or even a fun fly day) and when I get to the field, I want to know that I can

follow my pre-flight routine and step up to that first round flight line not worrying about the gliders condition or performance. Pre-contest preparation is a big confidence booster for any competitor and the first step in doing well in the standings.

Why Batteries Matter Lesson

For F5J and ALES events, having the best power system battery correctly sized and charged is absolutely critical. Why? Your battery performance determines your maximum airspeed and launch angle with your chosen motor and prop size. Any loss of power to the motor lessens your ability to get to the lift or penetrate into the wind within the limited motor-run window. Winning any e-launch contest starts with good choice and management.

At this last Polecat I saw many planes launch and you could instantly hear the motor rpms start to drop off quickly, telling me their packs were weak or not fully charged.



A few pilots even launched with totally depleted packs, costing them the heat and any chance of placing for the mugs. I noticed a few pilots flying multiple heats off the same pack without re-charging; that's not a good practice unless you have a small motor and a huge pack to feed it.

A big mistake rookies make is to have lots of motor packs, but no way to know if those packs were old and past their prime and not up to a 30 second motor run without big voltage sags.

Battery Routine

I always monitor all of my motor packs overall health with proper cycling and capacity checking routines. I'll never fly a contest heat with a pack that has shown any signs of a capacity drop or rising internal resistance measurements. Older packs are for practice or sport flying only.

For the contest, I make sure I have at least two or more new high quality packs that have been cycled and tested for my primary plane. Having a newer set of packs for your back up plane is also important, your chances of using your back-up glider are very high in a two day comp.

For each contest day, I take the two best performing packs and rotate them between heats, so after the heat I can charge the pack at a 1C rate safely and have one pack always fully charged and ready to go if needed. You may have to fly back-to-back heats so one good battery is not enough!

To be really safe, I use a LiPo voltage checker before the pack goes in the plane to ensure that it is indeed fully charged. A few years back I almost flew

a fly-off heat with a mostly dead pack as in the stress of the moment I grabbed a depleted pack instead of the charged one, and only my routine of checking with the meter revealed the mistake.

If you want to learn more about how to optimize and track LiPo battery performance, I cover these subjects in detail in my Electric Sailplane Clinic #3 instructional video available at my r/c glider instructional video website, www.radiocarbonart.com.

2016 Polecat Battery Lesson Learned

I was flying my Euphoria V2 this year and the fuse only fits packs of 1200mah capacity or smaller. During the day I was using two newer 3S 1200mah Revolectrix packs for the contest that I rotated out each heat.

I hadn't considered the fly-offs though, which are three heats in quick succession with no time to charge in between launches. While I could have done a second launch on the 1200 pack, I knew that the power was going to drop off quickly as the motor in the Euphoria is a Neu 1107 with a 16-10 prop.

The only choice I had was to use a smaller 1000mah pack for the third fly-off heat, and this pack has seen many cycles! Of course the motor rpms and climb rate were noticeably less than the newer Revo packs, but fortunately for me the fly-off cut-off altitude was only 100 meters, and the slightly lower power didn't keep me from getting to the air I called located about 300 meters cross wind.

Next time I'll have three good contest packs ready in case I make the fly-offs.

Enough with the technical and preparation issues, let's discuss some thermaling and air reading, that's what gliding and contests are all about.



Basic Air Reading Mistakes Lesson

Practice, airframe preparation and battery management lead you to that moment at the flight line where you should not be thinking about your glider, but where to put it in the sky.

The thermals for the 2016 contest were just superb. Actually almost too easy to hit. I got a 10 minute warm-up flight at 8 am on the first day. Sure, there were some strong sink cycles, but the sink areas were small, and with the light winds, easy to fly through. You could not fly more than 300 meters without hitting some sort of lift.

So why were there so many heats flown when half the planes were on the ground with 3-5 minutes left in the task? These early landers were not always the Radians or the beginner pilots. There were many 4M mouldies flown by veteran pilots that just dropped out of a sky filled with lift.

I watched the thermaling action all day and lots of pilots made the same two basic thermaling mistakes over and over. First mistake was not having a game plan or a confirmed air read before the launch window opened; they just launched upwind with the pack hoping to hit lift. Second mistake was not reading the air well once you hit your launch altitude, and not making a quick decision to fly elsewhere to find a thermal if the initial launch location at motor cutoff was not working out.

Lets discuss the first thermaling mistake and what you should do to correct it.

Like any man-on-man contest, you have some time before launch to look around and try to determine where the closest thermal is and if you can still get to it by the time the heat launch window opens. The Saturday Polecat conditions were a bit odd — huge lift was all around, but very few ground signs presented with minimal wind shifts and velocity changes, ground signs which usually indicate thermal locations and movements. The only sure clues to thermal location were a few Buzzards way up high and moving out fast.

I think I had only one sure air read from a ground sign all day, and that thermal was way downwind and off field by the time the heat started. The lift “threshold” was a bit high the first day, the threshold describing the minimal altitude required to be able to take a thermal out. It was just about impossible to thermal out below 150' for most of the day, as lots of pilots found out the hard way.

So with the lack of ground signs and a low thermal threshold, you were going to have to get off-field and find a thermal on the way up or right after motor cut-off. My game plan for most of the day was to read the plane on the way up, and not rely on ground reads at all. That plan worked every time.

After the launch horn, my plan was to fly out to the higher ground areas around the field and read the planes drift and climb rate as I gained altitude under power. My Euphoria has a bit of extra power, so I use that speed to go out and slowly climb



through as much of the surrounding air space as I can sampling the amount of drift I’m seeing on the plane and noting any areas of increased climb rate or angle. I’ll turn and change directions as needed to confirm a thermal read I might be getting.

For ALES you can use the full 30 seconds of powered flight to advantage and I have a count down timer set on my radio so I know how much time is left on the motor regardless of altitude reached. I’d like to have the plane right at the cutoff altitude at 30 seconds and hopefully in the thermal or darn close to it as glider bleeds energy after motor cutoff.

In the new F5J class, you still have the full 30 seconds of motor if you need it, but you get a better score the lower your launch altitude is. This low-launch altitude goal means your air calling and glider reading skills are even more important than with ALES.

If I read the planes responses correctly on launch, the thermal will be within a 100 meter circle from my max altitude point and I’ll just start a search pattern to find the best lift, and try to find it as quickly as possible. If I don’t find the thermal I was looking

for or it turns out to be too weak, I'll just go to my fast flight mode and fly off to another part of the sky without hesitation. I'll give myself 30 seconds or less to find lift after motor cutoff, otherwise I will get the heck out of that area and find another thermal. The faster you make your decisions on where to go, the better.

So what is this drift attitude you use to read the air on the way up the launch? I cover this advanced thermaling subject in full detail in my latest two hour instructional video the Thermal Soaring Master Class, but here is a brief description.

Reading the drift angle is a technique of finding the possible location of a thermal by watching how the glider drifts or yaws off course when influenced by the inflow currents around a thermal. A glider flying through a thermal inflow wind shift will tend to yaw the tail towards the thermal. Seeing and interpreting the subtle changes in your course angle while in flight is a hard skill to learn, but it's one of the best ways to find new lift in the absence of any ground signs or other lift indicators. I used drift indicators to find my first thermal in about 75% of my heat launches at the Polecat. Often I could read the whole pack of planes launching and could see how they all reacted to a nearby strong thermal by drifting across the thermal inflow wind shift. The Thermal Master Class video teaches you how to read the drift angles to find a new thermal core.

Move Your Butt Quickly Lesson

The second thermaling mistake is reading your plane effectively after motor shut off and not deciding to move away from sink quickly enough.

If you have no idea where that first thermal is and you just launched straight up wind, and at 20 seconds you hit 200 meters, you've wasted 10 seconds that you could have spent flying through more of the thermal air space looking for lift. Lots of pilots would execute this exact plan, hoping to find lift right after motor cutoff, then not deciding fast enough to move out of the area when they realized they launched into an area of sink.

I saw this scenario play out over and over again at this contest as four or five planes would begin circling in the general area of the upwind altitude cutoff height, not even knowing if they were in lift or sink. They would all lose altitude together, though one might luck into some lift and start to climb. Most would just loiter in the same area hoping to hit "the big one" until they got too low to be able to look elsewhere. Down in five minutes with lift everywhere. Herd mentality and not making a quick decision to move elsewhere when not gaining altitude.

You must read your own plane first and ignore the crowd. The crowd is only good for clues to new lift if the crowd is in different airspace. If your glider does not want to circle or feels dead on pitch, get out of that area fast, you will have plenty of altitude at 200 meters to do two big search patterns across the entire field. If you move out of sink quickly, your chances of getting your 10 minutes goes up fast. The thermals at this Polecat were everywhere, and even if your glider was of low performance, if you just flew a short distance away from neutral air or sink, you were bound to find lift. There was no excuse for not getting 10 minutes from 200 meters up no matter what type of glider you flew.

Getting Down Safe Lesson

As our electric gliders are getting lighter and lighter, they do have their structural limits and you have to keep that in mind in stronger lift conditions. I spent most of my rounds trying to safely dump altitude as I was launching into big lift right off and was high enough in a few minutes to get my ten. My Euphoria has a stout airframe for an F5J model, but it gets bendy at higher speeds and with the aft CG I like to fly at, I have to watch the airspeed and unplanned pitch departures as the airframe bends. There were a few "boomers" on Sunday, I was in full camber #3 and the Euphoria was still screaming and climbing like a rocket. I've got the small and light MKS 6100 HVs controlling everything on this big 4 meter glider, and it was a real job to keep the ship from over-speeding. At around 60 mph I was losing pitch



control as the boom flexed and twisted going through the violent lift. Just had to be conservative with the speed until I got out of the lift and was able to work my way down safely and hit the landing tape without blowing up anything.

Landing Too Early Lesson

The only big mistake I made all weekend was to drop about 20 seconds off an otherwise perfect flight. How did I do that?

I was killing time over the field with about a minute 30 seconds to go in the round. I was doing big circles staying up wind of the tape and out of the incoming traffic. Lift was everywhere and it was easy lift even at 100'.

At 45 seconds, I turned left to position the plane for my usual pattern entry. Then with 40 seconds left, the air changed, and changed drastically. I could barely turn, the sink was coming in hard, the wind shifted, and I was suddenly way lower than I wanted to be and far from the tapes! At 30 seconds left I was at 10' high and still out over the wheat field which was a Zero heat score if touched.

I knew I was going to be way early. I had to make the field first, then decide if I could make the tape and salvage some landing points.

I had just enough energy to get back on field, line up the tape and hit a perfect 50 landing. Just I was 20 seconds early! That mistake in reading the local field conditions cost me the Sunday daily first place mug and three positions on the board.

Lesson Learned: I was a little too busy with spotting traffic and visualizing a landing pattern to notice how strong the sink was at the other side of the field. I then was late by a few seconds in adjusting my speed and altitude to the sinking air. I should have noticed the changing air sooner and put some extra altitude in the bank before setting up for the last 30 second pattern. A basic mistake in situational awareness.

I still won the fly-offs and got the overall trophy win despite this big error.

Don't Worry About Making Mistakes Lesson

Those who take the risks of making mistakes learn the most. Try new tuning set ups, make that crazy thermal location prediction and see if it works. Launch low, land early a lot, don't give up on that ragged little streak of lift. Walk for your plane once in a while. Don't always fly in perfect conditions.

I'm happy to answer any questions you might have about any of these subjects. Contact me the usual ways or through the radiocarbonart.com website.

Here's a link to watch a short HD video I shot that gives you a taste of the action at the 2012 Polecat ALES event:

<https://youtu.be/55PuCcke1a4>





BAe Hawk low pass

A PSS BAe Hawk, built by Matt Jones from the popular Andy Conway plans. 34" span with an AUW of ~2lb, this fully built up model has a sporty performance on the slope with 2 channel R/C controlling ailerons and an all-moving tailplane. The model is now owned by Andy Meade, and it is

Andy at the controls when the photo was taken on 17th April 2016 – a fast low run towards the end of a fantastic weekends flying on the Great Orme. Photo by Phil Cooke – Power Scale Soaring Association, <<http://www.pssaonline.co.uk>> for more information on this event. Canon EOS 7D, ISO 320, 1/1600 sec., f5.6, 220mm

Markus Portmann's 1:3 scale ASK-18

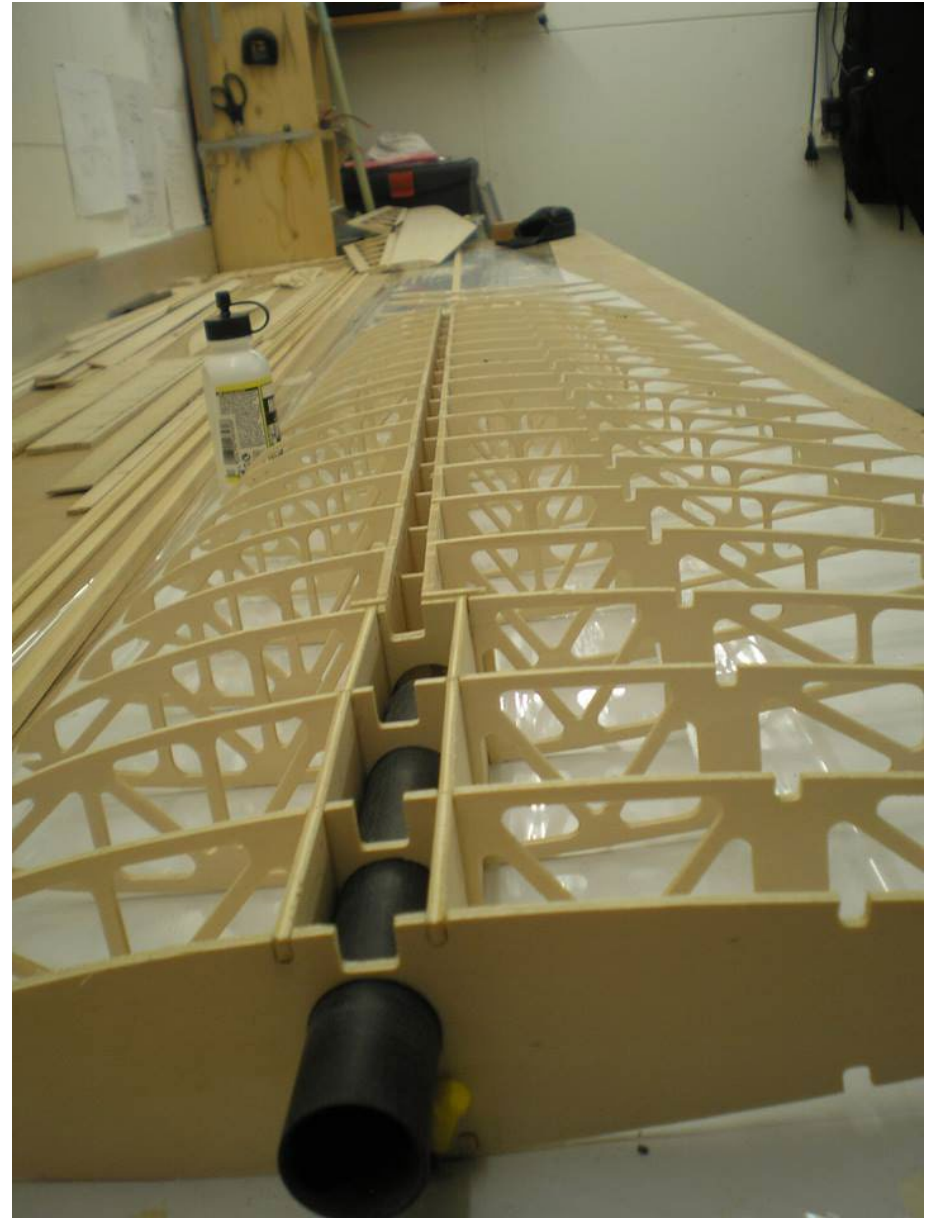


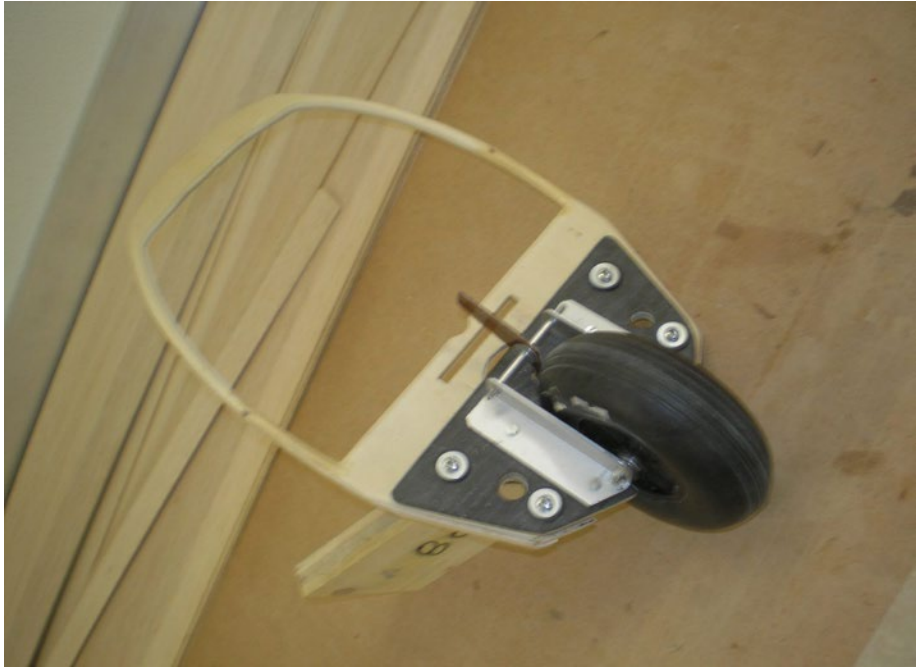
Here are a few pics of the construction and on the airfield.

The Schleicher ASK-18 had a steel tube fuselage and wooden wings spanning 16 meters. My model spans 5.33 meters and weighs 11.3 kg. The fuselage is (sadly) fiberglass, but has imitation steel tubing in the cockpit section.

Best greetings from Switzerland!

Markus, trumapo@kfnmail.ch











RC
SD

KA-7 Rhönadler



Alessandro (Alex) Villa, filotto78@gmail.com

Two years ago, I was looking for a new small kit to build during the winter season. A small “scale” glider, because the intent was to test some scale techniques that I would like to adopt on the actual model I’m building (Aeronaut Mu 13 Bergfalke).

After some nights spent in front of Google and forums I decided to buy the Schleicher KA-7 Rhönadler from Jamara. It’s a laser cut wooden kit that I found at a reasonable price in Germany.

No big deviations have been made from the supplied building instructions, but I did make few changes when it came to the fuselage.

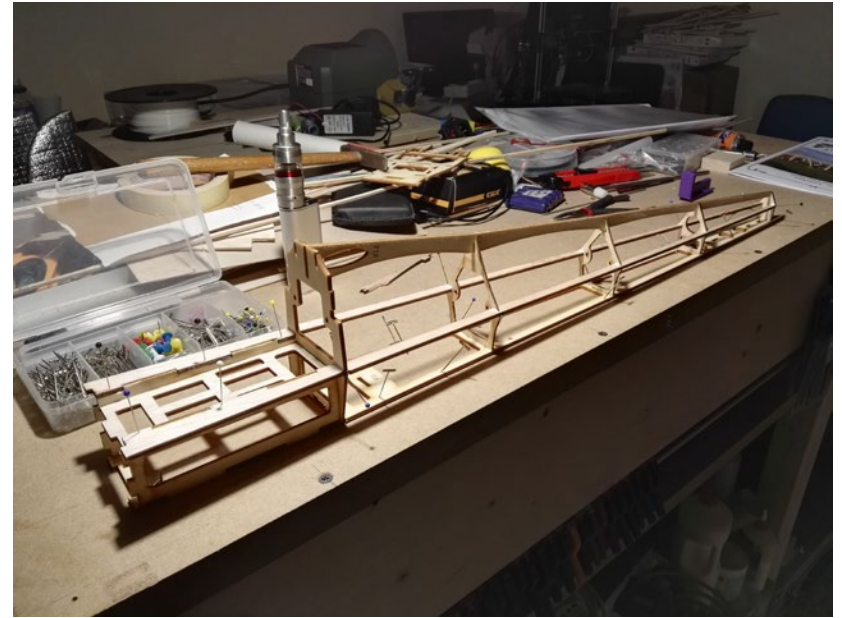
The first one concerns the wing joiner carbon fiber rod. The original idea was to not provide any case for it, not in the wing root area, not in the fuselage, leaving the wing joiner free to float in the fuselage. I didn’t like this solution, so I used an aluminum tube in both wing and fuselage.

I’m not sure how Jamara intended to keep the wings in place, but I decided to use the same aluminum tube to create a passage for the spring I used to keep the wings against the fuselage.

The second one was the modification of the canopy frame front former and the removal of its horizontal support. It was exactly in front of the instrument panel I intended to add. Very ugly and not scale-like. I decided that the canopy frame would have been strong enough even without these items and I choose to remove them.

The third was about the tow release, not foreseen in the original kit. I found a small area inside the fake skid, among two fuselage formers. I made the necessary servo fixture and then I covered the recess with a suitable plywood plank secured by small countersunk screws.

The last fuselage modification was about the tail command. Originally intended for two unaesthetic bowden cables, for





the rudder I decided to use the classic pull-pull cables, while for elevator I preferred to use the same method already used on my Grunau Baby. A small threaded rod hinged to a rigid wooden dowel coming from the servo and secured to the hole in the elevator through two M3 nuts.

All the other modifications concerned the scale details.

With my 3D printer I printed head and hands of the pilot. The body was made of soft foam. At the end I had fun by improvising myself to be a tailor and then I provided the clothes as well. Before the maiden flight I gave the head to a friend of mine who is a professional decorator. Excellent result if you think that the head is less than 1 inch tall...

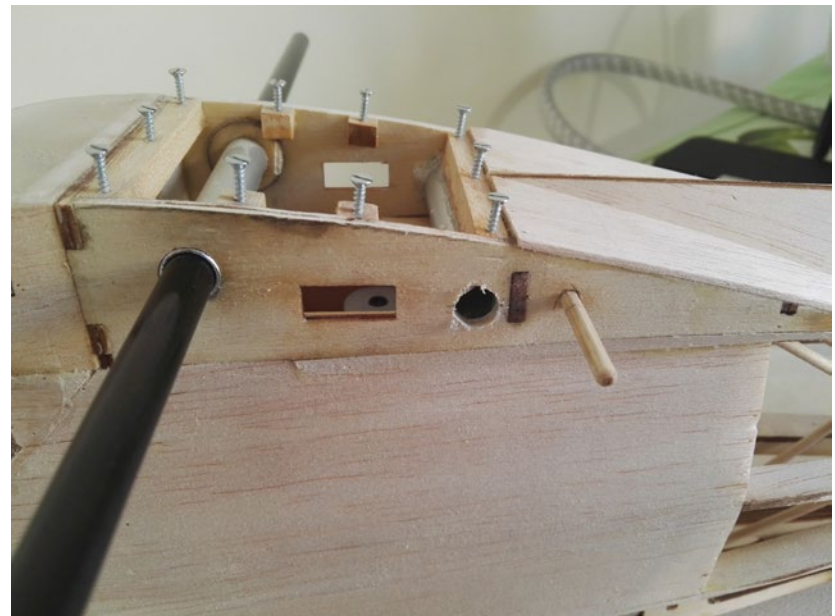
I used my Silhouette Cameo to cut out the fake reinforcement of sewing wing covering tissue. In order to be as "scale" as possible, below the sewing reinforcement, I glued very small pieces of brown thread trying to simulate the covering seams.

Also, the aileron hinges have been made in "retro" style. Instead of using CA hinges or, worse than that, aileron clear tape, I preferred to redesign and make them using thin plywood and a small brass nail as pivot. The final outcome wasn't too bad.

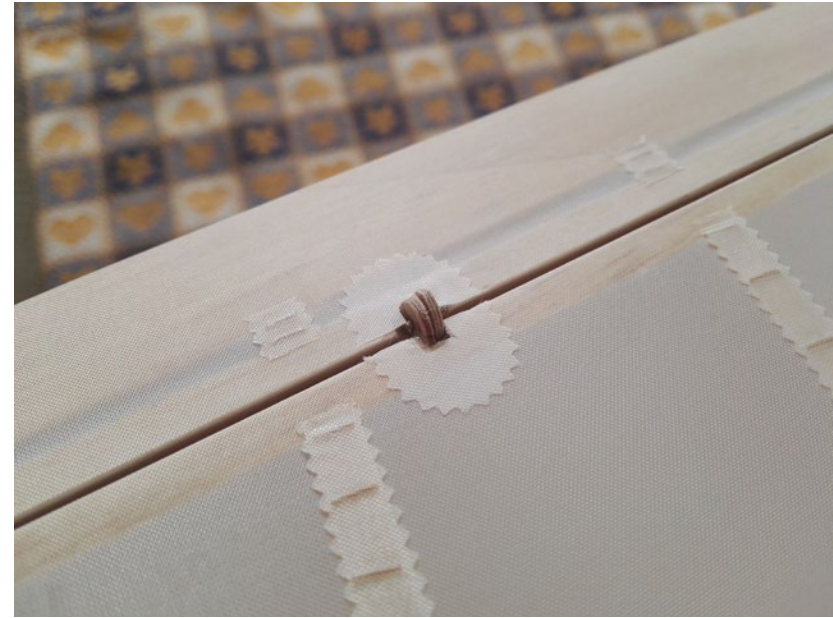
Instrument rings for the panel are 3D printed and painted with copper color varnish.

Finally, I also had fun in designing and creating a dedicated wooden case for this glider. I printed all the fixtures to hold the tools needed to assembly the model on the field.

The overall kit quality was pretty good but not excellent. Unfortunately, I found several plywood planks excessively bent. I fixed the problem by soaking the bent pieces in hot water and then I leave them to dry slightly bent on the other side. I know that it isn't a scientific method, but it actually works!



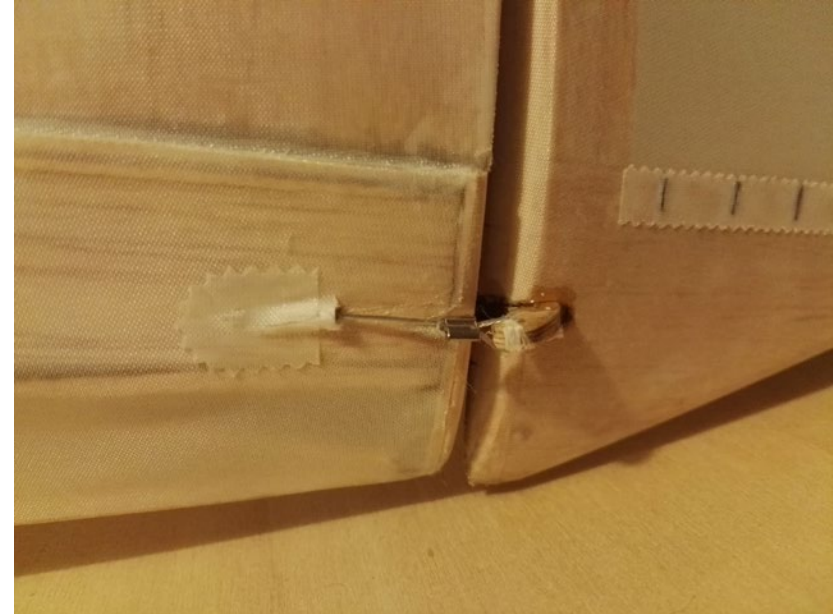




Center of gravity and command excursions have been set as per manual.

The whole model has been covered with Diacov 1000 tissue. This product is a self-glue heat shrink fabric used also on full scale airplanes and produced by Diatex. The weight per square meter is similar to Oratex but it costs about half. Moreover, it's available on rolls 1.5m wide that allows a good panel layout and saves material. It's available only in white, but it can be painted directly.

The maiden flight was carried out on my usual slope (Monte Mottarone, Italy) that I know very well, on a day with good lifting conditions. After having gained a suitable altitude, the first thing I wanted to try was the stall condition since this is the first model with forward-swept wing. It actually was as I expected, completely controllable, and also the ailerons were effective enough even in very slow speed conditions.





During the last Easter Monday, I also had the chance to try it under aerotow. After a brief tow I decided to release (don't forget that wingspan is just two meters and in seconds it becomes very very small...). The day had perfect lift so that I was able to test it also in thermal conditions. The typical pitch instability behavior of forward-swept wings helped me to better understand when I caught a thermal and turn around in meters. I didn't know that forward-swept wings are affected by adverse yaw behavior less than straight or swept wing, I set on the radio a certain amount of aileron to rudder mixer that I removed immediately.

That's the story of this model. As usually happens with a vintage glider, the interesting phase is building rather than flying. But I was honest with you: at the beginning of the article I told you that I was looking for a model to build, not to fly!

<<https://jamara-shop.com/KA-7-Lasercut>>

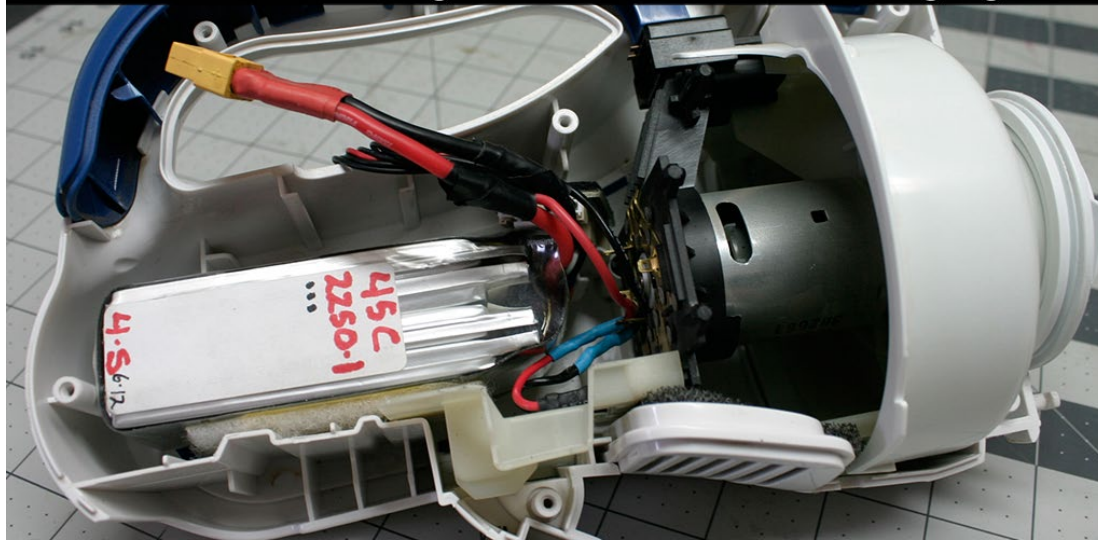




**BLACK &
DECKER**

DUST BUSTER

Lithium Battery Upgrade Hack
More Power - Longer Run Time - Faster Charging



Paul Naton / Radio Carbon Art Productions,
pnatonrca@gmail.com, <http://www.radiocarbonart.com>

I had a classic Black & Decker Dust Buster vacuum in my shop for years as they are great for cleaning up table top debris and sanding dust while working on RC gliders.

The unit's performance was never that great and the runtime short even after a full charge. Recently, the Buster's RPMs would start to fall rapidly after a few seconds of use and I suspected a failing battery pack. I hate to throw out perfectly good used cordless machines and it's always the batteries that fail long before the mechanics do.

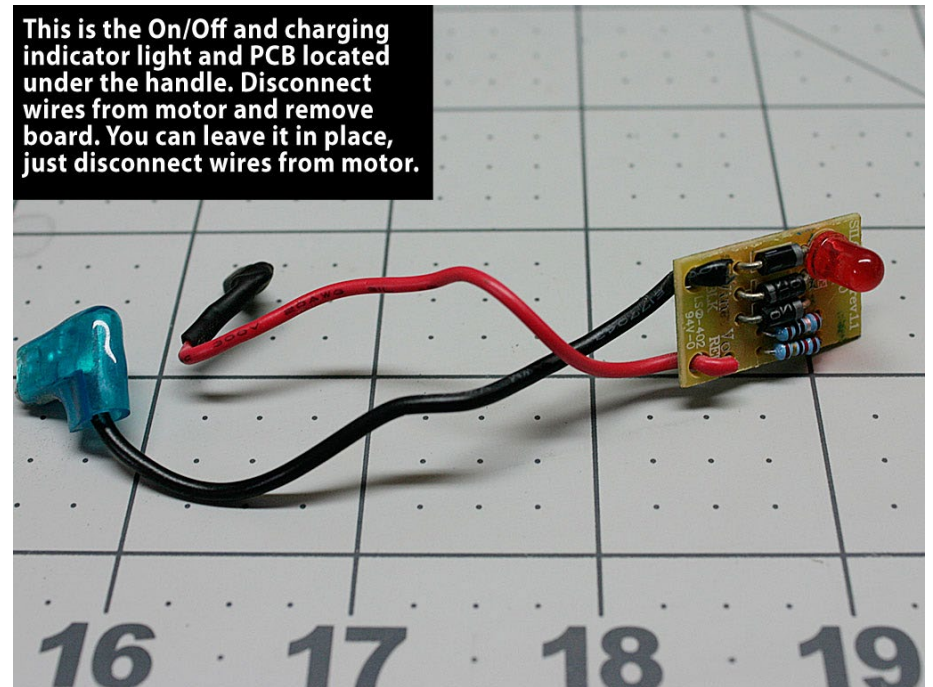
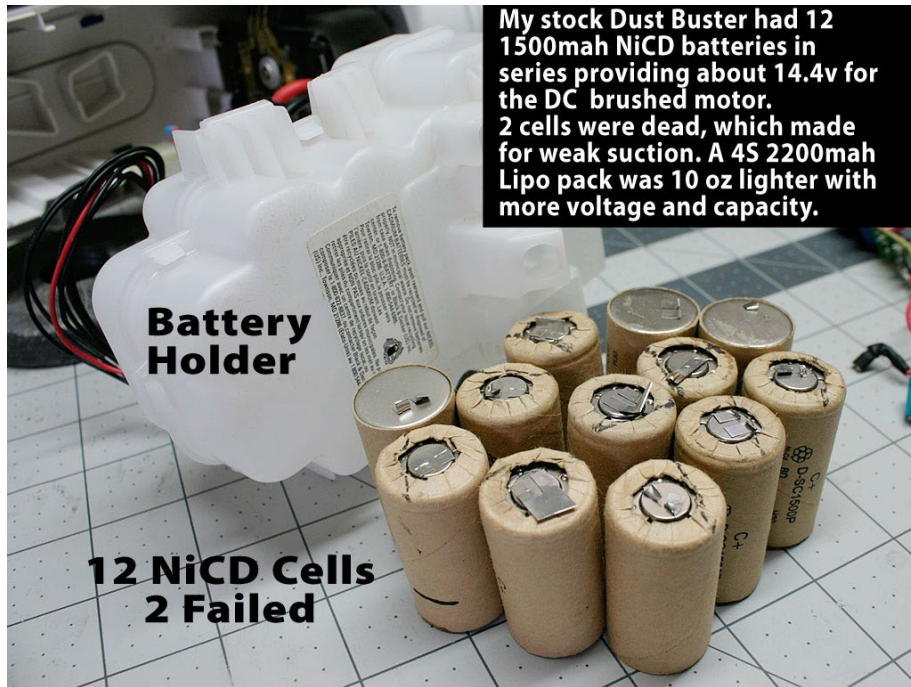
The Buster says 14.4 volts on the side so I knew there was a huge and heavy NiCd or NiMh pack sitting in that fat rear fuselage. At 14.4 volts, that would qualify it for some sort of Lithium pack, LiPo or some of those cool new Li-ion 3.7v cells. I had already replaced the dead NiCd 5S packs in my shop's Makita cordless drills with 2S 18650 Li-ion cells, and they now are always ready to go and run forever.

I poured myself a cold Porter and started to disassemble the unit to check out that old failing battery pack. The included photos show the internals and the wiring changes I made. It's an easy mod as long as you don't short the new pack while mod'ing the wires.

The Buster comes apart easily (warranty voided!), and I found a huge plastic battery box inside with a 12S 1500mah NiCD pack inside.

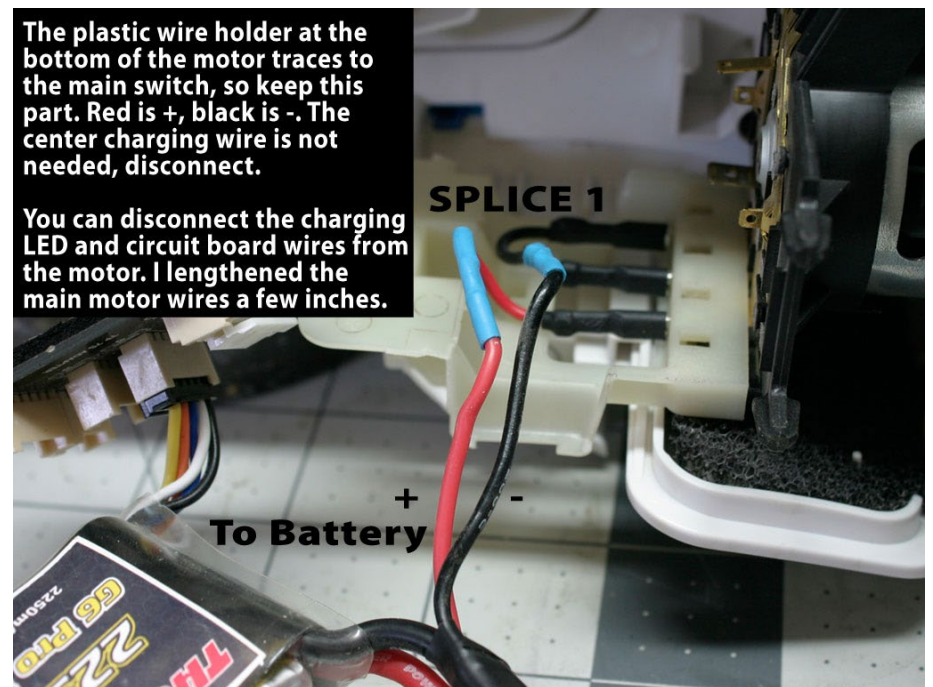
I knew that some of the cells might be bad, so I trickle charged it for 8 hours, and then tested the voltage of each cell. I was looking for any single cell reading at or under 1.1v. Two cells were at 1v, and another was at 1.1v. The rest of the cells measured at around 1.2v, though I suspected some memory effects over time had also reduced the pack capacity. The missing voltage of three cells really killed the units suction. Total weight of the NiCd pack was 19 oz.- 538 grams!

For a replacement battery I picked out of my LiPo safe a used 40C rated Thunder Power 4S 2200 Lipo which was no longer flight worthy, but still good enough for a low amp draw application.



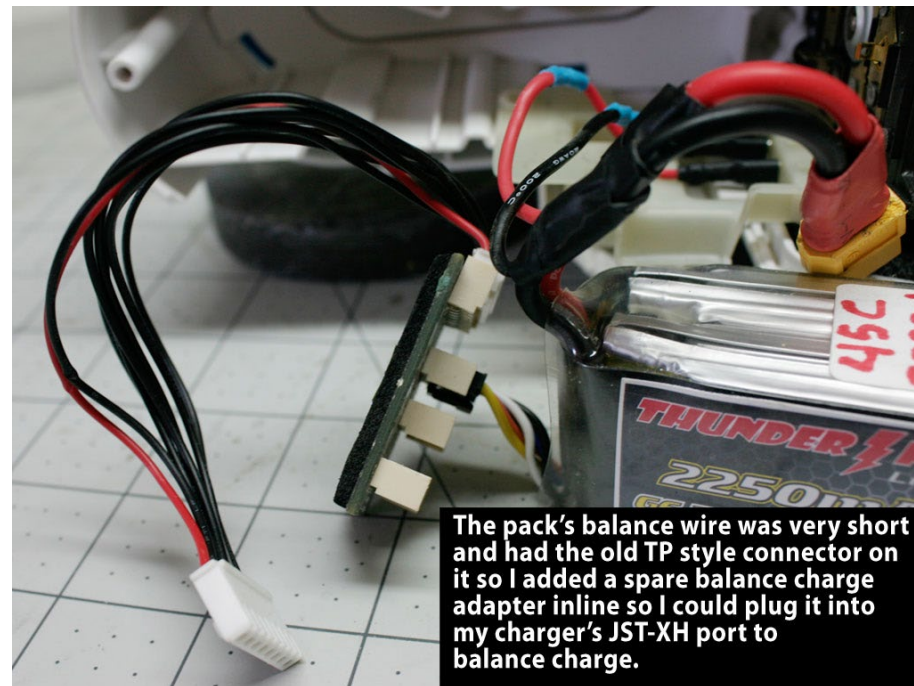
You could use a 4S Li-ion or Li-Fe pack for this application/hack as well. This battery had the old TP style balance connector with very short wires, so it was easier to plug the balance connector into a spare TP to JST-XH adapter board instead of soldering a more modern JST port on it. Balance charging is required to keep the cells healthy in this application. The XTC 60 connector hooks right to any of my chargers and I can charge the pack in minutes instead of hours. Nice. Total battery weight was now just 10 oz. - 283 grams!

The internal wiring is easy to figure out. There is a DC brushed motor connected to a plastic holder that has traces to the main power switch and the charging circuit PCB. I cut the battery box out, and removed the charging and power LED indicator light and PCB board from the top of the main body. The PCB board has two wires to the motor, just disconnect them. You can keep



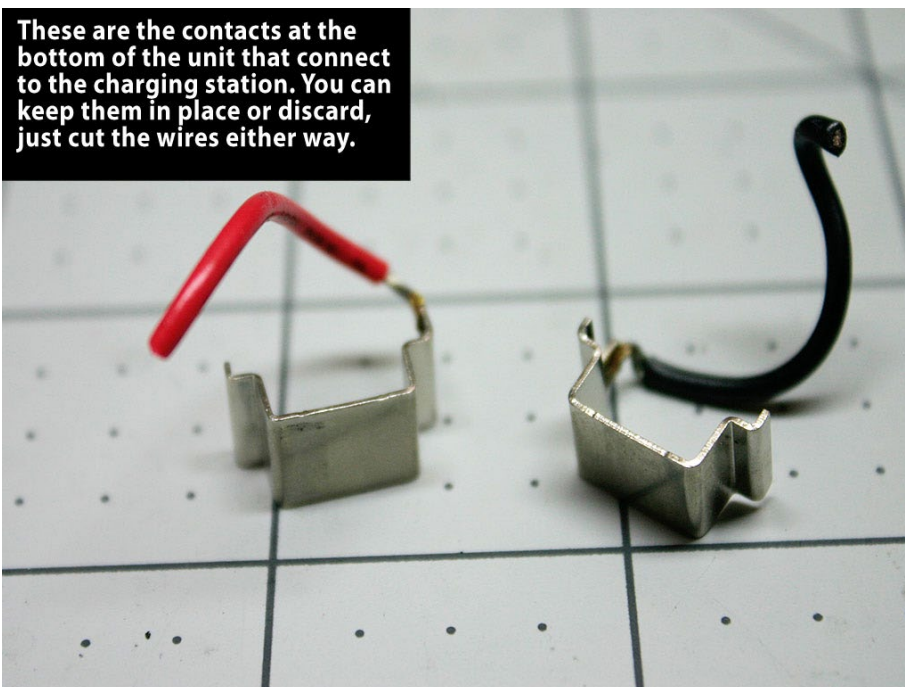
I first lengthened the motor's power wires a few inches with a soldered splice then stripped away insulation on the battery's main + & - wires and soldered the motor wires inline, protecting the splices with tape.

Do Not Short Battery Wires.
Do One At A Time!

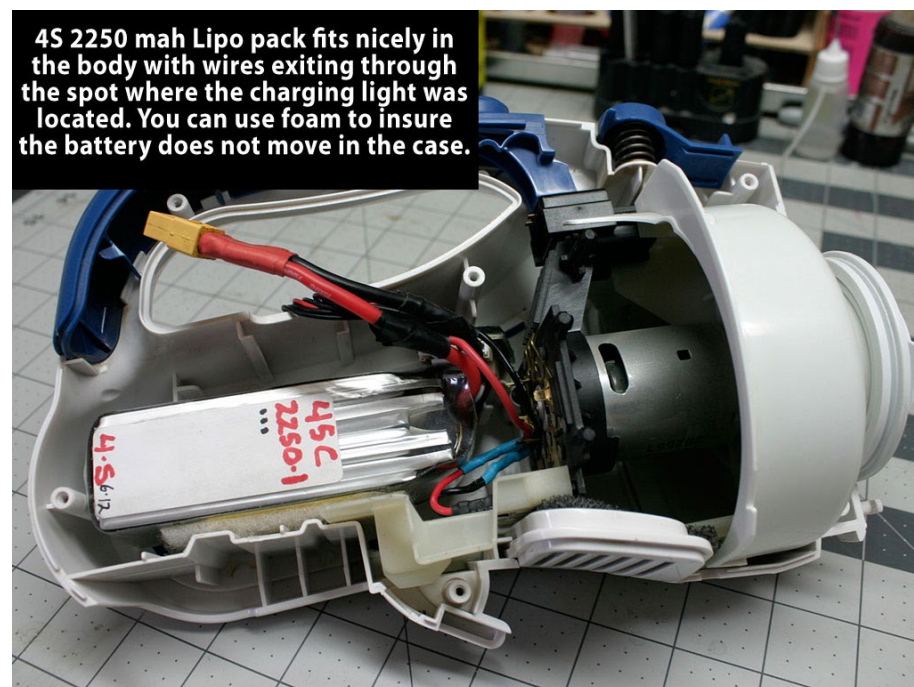


The pack's balance wire was very short and had the old TP style connector on it so I added a spare balance charge adapter inline so I could plug it into my charger's JST-XH port to balance charge.

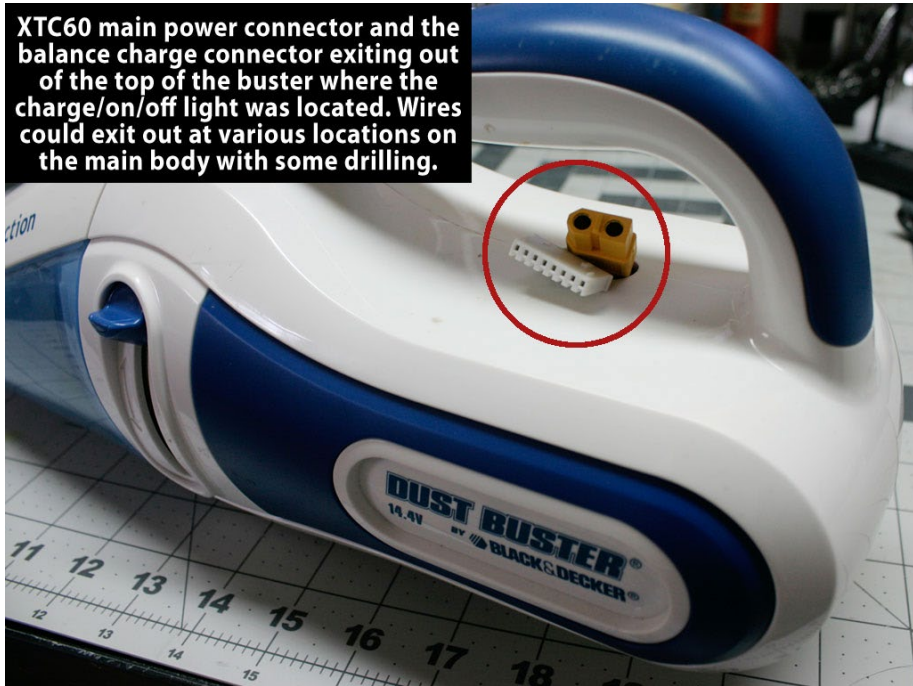
These are the contacts at the bottom of the unit that connect to the charging station. You can keep them in place or discard, just cut the wires either way.



4S 2250 mah Lipo pack fits nicely in the body with wires exiting through the spot where the charging light was located. You can use foam to insure the battery does not move in the case.



XTC60 main power connector and the balance charge connector exiting out of the top of the buster where the charge/on/off light was located. Wires could exit out at various locations on the main body with some drilling.



the PCB board in place as long as you disconnect the wires to the motor, but I wanted to run the charging wires through this hole so I discarded this part.

I next lengthened the two main motor power wires from the plastic holder a few inches with a solder splice which gave me some working slack. The center wire on the plastic wire holder can be cut or disconnected. You can also disconnect and remove the metal charging contact tabs at the bottom of the unit.

The positive (+) and negative (-) wires need to be spliced into the main battery wire for motor power. Do each wire separately for safety, do not short the battery wires!

I cut a small amount of the wire insulation from the negative battery wire first, then soldered the negative (-) motor wire to the

negative (-) battery wire. Some tape insulated the splice. I then did the same for the positive (+) wires.

With the motor wired to the battery, you can then test the switch, which should be in the OFF position when soldering power wires. The motor should turn on.

You will need to run the main battery power wires and the charge balance connectors outside the unit for charging. I was lazy and used the hole from the LED light and PCB under the handle to exit the wires. You can cut or drill a hole just about anywhere in the vac's body to exit the wires.

The freshly charged 4S Lipo outputs a solid 16+ volts to the motor, about 1.5 volts higher than the best the NiCds could give.

The suction is noticeably better at the higher RPM's and there is no voltage sag or motor over-heating even after many minutes of run time.

Once the RPMs start to noticeably drop, its time to recharge, you don't want to drain any Lithium pack to zero. You can use your Lipo voltage meter to check remaining capacity just like with your powered RC planes.

Dust Buster models vary, but most older models are likely to have NiCd packs and should be easy to modify with new batteries.

Newer Dust Buster models are available with Lithium batteries so just buy one of those for your shop.

This was an easy hack and this useful tool will be running for many years to come and I won't feel guilty feeding it carbon dust until it dies a natural death.

**Use any lithium battery with caution and charge them properly. NiCd batteries should be recycled at an authorized location.



BALSA FENCE & BALSA STRIPPER

Barrie Russell
Model Flying Hawkes Bay, New Zealand
<<http://www.mfhb.org.nz>>
07 October 2009

Last month (September 2009) on Flying Giants, Rod Ford published a picture of his balsa stripper on his Jungman “Git-R-Done” building Forum. It was quite the neatest unit I had seen, so I followed it up and found it had been designed by David Plumpe, who lives on Lake Keowee in upstate South Carolina.

I emailed Dave for information and permission to publish which he very kindly agreed to. He tells me...

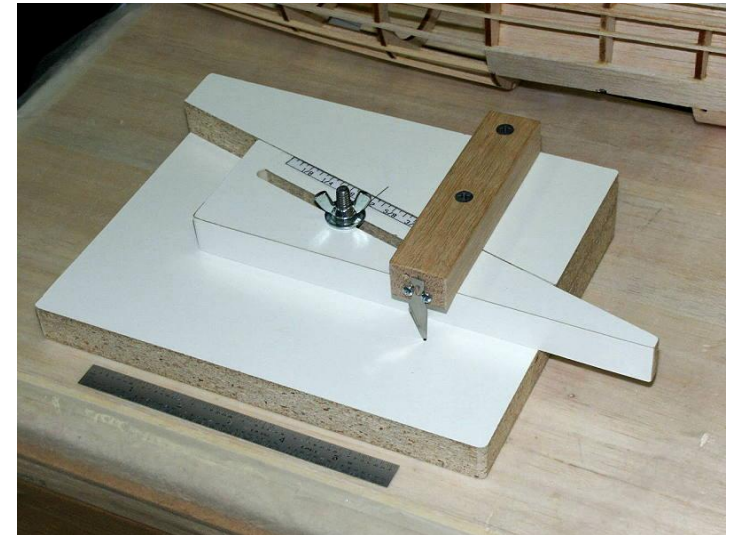
“I’ve been building model planes for at least 60 years, originally with painful double-edge razor blades, then X-acto knives, then unsatisfactory store-bought strippers, and finally this stripper. Actually, I use the fence more than the stripper, to cut my own leading and trailing edges, spars, etc. I certainly don’t claim credit for inventing the inclined plane or even for using it for fine adjustment in a balsa stripper/fence, but it did take me a few years to finally get a round tuit to work out the geometry I was happy with.

“I’m a retired electronics engineer (instrumentation for Navy ship research) and enjoy electronics, metalworking, boating, and lots of other stuff, but modeling has been a lifelong hobby and I can’t seem to shake it.

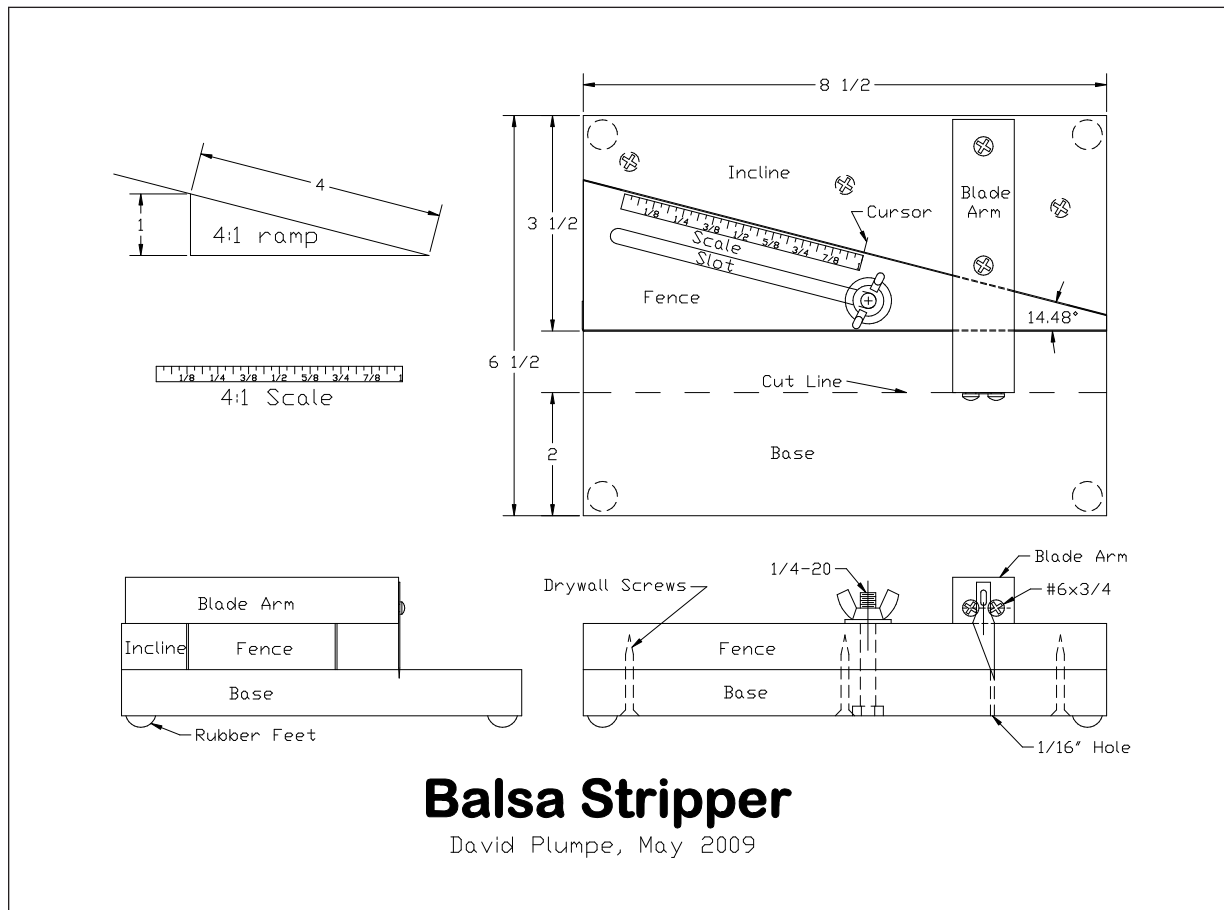
“I’m primarily an RC modeler. Mostly engines from .049ci to .60ci, but in recent years I’ve been doing some electrics.”



Balsa Fence



Balsa Stripper



Balsa Stripper

David Plumpe, May 2009

The following is excerpted from <https://www.rcgroups.com/forums/member.php?u=15730>

Dave Plumpe produced a PDF which includes both the explanatory text and the plans for both the Balsa stripper and Balsa Fence. We've uploaded it to the RCSD web site where it's available at <http://www.rcsoaringdigest.com/Supplements/BalsaFenceStripper.pdf>

I recently made a couple of tools for cutting balsa strips which I thought I'd pass on to the group. One is a standalone stripper based on the inclined fence and captured blade-tip approach. The other is a precision fence for my tablesaw. They're both accurate and very easy to set.

The balsa stripper is made of scraps of Melamine shelving, iron-on edging, and a small piece of hardwood for the blade arm. It's 8-1/2" wide, uses a 1:4 incline (1" lateral motion for 4" along hypotenuse), and cuts widths from 0 to 1". I use it for up to 1/8" medium balsa.

The tablesaw fence is made of a sink cutout from a laminated-surface kitchen countertop, a piece of 1/8" hardboard, and a hardwood strip for the cleat. It's 18" long, has a 1:8 incline, and also cuts 0-1" widths. I use it with a 7-1/4" hollow-ground veneer blade (DeWalt DW3326) and homemade zero-clearance table insert, for anything thicker than 1/8" or harder than balsa, leading & trailing edges, and really accurate cuts. With my 1950 Craftsman table saw I typically get cuts accurate to within a couple thousandths (even closer after a test cut) and smooth as a baby's bottom.

(Question by "Norm Furutani"):

On the knife stripper, you say captured blade-tip. Is the tip of the blade sitting in a small drilled hole?

What is the kerf on the saw blade? This is an all steel blade, not carbide?

Reply: Yes, the #11 blade tip is jammed into a 1/16" hole in the base. After assembling the wood parts, I slid the blade down to touch the base, tapped it to make a mark, then drilled the hole.

The tablesaw blade cuts a kerf of about 0.07". It's hollow-ground steel, not

carbide-tipped. Steel can take a sharper edge than carbide, so should give a cleaner cut, 'though I haven't tried a 7-1/4" carbide veneer/plywood blade on balsa. I've been using this blade for several years and it seems as sharp as ever.

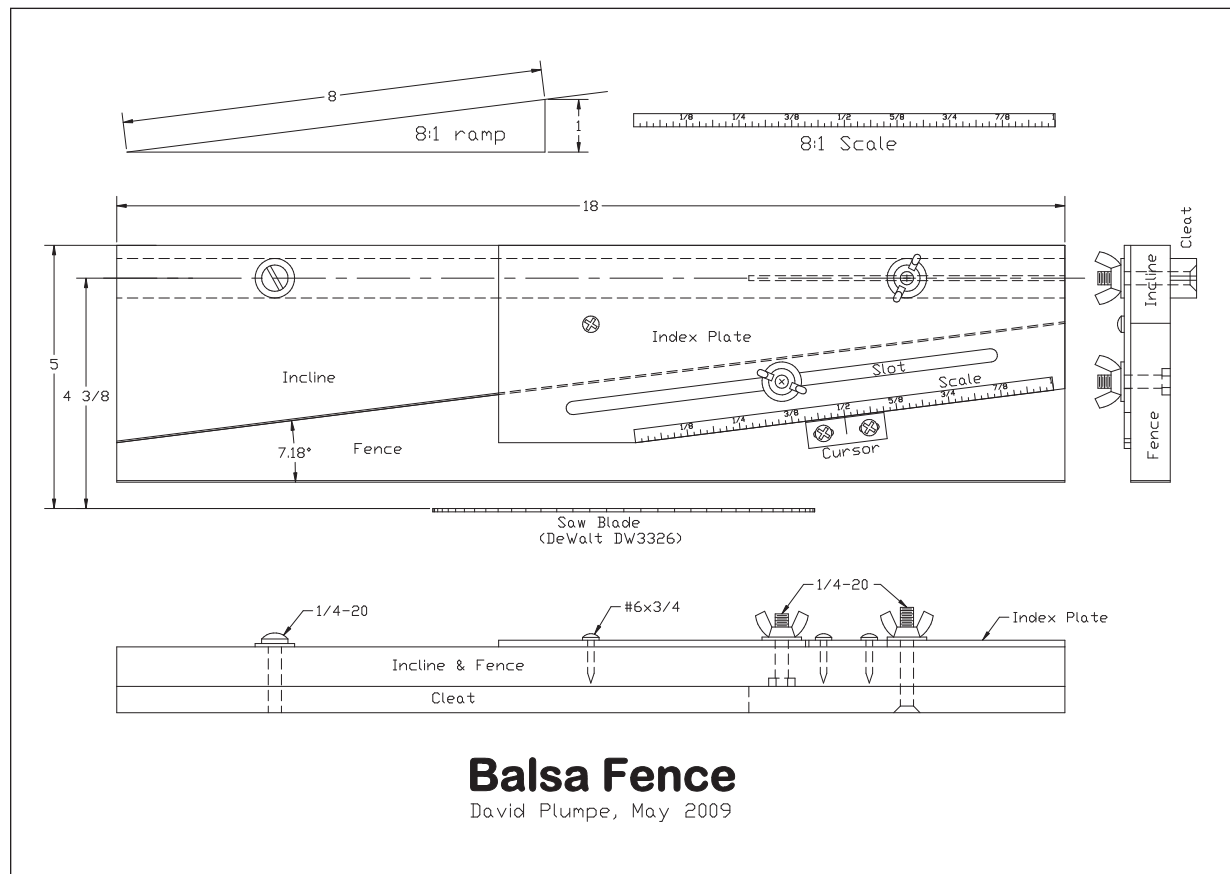
(Question by "littlewing78"):

Is there a certain angle you cut your fixtures at? Do the measurements stay accurate to the ruler you have on there or do you need to adjust it and mark your own?

Reply: The angle is the arcsine of the slope (the angle whose sine is the slope). For the slitter the slope is 1/4, so the angle is 14.4775 degrees and for the tablesaw fence the slope is 1/8, so the angle is 7.1808 degrees.

That's the fancy description. I don't have a protractor that accurate, so I accurately draw a line 1" in from the edge of a piece of paper and parallel to that edge, then find a point on that line that's 4" (or 8") from the corner. Draw a sloped line connecting that point with the corner. That triangle is the proper slope and I use that for cutting the incline. Does that make sense? If not, I'll draw something up.

For every 4 (or 8) inches of travel along the slope of the incline, you want 1" of distance change between the blade and fence.



Actually, you can make it any slope you want, as long as you can make an appropriate scale. I find it easier to have a scale that's a neat multiple (4 or 8) of a standard ruler.

Reply by "tommyeflight89":

It should just be a function of the angle of the triangle he has made. Any angle would work, with the smaller one giving you much more resolution.

Original David Plumpe document available for downloading from:
<http://www.rcsoaringdigest.com/Supplements/BalsaFenceStripper.pdf>

NRL Tests Autonomous “Soaring with Solar” Concept

<https://www.nrl.navy.mil/media/news-releases/2017/NRL-Tests-Autonomous-Soaring-with-Solar-Concept>

(WASHINGTON • May 9, 2017)

– Researchers at the U.S. Naval Research Laboratory (NRL), Vehicle Research Section and Photovoltaic Section are building on the proven concept of autonomous cooperative soaring of unmanned aerial vehicles (UAVs). Their research investigates the presence of solar photovoltaics (PV) to the cooperative autonomous soaring techniques, which enables long endurance flights of unmanned sailplanes that use the power of the Sun.

The Solar Photovoltaic and Autonomous Soaring Base Program and the U.S. Marine Corps’ Expeditionary Energy Office (E2O) want to improve the ability of unmanned platforms to support a 24-7 information, surveillance, and reconnaissance (ISR) mission. By doing so, the warfighter will greatly benefit because it will reduce the amount of batteries or fuel they must carry into battle, and improve the availability of continuous coverage of ISR assets.



Holding the photovoltaic (PV) UAV based on the SBXC sailplane, are members of the “Solar-Soaring” research flight crew (l-r) Dan Edwards and Trent Young (not shown: Chris Bovais, Sam Carter, Matthew Kelly, and Dave Scheiman). (U.S. Naval Research Laboratory)

“NRL has twice flown our solar UAV [based on the SBXC sailplane] over 10 hours using a combination of solar photovoltaics and autonomous soaring as part of the ‘solar-soaring’ research program,” said Dr. Dan Edwards, aerospace engineer. “This research is investigating the value of combining autonomous soaring algorithms and solar photovoltaics for capturing energy from the environment to extend flight endurance and mission operations of an aircraft.”

A photovoltaic array, custom built in NRL’s Vehicle Research Section and Photovoltaic Section, is integrated into the center wing panel of the PV-SBXC aircraft as a drop-in replacement to the original wing. A power management and distribution system converts the power from the solar arrays into direct current (DC) voltage, which the electric motor can use for propulsion, or recharge a ‘smart battery.’

Additionally, an autonomous soaring software algorithm — that would typically monitor the local vertical winds around the aircraft — commands the aircraft to orbit in any nearby updrafts, very similar to soaring birds. However, the algorithm was disabled for the two solar flights in order to assess the solar-only performance. Passive soaring — meaning no specific maneuvers are attempted to catch thermals — was

still allowed, to let the aircraft turn the motor off if altitude increased because of an updraft along the aircraft’s pre-defined flight path. The autonomous soaring software was tested extensively in previous flight demonstrations in late October 2015.

The UAV with solar arrays built at NRL using SunPower Inc. solar cells, flew for 10 hours, 50 minutes on October 14, 2016. Takeoff occurred at 7:20 a.m. at 95 percent battery state of charge and landing occurred at 6:10 p.m. with the battery at 10 percent state of charge. Thermal activity was very good in the middle of the day and 40 percent of the flight was spent with the motor off, and the solar array partly recharged the battery while the motor was off.

The UAV equipped with solar wings incorporated PV arrays from Alta Devices, Inc. It flew for 11 hours, 2 minutes on April 19, 2017. Takeoff occurred at 7:46 a.m., approximately an hour after sunrise, with the battery’s state of charge at 90 percent. Landing occurred at 6:48 p.m., approximately an hour before sunset, with the battery’s state of charge at 26 percent. Thermal activity was very weak and almost all of the flight was spent running the motor. Near solar noon, the solar array provided sufficient power to cruise on solar power alone.

The power management system for both flights was provided by Packet Digital, Inc., as part of a grant from the North Dakota Renewable Energy Council.

“The experiments confirm significant endurance gains are possible by leveraging thermal updrafts and incident solar radiation, rather than ignoring these free sources of energy,” Edwards said. “Future testing will focus on quantifying the trade space between improvements in solar cell efficiency and combining with autonomous soaring for improved solar-recharging.”

The Vehicle Research Section at NRL conducts research to develop technologies for autonomous, affordably expendable, unmanned systems that carry a wide variety of payloads for numerous mission scenarios. The Section is composed of aeronautical, aerospace, electrical, and mechanical engineers, scientists, and technicians dedicated to advancing the state-of-the-art in unmanned systems technology.

The Photovoltaics Section at NRL conducts research to develop photovoltaic (solar cell) technologies to enable logistics free, renewable, portable, power sources for the warfighter. The Section is composed of physicists, electrical engineers, and chemists dedicated to advancing the state-of-the-art in PV power sources and systems.

*Researchers at the U.S. Naval Research Laboratory (NRL), Vehicle Research Section and Photovoltaic Section tests a photovoltaic (PV) UAV [based on the SBXC sailplane], shown on takeoff at sunrise, October 14th, 2016. The research is to investigate the value of combining autonomous soaring algorithms and solar photovoltaics for capturing energy from the environment to extend the endurance of an aircraft.
(U.S. Naval Research Laboratory)*



The U.S. Naval Research Laboratory provides the advanced scientific capabilities required to bolster our country's position of global naval leadership. The Laboratory, with a total complement of approximately 2,500 personnel, is located in southwest Washington, D.C., with other major

sites at the Stennis Space Center, Miss., and Monterey, Calif. NRL has served the Navy and the nation for over 90 years and continues to advance research further than you can imagine. For more information, visit the NRL website <<https://www.nrl.navy.mil/>>.



Identifying the Flow Physics and Modeling Transient Forces on Two-Dimensional Wings

Aerospace & Defense Technology

<<http://www.aerodefensetech.com/component/content/article/1321-adt/tech-briefs/aerospace/26832-afri-0250>>

Using mathematics and modeling to understand the flow physics of aircraft wings undergoing highly unsteady maneuvers.

The main objective of this research was to better understand the flow physics of aircraft wings undergoing highly unsteady maneuvers. Reduced-order models play a central role in this study, both to elucidate the overall dynamical mechanisms behind various flow phenomena (such as dynamic stall and vortex shedding), and ultimately to guide flight control design for vehicles for which these unsteady phenomena are important.

Unsteady phenomena are of increasing interest to the Air Force, as lightweight unmanned air vehicles become more prevalent. With increasingly smaller and lighter vehicles envisioned in the future, understanding unsteady aerodynamics will become even more important, in order to design control systems that can respond to severe gusts, or perform highly agile maneuvers. The flight of small, highly maneuverable aircraft, whether biological or man-made, is greatly impacted by unsteady aerodynamic effects, which can be either beneficial or detrimental to flight. Accurate understanding of such effects can allow for the design of aircraft that are more efficient, responsive, and robust.

With advances in both experimental techniques and equipment, and computational power and storage capacity, researchers in fluid dynamics can now generate more high-fidelity data than ever before. The presence of increasingly large data sets calls for appropriate data analysis techniques, that are able to extract tractable and physically relevant information from the data. In particular, a much-desired goal in fluid mechanics, and indeed many other fields, is to obtain simple models that are capable of predicting the behavior of seemingly complex systems. Low-dimensional models can not only improve our fundamental understanding of such systems, but are often required for the purpose of efficient and accurate prediction, estimation and control.

Broadly speaking, one can obtain low-dimensional information about a system (whether it be in the form of a reduced-order model, or simply spatial modes corresponding to certain energetic or dynamic characteristics) in numerous ways, potentially using some combination of data collected from simulations and experiments, and theoretical knowledge of the system, such as the governing partial differential equations (PDEs).

Purely data-driven methods can include those developed particularly for fluids applications, such as the dynamic mode

decomposition (DMD), or those which are appropriated from other communities, such as the eigensystem realization algorithm (ERA), which was first applied to study spacecraft structures, but has more recently been appropriated to model a wide range of fluids systems.

Dynamic mode decomposition allows for the identification and analysis of dynamical features of time-evolving fluid flows, using data obtained from either experiments or simulations. In contrast to other data-driven modal decompositions such as the proper orthogonal decomposition (POD), DMD allows for spatial modes to be identified that can be directly associated with characteristic frequencies and growth/decay rates. Following its conception, DMD was quickly shown to be useful in extracting dynamical features in both experimental and numerical data. It has subsequently been used to gain dynamic insight on a wide range of problems arising in fluid mechanics and other fields.

One of the major advantages of DMD over techniques such as global stability analysis is that it can be applied directly to data, without the need for the knowledge or construction of the system matrix, which is typically not available for experiments. For this reason, analysis of the sensitivity of DMD to the type of noise typically found in experimental results is of particular importance.

This work was done by Clarence W. Rowley and David R. Williams of Princeton University for the Air Force Research Laboratory.

Original AFRL-0250 can be downloaded from:
<http://www.rcsoaringdigest.com/Supplements/AFRL-0250.pdf>

REPORT DOCUMENTATION PAGE				Form Approved OMB No. 0704-0188	
<small>The public reporting burden for this collection of information is estimated to average 1 hour per response, including the time for reviewing instructions, searching existing data sources, gathering and maintaining the data needed, and completing and reviewing the collection of information. Send comments regarding this burden estimate or any other aspect of this collection of information, including suggestions for reducing the burden, to the Department of Defense, Executive Service Directorate (0704-0188). Respondents should be aware that notwithstanding any other provision of law, no person shall be subject to any penalty for failing to comply with a collection of information if it does not display a currently valid OMB control number.</small> PLEASE DO NOT RETURN YOUR FORM TO THE ABOVE ORGANIZATION.					
1. REPORT DATE (DD-MM-YYYY) 26-08-2016		2. REPORT TYPE Final report		3. DATES COVERED (From - To) Mar 2012 - Sep 2015	
4. TITLE AND SUBTITLE Identifying the flow physics and modeling transient forces on two-dimensional wings				5a. CONTRACT NUMBER	
				5b. GRANT NUMBER FA9550-12-1-0075	
				5c. PROGRAM ELEMENT NUMBER	
6. AUTHOR(S) Clarence W. Rowley David R. Williams				5d. PROJECT NUMBER	
				5e. TASK NUMBER	
				5f. WORK UNIT NUMBER	
7. PERFORMING ORGANIZATION NAME(S) AND ADDRESS(ES) Princeton University Princeton, NJ 08544				8. PERFORMING ORGANIZATION REPORT NUMBER	
9. SPONSORING/MONITORING AGENCY NAME(S) AND ADDRESS(ES) Air Force Office of Scientific Research 875 N Randolph Street, Suite 325 Arlington, VA 22203				10. SPONSOR/MONITOR'S ACRONYM(S) AFOSR	
				11. SPONSOR/MONITOR'S REPORT NUMBER(S)	
12. DISTRIBUTION/AVAILABILITY STATEMENT DISTRIBUTION A: Distribution approved for public release.					
13. SUPPLEMENTARY NOTES					
14. ABSTRACT The main objective of the work described in this report is to better understand the flow physics of aircraft wings undergoing highly unsteady maneuvers. Reduced-order models play a central role in this study, both to elucidate the overall dynamical mechanisms behind various flow phenomena (such as dynamic stall and vortex shedding), and ultimately to guide flight control design for vehicles for which these unsteady phenomena are important. Our approach builds upon recent advances in understanding the dynamics of these unsteady flows, and uses state-of-the-art techniques, both for measuring these phenomena in experiments (using an unsteady wind tunnel), and for analyzing the data and developing reduced-order models (using techniques such as the Eigensystem Realization Algorithm and variants of Dynamic Mode Decomposition).					
15. SUBJECT TERMS Unsteady aerodynamics, reduced-order models, dynamic mode decomposition					
16. SECURITY CLASSIFICATION OF:			17. LIMITATION OF ABSTRACT	18. NUMBER OF PAGES 110	19a. NAME OF RESPONSIBLE PERSON
a. REPORT U	b. ABSTRACT U	c. THIS PAGE U			19b. TELEPHONE NUMBER (include area code)

Standard Form 298 (Rev. 8/98)
Prescribed by ANSI Std. Z39.18
 Adobe Professional 7.0

DISTRIBUTION A: Distribution approved for public release.



AFRL-AFOSR-VA-TR-2016-0305

Identifying the flow physics and modeling transient forces on two-dimensional wings

Clarence W. Rowley and David R. Williams, Principal Investigators

August 26, 2016

DISTRIBUTION A: Distribution approved for public release.

Air Force Research Laboratory
AF Office Of Scientific Research (AFOSR)/RTA1

DISTRIBUTION A: Distribution approved for public release.

Contents

1 Introduction 1
1.1 Unsteady aerodynamics 2
1.2 Data-driven modeling 3
1.3 Organization and contributions 5
2 Background and motivating results 9
3 Data-driven modeling 17
4 Lift enhancement by periodic pitching 33

iii

DISTRIBUTION A: Distribution approved for public release.

5	Nonlinear reduced-order models using EDMD	51
5.1	Introduction	51
5.2	Proper orthogonal decomposition and Galerkin projection	53
5.2.1	Proper orthogonal decomposition	53
5.2.2	Galerkin projection	54
5.3	Reduced-order models using extended dynamic mode decomposition	54
5.3.1	Dynamic Mode Decomposition	55
5.3.2	Extended dynamic mode decomposition and nonlinear models	55
5.3.3	A modification to DMD/EDMD	56
5.4	Example: flow past a circular cylinder	57
5.4.1	Data arrangement and selection	58
5.4.2	Comparison between EDMD and GP models, regularization, and model order dependence	59
5.4.3	Model prediction for untrained conditions	59
5.4.4	Noisy data	63
5.4.5	Data from a restricted spatial domain	63
5.4.6	Data from limited temporal sampling	65
5.5	Discussion and conclusions	67
6	Correcting for sensor noise in DMD	69
6.1	Introduction	69
6.2	Characterizing noise in dynamic mode decomposition	71
6.2.1	Dynamic mode decomposition	71
6.2.2	Sensor noise in DMD	72
6.2.3	Direct correction of sensor noise bias in DMD	75
6.2.4	Forward-backward DMD	76
6.2.5	Total least-squares DMD	77
6.3	Results with synthetic data	79
6.3.1	Example: A periodic linear system	79
6.3.2	A periodic linear system with a high-dimensional state of observables	81
6.3.3	Comparison to other modified DMD algorithms	82
6.3.4	Identifying hidden dynamics	83
6.3.5	Differentiating between process and sensor noise	84
6.4	Results with numerical and experimental data	87
6.4.1	Cylinder wake: simulation data	87
6.4.2	Cylinder wake: experimental data	88
6.5	Discussion and conclusions	89
	Bibliography	94

Chapter 1

Introduction

The main objective of the work described in this report is to better understand the flow physics of aircraft wings undergoing highly unsteady maneuvers. Reduced-order models play a central role in this study, both to elucidate the overall dynamical mechanisms behind various flow phenomena (such as dynamic stall and vortex shedding), and ultimately to guide flight control design for vehicles for which these unsteady phenomena are important.

Unsteady phenomena are of increasing interest to the Air Force, as lightweight unmanned air vehicles become more prevalent. With increasingly smaller and lighter vehicles envisioned in the future, understanding unsteady aerodynamics will become even more important, in order to design control systems that can respond to severe gusts, or perform highly agile maneuvers.

Our approach builds upon recent advances in understanding the dynamics of these unsteady flows, and uses state-of-the-art techniques, both for measuring these phenomena in experiments (using an unsteady wind tunnel at IIT), and for analyzing the data and developing reduced-order models (using techniques such as the Eigensystem Realization Algorithm and variants of Dynamic Mode Decomposition, being developed at Princeton).

The studying of aerodynamics and fluid mechanics predate the birth of the scientific method itself. From the initial musings of Aristotle and Archimedes, to the sketches of Leonardo Da Vinci, to George Caley's conception of a modern airplane configuration in 1799. Yet, in spite of this long history, and the fact that the underlying governing equations of viscous fluid flow being known for hundreds of years, there is still much to learn. For example, in many respects we are still catching up to the mastery exhibited by biological swimmers and fliers, in terms of maneuverability and efficiency. This "unfinished business" is not by any means due to a lack of imperative. Indeed, reductions in aerodynamic drag on cars, trucks, airplanes and ships can lead to billions of dollars in fuel savings, and significant reductions of CO₂ emissions, to speak nothing of the enhanced safety and maneuverability that would come with, for example, a more comprehensive understanding of the dynamics of aircraft in deep stall.

With advances in both experimental techniques and equipment, and computational power and storage capacity, researchers in fluid dynamics can now generate more high-fidelity data than ever before. This is crucial to advancing the field as a whole, since all but the most idealized, simple systems cannot be fully understood by analytical deductions alone. Moreover, advances in materials, manufacturing, and the miniaturization of processors allow for new questions to become of practical interest. This is not to suggest that the field of fluid dynamics and aerodynamics are now confined to the realms of data science. Indeed, progress is made by combining the insight attained from study of the fundamental equations with the additional dimension of large data. Indeed, obtaining the right data relies on understanding of the physical system. Beyond this, however, data

collection should also be informed by a proper understanding of the capabilities and limitations of the algorithmic tools that are required to assist in data analysis.

The presence of increasingly large data sets necessitates the use of such post-processing techniques that are able to extract tractable and physically relevant information from the data. This report considers methods to extract pertinent information and models from data obtained from fluids simulations and experiments. While the focus is on unsteady aerodynamic systems, specifically pitching airfoils, the techniques used and developed are applicable to a wider range of applications, both within and outside of fluids systems.

1.1 Unsteady aerodynamics

The flight of small, highly maneuverable aircraft, whether biological or manmade, is greatly impacted by unsteady aerodynamic effects, which can be either beneficial or detrimental to flight. Accurate understanding of such effects can allow for the design of aircraft that are more efficient, responsive, and robust.

The need to account for unsteady effects has been recognized since soon after the breakthrough of powered manmade flight, in the classical works of Wagner [155], Theodorsen [142], and Garrick [50]. Indeed, many failed attempts at flight can probably be attributed to a severe lack of understanding of how to utilize such effects. These classical models give significant insight into the fundamental flow physics associated with unsteady flight, such as relative contributions to lift of the added mass, quasi-steady bound circulation, and wake vortices. For example, the Theodorsen model gives the relationship between the airfoil kinematics (α , $\dot{\alpha}$, and $\ddot{\alpha}$) and the lift coefficient by:

$$C_L = \frac{\pi}{2} \left(\dot{\alpha} - \frac{1}{2} a \ddot{\alpha} \right) + 2\pi \left(\alpha + \frac{1}{2} \dot{\alpha} \left(\frac{1}{2} - a \right) \right) C(k), \quad (1.1.1)$$

where a is a parameter that defines the pitch axes, with $a = -1$ and $+1$ corresponding to pitching about the leading and trailing edge of the airfoil, respectively. $k = \frac{\pi f c}{U}$ is the reduced frequency, and $C(k)$ is the Theodorsen function, which governs the interaction between the shed vorticity in the wake and the circulatory lift force. While such models can be quantitatively accurate for cases of attached flow where viscous effects are negligible, they quickly lose validity when dealing with separated flows, which are often encountered in the extreme motions that are possible for birds, insects, and micro and unmanned aerial vehicles (MAV and UAV). It is precisely in these extreme cases that accurate predictive models are essential to prevent catastrophic failure and ensure ongoing successful flight. While more accurate predictions can be attained from high-fidelity simulations, the computational cost typically prohibits the direct use of such simulations for real-time prediction and control.

Biological examples such as insects [18, 120, 156] and birds [153] have seemingly evolved to take advantage of the high transient lift force that can be generated due to the formation of a leading edge vortex (LEV) during rapid pitch-up motion, for example. While these give motivating examples of the advantages of accurate understanding of unsteady aerodynamic effects, the preferred wing kinematics arising from evolution is highly specific and coupled to the geometry and other physiological features of the animal. Indeed, the characteristics of unsteady aerodynamic effects, particularly for separated flows, seem to be quite sensitive to both the geometry [79] and Reynolds number [166] of the airfoils. Studies into low Reynolds number flow over stationary [166, 4, 165] and pitching [154, 1, 131, 30, 80] symmetric airfoils have revealed, for example, complex effects associated with the stability and separation of the suction surface boundary layer, which are again highly sensitive to Reynolds numbers. These observations motivate the development of general

DISTRIBUTION A: Distribution approved for public release.

modeling procedures that can be easily applied to a range of parameter cases. In addition, it is desirable for such methods to be sufficiently general such that they can be applied to more realistic aircraft configurations, rather than just airfoils. As an example, such data driven modeling was considered for the case of accurate prediction and control of lift for a low Reynolds number pitching airfoil [22, 23], using the eigensystem realization algorithm [72] (ERA) and observer/Kalman filter identification [74] (OKID). There has also been a significant amount of work in terms of nonlinear modeling, ranging from low order state-space models formulated from theoretical considerations [54], to Volterra series models that have been used to model a range of unsteady aerodynamic and aeroelastic phenomena [132, 85, 11].

1.2 Data-driven modeling

With advances in both experimental techniques and equipment, and computational power and storage capacity, researchers in fluid dynamics can now generate more high-fidelity data than ever before. The presence of increasingly large data sets calls for appropriate data analysis techniques, that are able to extract tractable and physically relevant information from the data. In particular, a much-desired goal in fluid mechanics, and indeed many other fields, is to obtain simple models that are capable of predicting the behavior of seemingly complex systems. Low-dimensional models can not only improve our fundamental understanding of such systems, but are often required for purpose of efficient and accurate prediction, estimation and control. Broadly speaking, one can obtain low-dimensional information about a system (whether it be in the form of a reduced-order model, or simply spatial modes corresponding to certain energetic or dynamic characteristics) in numerous ways, potentially using some combination of data collected from simulations and experiments, and theoretical knowledge of the system, such as the governing partial differential equations (PDEs).

Purely data-driven methods can include those developed particularly for fluids applications, such as the dynamic mode decomposition (DMD) [125, 126], or those which are appropriated from other communities, such as the eigensystem realization algorithm (ERA) [82, 72], which was first applied to study spacecraft structures, but has more recently been appropriated to model a wide range of fluids systems [25, 2, 68, 69, 22, 23, 15, 67, 49].

Dynamic mode decomposition allows for the identification and analysis of dynamical features of time-evolving fluid flows, using data obtained from either experiments or simulations. In contrast to other data-driven modal decompositions such as the proper orthogonal decomposition (POD), DMD allows for spatial modes to be identified that can be directly associated with characteristic frequencies and growth/decay rates. Following its conception, DMD was quickly shown to be useful in extracting dynamical features in both experimental and numerical data [125, 126]. It has subsequently been used to gain dynamic insight on a wide range of problems arising in fluid mechanics [e.g., 119, 128, 127, 100, 129, 43, 58, 70, 83, 93, 55, 123, 45] and other fields [e.g., 59].

DMD has a strong connection to Koopman operator theory [81, 88], as exposed in [119], and further reviewed in [89], which can justify its use in analyzing nonlinear dynamical systems. Since its original formulation, numerous modifications and extensions have been made to DMD. Chen et al. [27] highlights the connection that DMD shares with traditional Fourier analysis, as well as proposing an optimized algorithm that recasts DMD as an optimal dimensionality reduction problem. This concept of finding only the dynamically important modes has also been considered in subsequent works of [164] and [71]. All of these works are motivated, in part, by the fact that by default DMD will output as many modes as there are pairs of snapshots (assuming that the length of the snapshot vector is greater than the number of snapshots), which is arbitrary with respect to the dynamical system under consideration. In reality, one would prefer to output only

DISTRIBUTION A: Distribution approved for public release.

the modes and eigenvalues that are present (or dominant) in the data. When the data is corrupted by noise (as will always be the case to some degree, especially for experimental data), this process becomes nontrivial, since noisy data might have a numerical rank far larger than the dimension of the governing dynamics of the system. Further to this, one cannot expect to have a clean partition into modes that identify true dynamical features, and those which consist largely of noise.

Simple ways of achieving this objective can involve either first projecting the data onto a smaller dimensional basis (such as the most energetic POD modes) before applying DMD, or by choosing only the most dynamically important DMD modes after applying DMD to the full data. One can also truncate the data to a dimension larger than the assumed dimension of the dynamics, and then apply a balanced truncation to the resulting dynamical system to obtain the desired reduced order model. This approach is sometimes referred to as *over-specification* in the system identification community [see, e.g., 75]. Keeping a higher dimension of data than that of the assumed dynamics can be particularly important for input-output systems that have highly energetic modes that are not strongly observable or controllable [112]. Ideally, any algorithm that restricts the number of DMD modes that are computed should also additionally be computationally efficient. A fast method to perform DMD in real time on large datasets was recently proposed in [62], while a library for efficient parallel implementation of number of common modal decomposition and system identification techniques is described in [16]. Sayadi and Schmid [122] also gives an explicit implementation of DMD for parallelized computation. One can also achieve computational speedup by incorporating efficient methods to compute singular value decompositions, typically the computational bottleneck in DMD, to speed up the computation []

One of the major advantages of DMD over techniques such as global stability analysis, for example, is that it can be applied directly to data, without the need for the knowledge or construction of the system matrix, which is typically not available for experiments [126]. For this reason, analysis of the sensitivity of DMD to the type of noise typically found in experimental results is of particular importance. The effects of noise on the accuracy of the DMD procedure was systematically investigated in the empirical study of [44], for the case of a synthetic waveform inspired by canonical periodic shear flow instabilities. More recently, [101] have extended this type of analysis to more complex data with multiple frequencies, as might be found in typical fluids systems.

An notable limitation of the methods mentioned so far is that (when considered in the context of data-driven reduced-order modeling techniques) they are linear, in the sense that the reduced order model that is identified is in the form of a linear system of ordinary differential equations (ODEs). While there have been a number of examples of nonlinear data-driven modeling techniques used in fluids applications [85, 102, 104, 52, 11, 37, 77, 60, 39, 24], their widespread use has been more limited, and the underlying theory is less established, than linear techniques. More details concerning the application of data-driven modeling techniques in fluid mechanics can be found in recent review articles [21, 113].

Perhaps the most common method to obtain a nonlinear reduced order model for fluids systems comes via a projection of the governing equations onto a low-dimensional basis that is optimal for capturing the energy of the data, i.e., the proper orthogonal decomposition (POD) [86, 17, 66], a procedure referred to as Galerkin projection. Galerkin projection (GP) has been used to extract models for many different fluids systems, a non-exhaustive list includes flow past a cylinder at low Reynolds number [41, 96, 95], grooved channels [41] the wall region of turbulent boundary layers [6, 103], flat plate boundary layers [111], turbulent plane Couette flow [91, 134], turbulent pipe flow [19] cavity oscillations [116, 115], mixing layers [110, 150, 13], and compressible flows [118]. One significant drawback of GP models is that they ignore modes that are low in energy, but are required for the dissipation of energy in the full system. A number of modifications have been proposed to address this concern, as well as other issues with such models. Aubry et al. [6] and Podvin [103]

DISTRIBUTION A: Distribution approved for public release.

use an eddy viscosity term that accounts for energy dissipated into unmodeled modes. Östth et al. [99] investigate a hierarchy of eddy viscosity formulations, while Wang et al. [157, 158] incorporate LES closure modeling strategies. Refs. [35] and [36] summarize a number of calibration techniques that can be used to improve the accuracy of Galerkin models, and also discuss the various ways in which the error of such models can be quantified. Ref. [12] employs a subspace rotation technique to stabilize the models, which, unlike other calibration techniques, maintains consistency with the original governing equations. Ref. [13] imposes constraints to balance the turbulent kinetic energy of the resulting model. All of these modifications of Galerkin projection increase the “data-driven” nature of the method. Ref. [97] gives an in-depth summary and analysis of many issues, variations, progress, and open problems on the topic of Galerkin projection models, while [84] gives a clear expository introduction of the main ideas in Galerkin projection, with examples.

While we mentioned above that DMD could be classified as a “linear” method, connections between the DMD algorithm and the Koopman operator [119, 89] give promise that it can ultimately be used to model and understand nonlinearities. The Koopman operator [81] gives a means of representing a finite-dimensional, nonlinear system as an infinite dimensional linear system, and DMD gives a finite-dimensional approximation to this operator.

In particular, an extension of DMD that potentially allows for better representation of nonlinear data has also recently been proposed [160], and although the computational costs increase dramatically with the dimension of the system, a kernel method described in [159] reduces the cost to be comparable to standard DMD.

1.3 Organization and contributions

Following this introductory chapter, Chapter 2 presents a summary of key concepts and techniques in data-driven modeling of fluid systems, as well as presenting some results that, besides being of some independent interest, will motivate the research directions taken in the subsequent chapters. Broadly speaking, Chapters 4 and 3 focus specifically on the application pitching airfoils, while 5 and 6 focus on data-driven modeling techniques, particularly extensions and improvements to DMD and their application to fluids systems. More precisely, the report includes the following sections:

Chapter 3 obtains models to predict the pressures and forces on a rapidly pitching airfoil. This is one of the first applications to experimental data of a recently developed variant of DMD to allow for the identification of systems that contain inputs (e.g., systems that are being controlled externally in some manner) [105]. We show that this modeling approach is convenient for constructing “switched models”, whereby one can predict the behavior of a nonlinear system by switching between a family of linear models. In particular, the “DMD with inputs” method gives models for which the coordinates of the models remain consistent with each other, which eliminates complications and ill-conditioning that has been observed when using alternate methods [38]. This modeling approach allows for the formulation of a switched model that remains accurate over a wide range of angles of attack, ranging from attached to fully separated flow. The experiments and subsequent analysis were performed with Nicole Schiavone, an undergraduate working in Prof. Rowley’s lab in summer 2014. Material in this chapter is based on the conference paper:

- Scott T M Dawson, Nicole K Schiavone, Clarence W Rowley, and David R Williams. A data-driven modeling framework for predicting forces and pressures on a rapidly pitching airfoil. In 45th AIAA Fluid Dynamics Conference, page 2767, 2015.

Chapter 4 explores a phenomena that is identified in Chapter 2: Namely that airfoils undergoing low-amplitude sinusoidal pitching motion generate enhanced lift when pitching occurs at a

DISTRIBUTION A: Distribution approved for public release.

preferred frequencies. A systematic parameter sweep over the pitching frequency, amplitude, and base angle of attack is conducted, with the mean and frequency content of the forces analyzed. In addition, the flow fields are studied using DMD. Material in this chapter is based on the conference paper:

- Scott TM Dawson, Daniel C Floryan, Clarence W Rowley, and Maziar S Hemati. Lift enhancement of high angle of attack airfoils using periodic pitching. In 54th AIAA Aerospace Sciences Meeting, page 2069, 2016.

Chapter 5 shows how a recently developed extension to DMD can be utilized to obtain nonlinear reduced order models for fluids systems. We modify the extended DMD algorithm to include a Tikhonov regularization step, which is found to give improved results for the purposes of nonlinear system identification. The method is demonstrated on the canonical example of flow past a circular cylinder, for data starting near the unstable equilibrium solution and converging to the periodic vortex shedding limit cycle. It is demonstrated that this approach can be superior to classical POD-Galerkin projection, particularly in cases where the data is noisy, is from a limited spatial region, is not spatially resolved, or is only collected over a short time window. Material in this chapter is contained in the paper:

- Scott T. M. Dawson and Clarence W. Rowley, Nonlinear reduced-order models of fluids systems using extended dynamic mode decomposition, *In preparation for Theoretical and Computational Fluid Dynamics*, 2016.

Some of the results presented in Chapter 5 are also used in an upcoming review paper:

- Clarence W. Rowley and Scott T. M. Dawson. Model reduction for flow analysis and control. *Annual Review of Fluid Mechanics*, 49(1), 2017.

Chapter 6 analyzes the effect of noise of DMD. As well as giving an explanation for a previously identifies sensitivity to noisy data, three variants of the DMD algorithm are proposed, all of which perform better on noisy data. This work was performed with Maziar Hemati and Matthew Williams, and is published in the following paper:

- Scott T. M. Dawson, Maziar S. Hemati, Matthew O. Williams, and Clarence W. Rowley. Characterizing and correcting for the effect of sensor noise in the dynamic mode decomposition. *Experiments in Fluids*, 57(42):1?19, 2016.

In addition to the publications listed above, Chapter 2 uses some material from the paper:

- Steven L Brunton, Scott T M Dawson, and Clarence W Rowley. State-space model identification and feedback control of unsteady aerodynamic forces. *Journal of Fluids and Structures*, 50:253?270, 2014.

Effort is made to keep notation consistent throughout this report; however, on occasion notation changes between chapters, in attempt to uphold existing conventions in the relevant fields. While each of these chapters is largely self contained, we present in Chapter 2 underlying preliminaries that are broadly relevant across all sections of this thesis.

1.3.1 Publications supported by this grant

Journal papers:

DISTRIBUTION A: Distribution approved for public release.

- Dawson STM and Rowley CW, “Nonlinear reduced-order models of fluids systems using extended dynamic mode decomposition,” in preparation.
- Hemati MS, Dawson STM, and Rowley CW, “Parameter-Varying Models for Unsteady Aerodynamic Response Prediction,” submitted to *AIAA Journal*.
- Rowley CW and Dawson STM, “Model reduction for flow analysis and control,” *Annual Reviews in Fluid Mechanics*, to appear, Jan 2017.
- Monnier B, Williams DR, Weier T, and Albrecht T, “Comparison of a Separated Flow Response to Localized and Global type Disturbances,” *Experiments in Fluids*, accepted for publication, Jun 2016.
- Williams DR, Reissner F, Greenblatt D, Muehler-Vahl H, and Strangfeld C, “Modeling Lift Hysteresis on Pitching Airfoils with a Modified Goman-Khrabrov Model,” *AIAA Journal*, accepted for publication, Aug 2016.
- Dawson STM, Hemati MS, Williams MO, and Rowley CW, “Characterizing and correcting for the effect of sensor noise in the dynamic mode decomposition,” *Experiments in Fluids*, 57:42, 2016.
- Williams DR, An X, Iliev S, King R, and Reissner F, “Dynamic hysteresis control of lift on a pitching wing,” *Experiments in Fluids*, 56:1–12, 2015.
- An X, Grimaud L, and Williams D, “Feedforward Control of Lift Hysteresis during Periodic and Randomized Pitching Maneuvers,” In: King R (ed) *Active Flow Control and Combustion Control*, vol 127. Springer, Heidelberg, pp 55–69.
- Tu JH, Rowley CW, Luchtenburg DM, Brunton SL, and Kutz JN, “On dynamic mode decomposition: theory and applications,” *J. Computational Dynamics*, 1(2):391–421, Dec 2014.
- Hemati MS, Williams MO, and Rowley CW, “Dynamic mode decomposition for large and streaming datasets,” *Physics of Fluids*, 26(11):111781, Nov 2014.
- Brunton SL, Dawson STM, and Rowley CW, “State-space model and feedback control of unsteady aerodynamic forces,” *Journal of Fluids and Structures*, 50:253–270, Oct 2014.
- Brunton SL, Rowley CW, and Williams DR, “Reduced-order unsteady aerodynamic models at low Reynolds numbers,” *Journal of Fluid Mechanics*, 724:203–233, Sep 2013.

Conference papers:

- Dawson STM, Hemati MS, Floryan D, and Rowley CW, “Lift Enhancement of High Angle of Attack Airfoils using Periodic Pitching,” 54th AIAA Aerospace Sciences Meeting, San Diego, CA, January 2015.
- Dawson STM, Schiavone NK, Rowley CW, and Williams DR, “A Data-Driven Modeling Framework for Predicting Forces and Pressures on a Rapidly Pitching Airfoil,” 44th AIAA Fluid Mechanics Conference, Dallas, TX, June 2015.
- Hemati MS, Dawson STM, and Rowley CW, “Unsteady Aerodynamic Response Modeling: A Parameter-Varying Approach,” 53rd AIAA Aerospace Sciences Meeting, Kissimmee, FL, January 2014.

DISTRIBUTION A: Distribution approved for public release.

- Monnier B, Williams DR, Weier T, and Albrecht T, “Comparison of a Separated Flow Response to Localized and Global-type Disturbances,” *International Journal of Flow Control*, AIAA paper 2015-1056
- Williams DR, Reissner F, Greenblatt D, Muehler-Vahl H, and Strangfeld C, “Modeling Lift Hysteresis with a Modified Goman-Khrabrov Model on Pitching Airfoils,” AIAA Paper 2015-2631.

1.3.2 Students and postdocs supported

The following students and postdocs were supported at least partially by this grant:

- Scott Dawson (current Ph.D. student, Princeton)
- Xuanhong An (current Ph.D. student, IIT)
- Simeon Iliev (M.S. 2015, IIT)
- Florian Reissner (M.S. 2015, TU Berlin)
- Lou Grimaud (M.S. 2014, IIT)
- Mark Luchtenburg (postdoc, Princeton)
- Steven Brunton (Ph.D. 2012, then postdoc, Princeton)

Chapter 2

Background and motivating results

This section will introduce some concepts that are relevant to, and will be used and referred to on a number of occasions throughout this report. Section 2.1, presents a range of algorithms that have seen common use for identifying models and features of fluids systems. Relevant literature and applications of such methods are discussed in detail in Section 1.2.

Of each of these methods, that which is utilized more predominantly in this report is DMD, which is featured to various extents in each of chapters 3, 4, 5, and 6. Additionally, Galerkin projection, which utilizes POD modes as an efficient basis for approximating the governing equations, is used in Chapter 5 as a comparison to the EDMD method of nonlinear system identification. We include a presentation of ERA both since it is used in Section 2.2, and to highlight the similarities with DMD; similarities which exist between numerous data-driven linear modeling/system identification algorithms.

2.1 Data-driven modeling of fluids systems

2.1.1 Proper orthogonal decomposition

The goal of the proper orthogonal decomposition (POD) is to obtain a set of empirical spatial modes that optimally represent a given dataset from an energetic standpoint. Assume that we can decompose the dynamics of some system $\mathbf{u}(x, t)$ (which could be the time-varying velocity field of a fluid, say) by

$$\mathbf{u}(x, t) = \mathbf{u}_0(x) + \sum_{i=1}^{\infty} \mathbf{u}_i(x) a_i(t), \quad (2.1.1)$$

where $\mathbf{u}_0(x)$ is some fixed (often average) data, and $\{\mathbf{u}_i(x)\}_{i=1}^{\infty}$ are a set of orthonormal basis functions (modes). POD takes these modes to be those which successively capture the most energy of the velocity field. Each POD mode \mathbf{u}_i satisfies the integral

$$\int_{\Omega} R_{i,j}(x, x') \mathbf{u}_i(x') dx' = \lambda \mathbf{u}_i(x),$$

where $R_{i,j}(x, y) = E[\mathbf{u}_i(x) \mathbf{u}_j(y)]$, with E being the expectation. As indicated by Eq. (5.2.1), POD is normally performed after first subtracting the mean (or perhaps an equilibrium point) from the data. This approach has the advantage that \mathbf{u}_0 satisfies the required non-homogeneous boundary conditions, meaning that all other modes \mathbf{u}_i will satisfy homogenous boundary conditions, so any linear combination of modes of the form given by Equation (5.2.1) will automatically satisfy

the correct boundary conditions of the problem at hand. In discrete terms, if we arrange finite-dimensional data collected from a simulation or experiment into a matrix $\mathbf{Y}^\#$, with each column representing a snapshot of data at a given time, then the POD modes are the columns of \mathbf{U} in the singular value decomposition $\mathbf{Y}^\# = \mathbf{U}\mathbf{\Sigma}\mathbf{V}^*$. Here the i^{th} entry of the diagonal matrix $\mathbf{\Sigma}$ corresponds to the energy contained in the i^{th} POD mode. In this discrete formulation, for simplicity we are omitting any rescaling of the data that should be performed so that the modes are orthonormal with respect to the usual inner product. That is, if \mathbf{u}_i and \mathbf{u}_j are columns of \mathbf{U} , then we really should have

$$\int_{\Omega} \mathbf{u}_j^*(x') \mathbf{u}_i(x') dx' \approx \sum_{k=1}^n \mathbf{u}_j^*(x_k) \mathbf{u}_i(x_k) dx_k = \delta_{ij},$$

rather than $\mathbf{u}_j^* \mathbf{u}_i = \delta_{ij}$. The original data $\mathbf{Y}^\#$ can then be represented in terms of POD coefficients by $\tilde{\mathbf{Y}}^\# = \mathbf{U}^* \mathbf{Y}^\#$. If we wish to reduce the dimension of this data, we may do so in an optimal way (with respect to energy content) by simply truncating the columns of \mathbf{U} beyond a certain point, which corresponds to removing POD modes that are of sufficiently low energy. Doing this gives a reduced order approximation of the data $\tilde{\mathbf{Y}}_r^\# = \mathbf{U}_r^* \mathbf{Y}^\#$, where \mathbf{U}_r contains the first r columns of \mathbf{U} . Note that there are alternative truncation techniques that may be more effective than energy maximization for certain applications, for example balanced POD [112] gives a reduced order linear state space model that is optimal with respect to a given set of sensors and actuators.

2.1.2 Galerkin projection

The idea behind GP is to approximate the governing PDEs that describe a given system with a low-dimensional set of ODEs. This is accomplished by projecting the equations onto spatial POD modes identified using the methods described in Sect. 5.2.1. We begin with the incompressible Navier–Stokes equations:

$$\begin{aligned} \frac{\partial \mathbf{u}}{\partial t} &= -(\mathbf{u} \cdot \nabla) \mathbf{u} - \nu \Delta \mathbf{u} - \nabla P \\ \nabla \cdot \mathbf{u} &= 0. \end{aligned} \quad (2.1.2)$$

If we take the (spatial) inner product of Eq. (5.2.2) with a given mode \mathbf{u}_j , we obtain

$$\left\langle \frac{\partial \mathbf{u}}{\partial t}, \mathbf{u}_j \right\rangle = -\langle (\mathbf{u} \cdot \nabla) \mathbf{u}, \mathbf{u}_j \rangle - \nu \langle \Delta \mathbf{u}, \mathbf{u}_j \rangle - \langle \nabla P, \mathbf{u}_j \rangle. \quad (2.1.3)$$

Substituting in the finite-dimensional approximation of Eq. (5.2.1), we obtain

$$\dot{\mathbf{a}} = \mathbf{L}\mathbf{a} + \mathbf{Q}(\mathbf{a}, \mathbf{a}) + \mathbf{f}, \quad (2.1.4)$$

where \mathbf{L} is a linear operation (i.e., a matrix), \mathbf{Q} is a bilinear operator (which can be represented as a 3-tensor), and \mathbf{f} is a vector, each defined based on the identified spatial POD modes by

$$\mathbf{L}_{ij} = -\nu \langle \Delta \mathbf{u}_j, \mathbf{u}_i \rangle, \quad \mathbf{Q}_{ijk} = -\langle (\mathbf{u}_j \cdot \nabla) \mathbf{u}_k, \mathbf{u}_i \rangle, \quad \mathbf{f} = -\langle \nabla p, \mathbf{u}_i \rangle. \quad (2.1.5)$$

This gives a means of approximating the Navier–Stokes equations by a set of nonlinear ODEs. As mentioned in Sect. 6.1, there are many modifications that have been proposed for this general procedure, most typically to account for the energy transfer to unmodeled modes (i.e., the energy cascade to finer spatial scales). For cases where spatial symmetries exist (e.g., in the streamwise and azimuthal directions for circular pipe flow), one can show that the POD modes must become Fourier modes, which can simplify their computation. It is also possible to “factor out” such symmetries by using an optimally chosen moving frame of reference [114, 117].

2.1.3 Dynamic mode decomposition

DMD has undergone a number of formulations, interpretations and modifications since its inception. Common to all methods is the requisite collection and arrangement of data, summarized now. Suppose we collect snapshots of data \mathbf{y}_i , which we assemble as columns in the data matrix \mathbf{Z} . For fluids systems \mathbf{y}_i will typically be a velocity field snapshot, but more generally it is a vector of observations of an evolving dynamical system at a given time. From \mathbf{Z} , we select all pairs of columns that are sampled at a time difference Δt apart, and place them into the matrices \mathbf{Y} and $\mathbf{Y}^\#$ (where the data in a given column of $\mathbf{Y}^\#$ was collected Δt after the equivalent column of \mathbf{Y}). Note that if \mathbf{Z} consists of a sequential time-series of data, then \mathbf{Y} and $\mathbf{Y}^\#$ are simply \mathbf{Z} with the last and first columns excluded, respectively. Let \mathbf{Y} and $\mathbf{Y}^\#$ each be n by m matrices, so we have m pairs of snapshots, each of size n . By not explicitly requiring a single time-series of data, we allow for larger or irregular time gaps between snapshot pairs, the concatenation of data from multiple time-series, and for the removal of any corrupted or spurious data. Recently, Tu et al. [149] proposed an interpretation of DMD modes and eigenvalues as the eigendecomposition of the matrix

$$\mathbf{A} = \mathbf{Y}^\# \mathbf{Y}^+, \quad (2.1.6)$$

where \mathbf{Y}^+ denotes the Moore–Penrose pseudoinverse of a matrix \mathbf{Y} . While this is a succinct interpretation, and one which will be useful in the ensuing analysis, it is typically not an efficient (or even feasible) means of performing DMD (as discussed in [149]). This is especially true when $n \gg m$, which is often the case in high-dimensional fluids systems. Instead, since \mathbf{Y} and $\mathbf{Y}^\#$ have rank at most $\min(m, n)$, it is typically more efficient to first project the data onto a subspace that is (at most) of this dimension. One way to do this is by projecting the original snapshots onto the POD modes of the data, which is implicitly done in all DMD algorithms. Note that the POD modes of \mathbf{Y} are the columns of \mathbf{U} in the singular value decomposition $\mathbf{Y} = \mathbf{U}\mathbf{\Sigma}\mathbf{V}^*$ (though typically POD is performed after first subtracting the temporal mean of the data, which is not done here). We present here a typical algorithm to compute DMD, that is most similar to that proposed in [149] as *exact* DMD.

Algorithm 1 (DMD).

1. Take the reduced singular value decomposition (SVD) of \mathbf{Y} , letting $\mathbf{Y} = \mathbf{U}\mathbf{\Sigma}\mathbf{V}^*$.
2. (Optional) Truncate the SVD by only considering the first r columns of \mathbf{U} and \mathbf{V} , and the first r rows and columns of $\mathbf{\Sigma}$ (with the singular values ordered by size), to obtain \mathbf{U}_r , $\mathbf{\Sigma}_r$, and \mathbf{V}_r .
3. Let $\tilde{\mathbf{A}} := \mathbf{U}_r^* \mathbf{Y}^\# \mathbf{V}_r \mathbf{\Sigma}_r^{-1}$.
4. Find the eigenvalues μ_i and eigenvectors w_i of $\tilde{\mathbf{A}}$, with $\tilde{\mathbf{A}} w_i = \mu_i w_i$.
5. Every nonzero μ_i is a DMD eigenvector, with a corresponding DMD mode given by $\varphi_i := \mu_i^{-1} \mathbf{Y}^\# \mathbf{V}_r \mathbf{\Sigma}_r^{-1} w_i$.

This method is similar to the original formulation in [126], but for the fact that in step 5 the DMD modes are no longer restricted to lie within the column space of \mathbf{Y} . We also explicitly provide the optional step of truncating the SVD of \mathbf{Y} , which might be done if the system is known to exhibit low dimensional dynamics, or in an attempt to eliminate POD modes that contain only noise. We note that this is not the only means to reduce the dimension of the identified system dynamics, nor is it necessarily optimal. Indeed, [164] develops a method that optimizes the

projection basis in parallel while performing a DMD-like eigendecomposition. [71] takes a different approach, seeking a small number of nonzero modes from the full eigendecomposition that best approximate the system dynamics. An empirical comparison between these various dimensionality-reduction techniques will be given in Sect 6.3.3. Note that the continuous eigenvalues λ_{ci} of the system are related to the discrete time eigenvalues identified via DMD via $\lambda_{ci} = \log(\mu_i)/\Delta t$. The growth rate γ_i and frequency ω_i associated with DMD mode φ_i are then given by $\lambda_{ci} = \gamma_i + i\omega_i$.

The matrix $\tilde{\mathbf{A}}$ is related to \mathbf{A} in Eq. (6.2.1) by $\tilde{\mathbf{A}} = \mathbf{U}_r^* \mathbf{A} \mathbf{U}_r$. While \mathbf{A} can be viewed as an approximating linear propagation matrix in \mathbb{R}^n (i.e., the space of original data vectors), $\tilde{\mathbf{A}}$ is the equivalent propagation matrix in the space of POD coefficients, which we will sometimes refer to as POD space. Another interpretation of $\tilde{\mathbf{A}}$ is that it is the spatial correlation matrix between the POD modes \mathbf{U}_r , and the same POD modes shifted by the assumed dynamics \mathbf{A} [126]. If we let $\tilde{\mathbf{x}}_k = \mathbf{U}_r^* \mathbf{x}_k$ be the representation of a given snapshot \mathbf{x} in the POD basis and let $\tilde{\mathbf{Y}} = \mathbf{U}_r^* \mathbf{Y}$ and $\tilde{\mathbf{Y}}^\# = \mathbf{U}_r^* \mathbf{Y}^\#$, then it is easy to verify that the equivalent of Eq. (6.2.1) in POD space is

$$\tilde{\mathbf{A}} = \tilde{\mathbf{Y}}^\# \tilde{\mathbf{Y}}^+ \quad (2.1.7)$$

Eq. (6.2.2) will be useful for the subsequent analysis performed in this paper.

2.1.4 Eigensystem realization algorithm

The eigensystem realization algorithm (ERA) is a method that extracts a linear state space model from impulse response data. As mentioned in section 1.2, it was first conceived for analyzing the structural dynamics of spacecraft in Juang and Pappa [72], but also shares close similarities with a number of previously proposed techniques [e.g., 65, 82]. More details about a range of similar methods and their potential applications can be found in [151, 152, 109].

The output of ERA is a discrete-time linear state-space system, taking the form.

$$\begin{aligned} \mathbf{x}_{k+1} &= \mathbf{A}_d \mathbf{x}_k + \mathbf{B}_d \mathbf{u}_k \\ \mathbf{y}_k &= \mathbf{C}_d \mathbf{x}_k + \mathbf{D}_d \mathbf{u}_k, \end{aligned} \quad (2.1.8)$$

The ERA algorithm proceeds as follows:

1. Collect output data from an impulse response of the form $\{\mathbf{y}_0, \mathbf{y}_P, \mathbf{y}_{2P}, \dots, \mathbf{y}_{m_P}\}$ and $\{\mathbf{y}_1, \mathbf{y}_{P+1}, \mathbf{y}_{2P+1}, \dots, \mathbf{y}_{m_P+1}\}$
2. Assemble the block Hankel matrices

$$\mathbf{H} = \begin{bmatrix} \mathbf{y}_0 & \mathbf{y}_P & \mathbf{y}_{2P} & \cdots & \mathbf{y}_{m_c} \\ \mathbf{y}_P & \mathbf{y}_{2P} & \mathbf{y}_{3P} & \cdots & \mathbf{y}_{(m_c+1)} \\ \vdots & \vdots & \vdots & \ddots & \vdots \\ \mathbf{y}_{m_o P} & \mathbf{y}_{(m_o+1)P} & \mathbf{y}_{(m_o+2)P} & \cdots & \mathbf{y}_{(m_o+m_c)P} \end{bmatrix},$$

$$\mathbf{H}^\# = \begin{bmatrix} \mathbf{y}_1 & \mathbf{y}_{P+1} & \mathbf{y}_{2P+1} & \cdots & \mathbf{y}_{m_c P+1} \\ \mathbf{y}_{P+1} & \mathbf{y}_{2P+1} & \mathbf{y}_{3P+1} & \cdots & \mathbf{y}_{(m_c+1)P+1} \\ \vdots & \vdots & \vdots & \ddots & \vdots \\ \mathbf{y}_{m_o P+1} & \mathbf{y}_{(m_o+1)P+1} & \mathbf{y}_{(m_o+2)P+1} & \cdots & \mathbf{y}_{(m_o+m_c)P+1} \end{bmatrix},$$

where m_c and m_o are chosen such that $m_c + m_o \leq m$.

3. Compute the (reduced) SVD $\mathbf{H} = \mathbf{U} \mathbf{\Sigma} \mathbf{V}^T$.

DISTRIBUTION A: Distribution approved for public release.

4. Truncate the SVD by only considering the first r columns of \mathbf{U} and \mathbf{V} , and the first r rows and columns of $\mathbf{\Sigma}$ (with the singular values ordered by size), to obtain \mathbf{U}_r , $\mathbf{\Sigma}_r$, and \mathbf{V}_r , where r is the desired model order.
5. The matrices of the reduced-order model of a system with p inputs and q outputs are given by

$$\begin{aligned} \mathbf{A}_r &= \mathbf{\Sigma}_r^{-1/2} \mathbf{U}_r^T \mathbf{H} \mathbf{V}_r \mathbf{\Sigma}_r^{1/2}, \\ \mathbf{B}_r &= \text{the first } p \text{ columns of } \mathbf{\Sigma}_r^{1/2} \mathbf{V}_r^T, \\ \mathbf{C}_r &= \text{the first } q \text{ rows of } \mathbf{U}_r \mathbf{\Sigma}_r^{1/2}, \\ \mathbf{D}_r &= \mathbf{y}_0. \end{aligned} \quad (2.1.9)$$

Note that when $p = 1$, the data pairs in step 1 can just be taken from an impulse response sequence with its last and first entries removed. This more general formulation allows for the skipping of data when assembling \mathbf{H} , which can reduce computational costs, while still allowing data to be used across a large total time window.

In general, input-output data might not be available in the form of an impulse response, in which case other more general subspace methods may be used (e.g., Verhaegen and Dewilde [151]). Another approach is to use a technique such as observer/Kalman filter identification [74] to compute an impulse response from input-output data with random inputs, before applying ERA. We note that there are close similarities between DMD and ERA. Indeed, the two algorithms become equivalent when $m_o = 1$, in the sense that the \mathbf{A} matrices from either method are only different by a similarity transform [149].

2.2 Motivating results

Here, we present some preliminary results that will serve as motivation for the research in the following chapters. The main idea will be to use ERA to identify models for a pitching airfoil system, and use these models to design feedback controllers that allow for the lift to be controlled. The core methodology behind these results is given in Brunton et al. [23]. For brevity, we defer a detailed discussion of the experimental and numerical methods to Chapters 3 and 4 respectively.

We consider an airfoil undergoing simple pitching motion about the quarter chord, with the system input being the kinematics of the airfoil (captured by the angular acceleration, $\ddot{\alpha}$) and the output the lift coefficient, $C_L = \frac{F_L}{0.5\rho A U_\infty^2}$. Models (in the form of low order state-space realizations of the system) are identified by applying the eigensystem realization algorithm to discrete-time impulse response data. This occurs after first extracting the components of the lift that are directly proportional to the angle of attack and its derivatives (α , $\dot{\alpha}$, and $\ddot{\alpha}$), described in further detail in [?]. For direct numerical simulations, such impulse response data is directly simulated, while in experiments it is acquired by applying the observer/Kalman filter identification algorithm (OKID) to the input/output data from pseudo-random, frequency rich maneuvers. Feedback controllers are designed using H_∞ loopshaping, with a desired loopshape given by

$$G_d = \frac{180a^2(s + 1.5a)}{s^2(s + 30a)}, \quad (2.2.1)$$

where the parameter a determines the bandwidth of the controller. This procedure can be applied using both theoretical models (such as the Theodorsen model) and the previously discussed reduced order models, identified in both direct numerical simulations (DNS) and wind tunnel experiments. Simulations are performed on a two-dimensional flat plate airfoil at a Reynolds Number of 100,

DISTRIBUTION A: Distribution approved for public release.

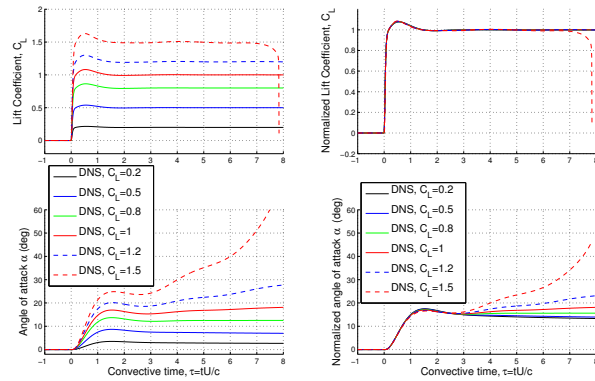


Figure 2.1: (left) Step responses of various magnitude for the closed-loop system in DNS, and (right) Normalized step responses. Linear behavior in the output (lift coefficient) is observed, despite large nonlinearities present in the system, which is evident from the variation in the angle of attack plots.

using an immersed boundary projection method ([139, 34]). Experiments were conducted using a NACA0006 airfoil of chord length 0.245m with a free stream velocity of 3 m/s, giving a Reynolds number of approximately 50,000. Gusting conditions are generated in the wind tunnel by using a series of shutters downstream of the test section. In spite of the differences in parameters and conditions between the DNS and experimental work, we demonstrate that the same control methodology can be successfully applied in both cases.

Feedback control is implemented for tracking reference lifts of a range of magnitudes, both with and without the presence of gusting disturbances. To begin with, we consider tracking step changes in reference lift in DNS. Figure 2.1 shows accurate tracking of the desired lift over a range of magnitudes, even significantly beyond the maximum value that can be held in steady conditions ($C_L = 0.97$). This highlights one of the major benefits of using feedback control: even though the system is clearly non-linear, we are able to make the output (which is often what we care most about) behave linearly. Here the nonlinear effects are compensated for by the controller modifying the input to the system. Figure 2.2 shows lift tracking step responses for experimental conditions. The presence of noise and time lags in the system degrades the performance. Nonlinear effects further limit the performance for high amplitude steps.

Figure 2.3 shows experimental data, where feedback control is used to track a constant, high magnitude lift in the presence of 10% periodic fluctuations in the freestream velocity. Despite not receiving any direct information about the disturbance, the controller is able to correct for

DISTRIBUTION A: Distribution approved for public release.

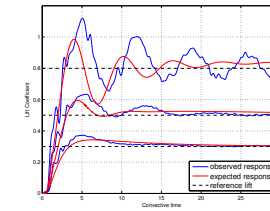


Figure 2.2: Step responses of various magnitude for the closed-loop system in wind tunnel experiments. The controller performance degrades for high-amplitude steps

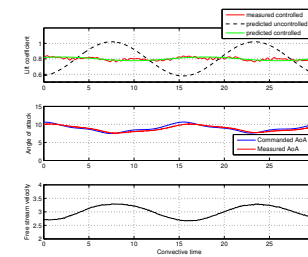


Figure 2.3: Tracking a lift coefficient of 0.8 in wind tunnel experiments in the presence of periodic gusts.

the changes in lift coefficient that are caused by the fluctuating free stream velocity, in order to maintain a nearly constant lift. The performance closely agrees with predictions that can be made using identified models for the gust disturbance.

Having validated that feedback control can be successfully implemented on simple step maneuvers, we proceed to investigate more complex desired lift profiles. Figure ?? shows the performance of the DNS system in tracking a sinusoidally varying reference lift. Interestingly, we note that the addition of a periodic component to the reference lift at certain frequencies allows for successful tracking of a higher average lift. In particular,

While these results show one use for reduced order models, they also suggest a few limitations of such an approach. Firstly, accurate lift tracking was only possible when an accurate, real-time lift measurement was available. This is primarily due to the fact that the system is nonlinear. This motivates the development of nonlinear modeling procedures considered in Chapters 3 and 5.

DISTRIBUTION A: Distribution approved for public release.

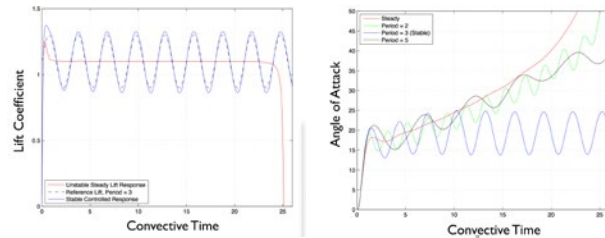


Figure 2.4: Controller performance in tracking sinusoidally varying reference lift coefficient.

Figure 2.4 exposes some interesting flow physics for this particularly pitching airfoil system, where higher average lift coefficients are found when pitching at a preferred frequency. This phenomena is explored systematically in Chapter 4.

We also observe a degradation of performance when using experimental, rather than numerical data. Aside from issues with implementing feedback control in experimental systems that contain time lags between command and actuation, one cause of this degradation is the presence of noise in the data. This is particularly important when it is data that is being used to identify models. We study the presence of noise in the dynamic mode decomposition in Chapter 6, and propose modified algorithms that can give improved performance with noisy data.

DISTRIBUTION A: Distribution approved for public release.

Chapter 3

A data-driven modeling framework for predicting forces and pressures on a rapidly pitching airfoil

This work formulates a switched linear modeling procedure to understand and predict the unsteady aerodynamic forces arising from rapid pitching motion of a NACA 0012 airfoil at a Reynolds number of 50,000. The system identification procedure applies a generalized dynamic mode decomposition algorithm to time-resolved wind tunnel measurements of the lift and drag forces, as well as the pressure at six locations on the suction surface of the airfoil. Linear state space models are identified for 5-degree pitch-up and pitch-down maneuvers within an overall angle of attack range of 0° – 20° . The identified models accurately capture the effects of flow separation and leading-edge vortex formation and convection. It is shown that switching between different linear models can give accurate prediction of the nonlinear behavior that is present in high-amplitude maneuvers. The models are accurate for a wide range of motions, including pitch-and-hold, sinusoidal, and pseudo-random pitching maneuvers. Providing the models access to a subset of the measured data channels can allow for improved estimates of the remaining states via the use of a Kalman filter, which could be of use for aerodynamic control applications.

3.1 Introduction

The flight of small, highly maneuverable aircraft, whether biological or manmade, is greatly impacted by unsteady aerodynamic effects, which can be either beneficial or detrimental to flight. Accurate understanding of such effects can allow for the design of aircraft that are more efficient, responsive, and robust.

The need to account for unsteady effects has been recognized since soon after the breakthrough of powered manmade flight, in the classical works of Wagner [155], Theodorsen [142], and Garrick [50]. Indeed, many failed attempts at flight can probably be attributed to a severe lack of understanding of how to utilize such effects. These classical models give significant insight into the fundamental flow physics associated with unsteady flight, such as relative contributions to lift of the added mass, quasi-steady bound circulation, and wake vortices. While such models can be quantitatively accurate for cases of attached flow where viscous effects are negligible, they quickly lose validity when dealing with separated flows, which are often encountered in the extreme motions that are possible for birds, insects, and micro and unmanned aerial vehicles (MAV and UAV). It is precisely in these extreme cases that accurate predictive models are essential to prevent catastrophic failure

17

DISTRIBUTION A: Distribution approved for public release.

and ensure ongoing successful flight. While more accurate predictions can be attained from high-fidelity simulations, the computational cost typically prohibits the direct use of such simulations for real-time prediction and control.

Biological examples such as insects [18, 120, 156] and birds [153] have seemingly evolved to take advantage of the high transient lift force that can be generated due to the formation of a leading edge vortex (LEV) during rapid pitch-up motion, for example. While these give motivating examples of the advantages of accurate understanding of unsteady aerodynamic effects, the preferred wing kinematics arising from evolution is highly specific and coupled to the geometry and other physiological features of the animal. Indeed, the characteristics of unsteady aerodynamic effects, particularly for separated flows, seem to be quite sensitive to both the geometry [79] and Reynolds number [166] of the airfoils. Studies into low Reynolds number flow over stationary [166, 4, 165] and pitching [154, 1, 131, 30, 80] symmetric airfoils have revealed, for example, complex effects associated with the stability and separation of the suction surface boundary layer, which are again highly sensitive to Reynolds numbers. These observations motivate the development of general modeling procedures that can be easily applied to a range of parameter cases. In addition, it is desirable for such methods to be sufficiently general such that they can be applied to more realistic aircraft configurations, rather than just airfoils. As an example, such data driven modeling was considered for the case of accurate prediction and control of lift for a low Reynolds number pitching airfoil [22, 23], using the eigensystem realization algorithm [72] (ERA) and observer/Kalman filter identification [74] (OKID). There has also been a significant amount of work in terms of nonlinear modeling, ranging from low order state-space models formulated from theoretical considerations [54], to Volterra series models that have been used to model a range of unsteady aerodynamic and aeroelastic phenomena [132, 85, 11].

More generally, rapid advances in both computational power and experimental equipment has seen a large increase in the amount of data that can be generated by researchers in fluid mechanics. This has led to the increased popularity of techniques such as proper orthogonal decomposition [66] and dynamic mode decomposition [126] (DMD), which can be useful to extract tractable models and physical insight from large fluids datasets.

In the present work, we use a variant of DMD to identify linear state space models for a variety of pitch-up and pitch-down maneuvers. DMD was first introduced to the fluids community as a means to extract dynamic information from data [125], and has subsequently been successfully applied to a range of numerical and experimental fluids datasets [126, 128, 127, 70]. Numerous theoretical developments have highlighted DMD's connections to both Fourier [27] and Koopman [119] spectral analyses, and other system identification techniques such as ERA [149]. DMD's formulation has also been generalized to allow for the identification of systems with inputs [105], and it is this framework that we make use of in this work. One advantage of the present modeling approach is that, unlike those generated using ERA/OKID the model states can be directly related to measurements. This can allow easy switching between neighboring linear models, which subsequently permits the formation of a switched linear model that is capable of predicting nonlinear behavior. Our algorithm is described in section 3.2, which is followed by a description of the experimental setup in section 3.3. Section 5.4 demonstrates that the obtained models are accurate for a range of high-amplitude pitching maneuvers. Section 5.5 contains a more general discussion of the results and subsequent conclusions of this study.

DISTRIBUTION A: Distribution approved for public release.

3.2 System identification method

We use a variant of dynamic-mode decomposition to identify models describing the pitching airfoil, which is briefly described here. The goal will be to identify a family linear systems of the form

$$\mathbf{x}_{i+1} = \mathbf{A}_k \mathbf{x}_i + \mathbf{B}_k \mathbf{u}_i. \quad (3.2.1)$$

By identifying different \mathbf{A}_k and \mathbf{B}_k matrices for different angles of attack and directions of pitching, we can assemble a family of linear models $\{\mathbf{A}_k, \mathbf{B}_k\}_{k=1}^N$ that can subsequently be pieced together to allow for accurate prediction of maneuvers spanning a wider range of angles of attack than any single linear model would be capable of. We now describe in general terms the identification procedure for a linear model $\{\mathbf{A}, \mathbf{B}\}$. Further details concerning the specific data chosen to constitute the state \mathbf{x} will be given in Section 3.4.1.

Suppose we collect a time-series of measurements \mathbf{x}_i , which we assemble as columns into a matrix \mathbf{X} . From \mathbf{X} , we select all pairs of data that are separated by some nominal time Δt , which we assemble into matrices \mathbf{X}_1 and \mathbf{X}_2 . If \mathbf{X} consists of uniformly sampled data, then \mathbf{X}_1 and \mathbf{X}_2 are \mathbf{X} with the last and first columns removed, respectively. Standard DMD can be characterized as finding the eigendecomposition of a matrix \mathbf{A} satisfying (or approximately satisfying) $\mathbf{X}_2 = \mathbf{A} \mathbf{X}_1$ [149]. Depending on the size of \mathbf{X}_1 and \mathbf{X}_2 , \mathbf{A} is either the (Frobenius) minimum-norm solution (if the data matrices have more rows than columns), or the least-squares solution (otherwise). The usefulness and validity of this approach relies assumption that the system is autonomous, and not greatly affected by external inputs. If we have known inputs \mathbf{u}_i assembled into a matrix \mathbf{U} , then it is possible to modify DMD [105] to instead seek the matrices \mathbf{A} and \mathbf{B} satisfying

$$\mathbf{X}_2 = [\mathbf{A} \ \mathbf{B}] [\mathbf{X}_1 \ \mathbf{U}]. \quad (3.2.2)$$

Provided that the size of the state m is not excessive, we may compute the augmented system matrices $[\mathbf{A} \ \mathbf{B}]$ through

$$[\mathbf{A} \ \mathbf{B}] = \mathbf{X}_2 [\mathbf{X}_1 \ \mathbf{U}]^+, \quad (3.2.3)$$

where $+$ denotes the Moore-Penrose pseudoinverse. Since fluids systems are, in general, nonlinear, the ability of the identified linear system in accurately modeling all data may be limited. However, an intelligent selection of state variables \mathbf{x} can go a considerable way towards factoring out much of the nonlinearity in the system. To begin with, rather than directly using force and pressure measurements, we can instead consider deviations from the equilibrium (or mean) values at a given angle of attack. This allows for the resulting linear model to be accurate despite nonlinear static behavior.

3.3 Experimental method

Experiments were conducted at the Andrew Fejer wind tunnel at the Illinois Institute of Technology, with a diagram of the airfoil mounting shown in figure 3.1. A NACA 0012 airfoil of chord length $c = 0.245\text{m}$ was used in a test section of length 3m and cross-section 0.6m by 0.6m. The airfoil spanned the width of the test-section, thus minimizing three-dimensional effects. The airfoil was mounted upon a six-axis ATI nano17 force transducer, which allowed for the measurement of time-resolved forces and moments. This, in turn, was mounted upon two pushrods actuated by Copley servo tubes, allowing for pitching motion to be commanded. For the results presented here, only the rear pushrod was actuated, which resulted in pitching about an axis 0.11c from the leading edge.

DISTRIBUTION A: Distribution approved for public release.

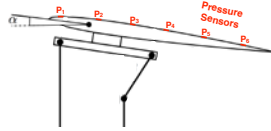


Figure 3.1: Schematic of the experimental setup.

Six pressure taps were installed along the chord of the airfoil at one spanwise location, located at distances of $0.050c$, $0.217c$, $0.385c$, $0.552c$, $0.720c$, and $0.887c$ aft of the leading edge. The freestream velocity was measured using a pitot tube and remained constant at a nominal value of 3m/s , giving a Reynolds number $\frac{\rho U}{\mu}$ of approximately $50,000$, and a convective time $t_c = \frac{c}{U} = 0.0817\text{s}$. Note that some blockage effects meant that the freestream velocity changed by a small amount as the angle of attack changed (approximately 3% when pitching between 0° and 20°). All forces and pressures were nondimensionalized using the averaged velocity at the relevant phase of the maneuver. (Note that this neglects unsteady effects associated with the changing velocity, but since the changes are small, these effects should be negligible.)

Force and pressure data was acquired at a frequency of 1000Hz . For each maneuver, data was phase-averaged over at least 50 cycles to reduce the effect of measurement noise. All maneuvers were also performed with the wind tunnel off before and after data was collected with the tunnel switched on. These results were also phase-averaged, and subtracted from the tunnel-on data. This eliminates (for the force readings) the effects of the mass of the wing, the added-mass terms associated with accelerating the surrounding air, and also any other effects on the measurement equipment resulting directly from the maneuver performed. By eliminating added-mass terms, we isolate the circulatory fluids forces arising from a given pitching maneuver.

3.4 Results

Here results are presented for the identification (Section 3.4.1) and performance of the suite of identified models. To test the performance of the family of models that have been identified, we analyze their ability to predict a range of other maneuvers. These range from compositions of similar individual maneuvers (Section 3.4.2), to sinusoidal (Section 3.4.3) and pseudo-random (Section 3.4.4) pitching maneuvers. The latter two of classes of maneuver bear little similarity to the maneuvers used for identification. In this sense, we will be able to show the generality of these models, which highlights that the identified models represent more than simply fits to the data, and have predictive capabilities.

3.4.1 System identification results

Models were identified separately from pitch-up and pitch-down maneuvers between 0° – 5° , 5° – 10° , 10° – 15° , and 15° – 20° , with model states obtained from the 6 pressure readings and the lift and

DISTRIBUTION A: Distribution approved for public release.

drag measurements. The prescribed maneuvers take the canonical form[47]

$$\alpha(t) = \frac{MG}{\max(G)}, \quad G = \log \left[\frac{\cosh(a(t-t_1)) \cosh(at_2)}{\cosh(a(t-t_2)) \cosh(at_1)} \right]. \quad (3.4.1)$$

Nondimensionalizing time by $\frac{U}{c}$, we take $t_2 - t_1 = 2$, and $a = \frac{10U}{c} = 122.4$ (and $M = 5^\circ$). With these parameter values, a becomes the main governing parameter that determines the rate of the step.

The duration of the pitch was approximately 4 convective times ($4\frac{c}{U}$). Static data at the corresponding angles of attack was first subtracted from all measurements, and all data was nondimensionalized (forces by $\frac{1}{2}\rho c U^2$ and pressures by $\frac{1}{2}\rho U^2$). To identify models, the DMD-type algorithm described above was used, which allows for data with inputs (which in this case was taken to be measurements of either α and $\dot{\alpha}$, or just $\dot{\alpha}$). Using this method, we arrive at models of the form

$$\mathbf{x}_{i+1} = \mathbf{A}\mathbf{x}_i + \mathbf{B}\mathbf{u}_i,$$

as described in Section 3.2. Here we let $\mathbf{x} = [\hat{C}_{p1} \ \hat{C}_{p2} \ \dots \ C_{p6} \ \hat{C}_l \ \hat{C}_d]^T$, and $\mathbf{u} = [\alpha \ \dot{\alpha}]^T$. Note that while we treat α as an input for convenience, the fact that it is entirely dependent on $\dot{\alpha}$ means that we could also treat it as an additional system state. Here $\hat{\cdot}$ represents the deviation from an equilibrium condition, $\hat{C}_i = C_i - C_i^e(\alpha)$, where $C_i^e(\alpha)$ is the equilibrium value at a given angle of attack. We first attain this equilibrium data for angles of attack in the range $\alpha \in [0^\circ, 22^\circ]$, which is shown in Figure 3.2. To motivate the development of unsteady models, we also show how data acquired for a pitching airfoil deviates from these equilibrium values. Considering just the static data, we observe that the lift coefficient increases close to linearly (with a slope of approximately 1.7π) between 0° and 8° , before the lift curve reaches its peak and then plateaus between 10° and 15° , before again increasing beyond 15° . The lift plateau corresponds to the airfoil stalling, with the flow over the suction surface becoming separated. Further evidence for this comes from examining both the drag curve, which sees a large increase in drag beyond $\alpha = 8^\circ$, and in the first two pressure coefficients, which give a sharp drop in pressure beyond this angle. Prior to full separation, there is evidence for partial separation towards the rear of the airfoil. Pressure sensors 3–6 all measure a drop in pressure at a critical angle between 2° and 6° , which appears to signify the separation point moving upstream of the given sensor.

Returning now to the system identification procedure, Figures 3.3 and 3.4 show the performance of each model in predicting the pressure and force coefficients for the maneuver upon which they were identified. For reference, the static pressure and force coefficients at the instantaneous angle of attack are also shown in Figures 3.3 and 3.4. Rather than subtracting the full static curves before system identification, we found improved results by assuming linear variation in the static values throughout the maneuver. This avoids issues with separation-related “jumps” occurring at different angles of attack in for the static and moving airfoil, which makes the static-subtracted data less smooth.

We can identify two dominant features of the pitch-up and pitch-down behavior. A temporary rise in C_l , C_d and $-C_p$ is observed which is consistent with the formation and convection of a leading-edge vortex (see e.g. all measurements for pitching between 15° and 20°), and a time-lag in reaching the steady state value, most likely due to the boundary layer requiring time to reach its new equilibrium configuration (see e.g. C_{p6} when pitching between 0° and 5°).

We finally note that we obtain quite different models for pitch-up and pitch-down maneuvers. To show this explicitly, Figure 3.5 shows the inaccuracy of the prediction of a 5 – 10° pitch-up

DISTRIBUTION A: Distribution approved for public release.

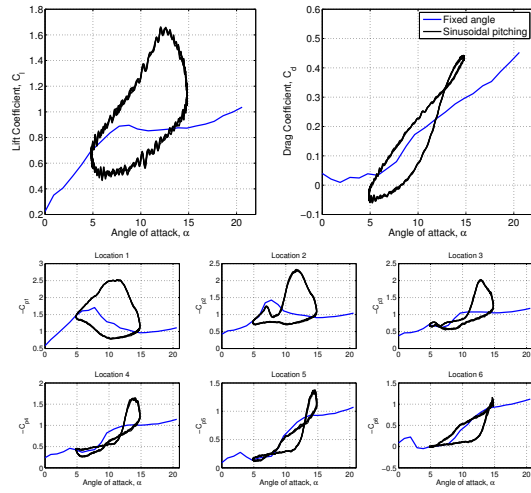


Figure 3.2: Force and pressure coefficient data for a static airfoil at angles of attack between 0° and 22° , as well as for an airfoil sinusoidally pitching between 5° and 15° at a rate $k = \frac{\pi}{U} = 0.051$.

DISTRIBUTION A: Distribution approved for public release.

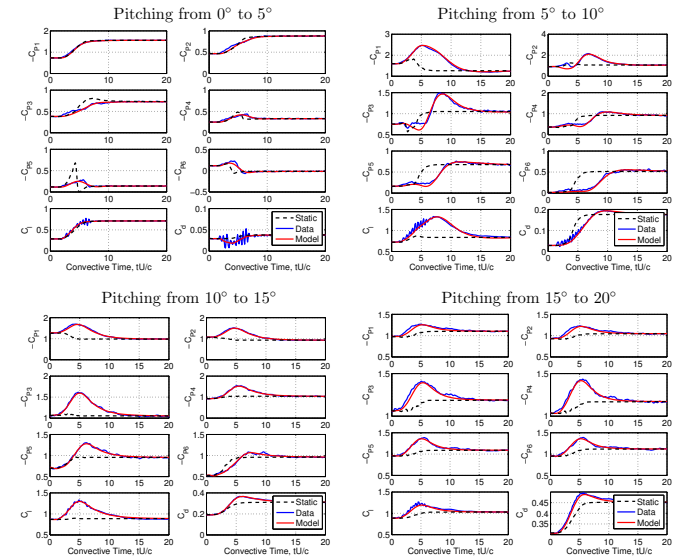


Figure 3.3: Force and pressure data for 5° pitch-up maneuvers for starting angles of 0° , 5° , 10° and 15° , which were used for system identification. In all cases, the identified models accurately replicate the experimental data. Also shown is the static data at the relevant instantaneous angle of attack.

DISTRIBUTION A: Distribution approved for public release.

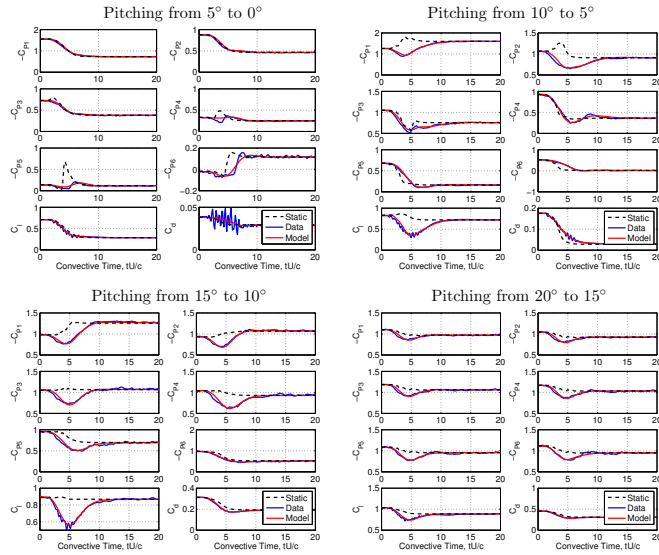


Figure 3.4: Force and pressure data for 5° pitch-down maneuvers for starting angles of 5° , 10° , 15° and 20° , which were used for system identification. In all cases, the identified models accurately replicate the experimental data. Also shown is the static data at the relevant instantaneous angle of attack.

DISTRIBUTION A: Distribution approved for public release.

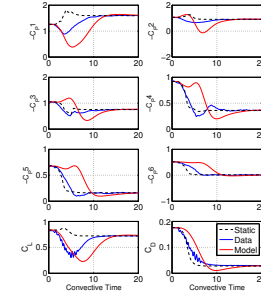


Figure 3.5: Example of inaccurate prediction of a pitch-up model ($5 - 10^\circ$ model, red curves) on pitch down maneuver ($10 - 5^\circ$ maneuver, blue curves).

model for a $10 - 5^\circ$ pitch-down maneuver, which arises primarily because the $5 - 10^\circ$ pitch-up model predicts the existence of a time-delay, which is not present in the $10 - 5^\circ$ pitch-down data. This has important implications for the use of pseudo-random system identification maneuvers, which necessarily incorporate both pitching up and pitching down motion.

3.4.2 Multiple pitch-up and pitch-down maneuvers

We now consider a maneuver consisting of two pitch-ups followed by two pitch-downs, each in rapid succession. We attempt to predict the maneuver by switching between the relevant models for each pitch-up and pitch-down. For this maneuver, four different models are used. Given that the state of each model consists of the same variables, this is simply a matter of switching the A and B matrices used to propagate the system.

The results for this procedure in predicting C_l , C_d , as well as two of the pressure coefficients are shown in Figure 3.6, where we have considered double pitch-up/down maneuvers between 10° and 20° with different pitching rates. We vary the a parameter from equation 3.4.1: to modify the pitching rate (halving and doubling it from the value used in system identification). In all cases, we switch between sub-models at $t = 10, 20$ and 30 convective times, using the final predicted state from one sub-model as the initial condition for the next. To give some basis for comparison, we show the performance of a single linear model (that identified from a $5 - 10^\circ$ pitch-up) in predicting this maneuver in Figure 3.7. We note that the only section of this maneuver that this model accurately predicts is that which is most similar to its identification maneuver.

Figure 3.8 shows a quadruple pitch-up and -down maneuver, which switches between all models. From all of these results, we find that switching between models generally works well, though sometimes it can induce “jumps” immediately after switching, particularly when switching between

DISTRIBUTION A: Distribution approved for public release.

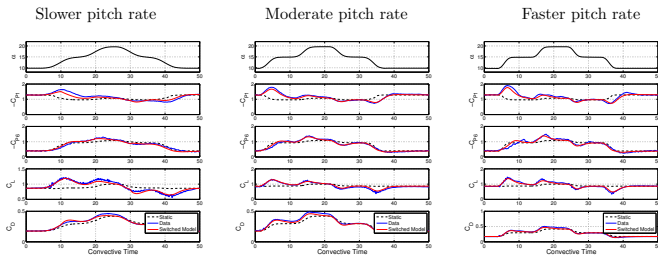


Figure 3.6: Switched model performance in predicting pressure and force coefficients for double pitch up/down maneuvers with different pitch-rates, between 10° and 20° . Switching between sub-models occurs at $t = 10, 20$ and 30 convective times, using the final predicted state from one sub-model as the initial condition for the next. The middle plot uses the same pitch-rate as the maneuvers used for system identification.

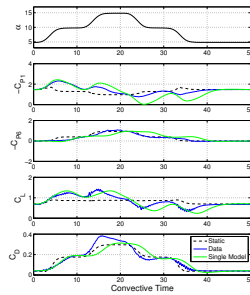


Figure 3.7: Performance of a single ($5\text{--}10^\circ$ pitch-up) model in predicting pressure and force coefficients for double pitch up/down maneuver.

DISTRIBUTION A: Distribution approved for public release.

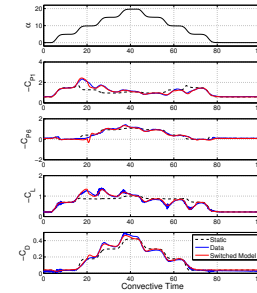


Figure 3.8: Performance of switched model in predicting pressure and force coefficients for quadruple pitch up/down maneuver. Switching between models occurs at multiples of 10 convective times between $t = 10$ and $t = 70$, where the final predicted state from one sub-model as the initial condition for the next.

the pitch-up and pitch-down models between 5° and 10° . It is possible that these could be eliminated or reduced by further refining the system identification and/ or switching procedure.

3.4.3 Sinusoidal pitching

Next, we consider high-amplitude sinusoidal pitching maneuvers, pitching between 0° and 20° at rates $f = 0.2$ Hz and 0.4 Hz, giving a reduced frequencies $k = \frac{\pi f c}{U} = 0.051$ and 0.103 . In Figure 3.9 we show the predicted pressures and forces when using a single model (arbitrarily taken to be the pitch-up model from 5° to 10°), a switched model, and a switched equipped with a Kalman filter (that gives access to the 1^{st} and 6^{th} pressure measurements). Details concerning the design of this Kalman filter are given in Appendix 1. We find that the switched model performs better than any single linear model, and that improved accuracy in all measurements can be achieved when using the Kalman filter. The latter observation demonstrates that, even if the models themselves have some inaccuracies in predicting the outputs, access to measurements of a subset of these outputs can improve the prediction of all outputs. This is relevant for the use of such models for real-time control, where, for example, we may seek to attain a desired lift force using only pressure measurements.

3.4.4 Pseudo-random pitching

We finally consider the case where the angle of attack varies in a pseudo-random manner. Figure 3.10 shows the performance of a switched model equipped with a Kalman filter in predicting the pressures and forces for a pseudo-random pitching maneuver. Again, we observe close agreement

DISTRIBUTION A: Distribution approved for public release.

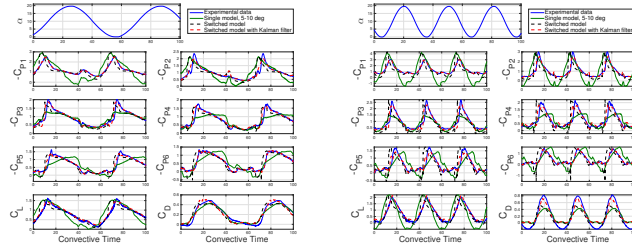


Figure 3.9: Predicted and actual pressure and force coefficients for high-amplitude sinusoidal pitching at dimensionless frequencies $k = \frac{\pi f c}{c} = 0.051$ and 0.103 . Predictions are made using a model both with and without a Kalman filter. When a Kalman filter is used, the model is given access to the 1st and 6th pressure measurements.

between the measured and predicted results. This close agreement highlights the full generality of the switched model, as it is capable of accurately predicting the behavior of the airfoil forces and pressures for arbitrary high-amplitude pitching motions.

3.5 Discussion and conclusions

The results presented in Section 5.4 demonstrate that the system identification technique described in Section 3.2 can be of use for unsteady aerodynamic modeling applications. The fact that accurate models were attained from very simple pitch-up and pitch-down maneuvers gives the procedure an advantage over the OKID algorithm, which typically requires a concatenation of a variety of motions to obtain accurate models[22]. The absence of internal states in the resulting models mean that they are naturally suited for piecing together for the formation of a global switched model. This process is difficult for ERA models, where the internal states are not directly associated with physical measurements. Having measurements directly associated with model states means that the dimension of the observables must be at least as large as the dimension of the underlying dynamics (or their approximating model), though this restriction could be relaxed if we were to concatenate the data with time-shifted measurements (as is done in ERA), or by using transformations of the original data [160]. Conversely, the fact that the models are accurate suggests that 8th order linear models are sufficient to capture the phenomena present in the maneuvers considered. Indeed, in many cases it was found that it was possible to apply balanced truncation to reduce the dimension of the identified models without significant degradation of predictive accuracy.

In general, linear modeling techniques are appealing due to the simplicity of their identification and formulation, and the ease of use in simulation and controller design. Their accuracy in the prediction of nonlinear dynamics, however, will typically be fundamentally limited to a region in phase-space that is near to the identification maneuver. Scheduling between a family of linear

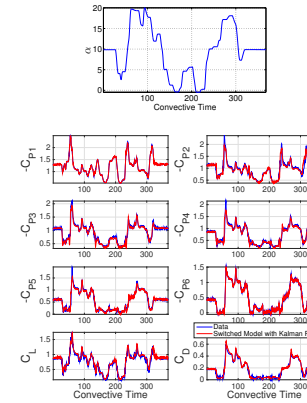


Figure 3.10: Performance of the switched model, equipped with a Kalman filter and measurements of the first and last pressure coefficient, in predicting pressure and force coefficients for high-amplitude pseudo-random pitching maneuver.

models can go some way to incorporating nonlinear effects into a global model, thus increasing the region in phase-space where such models are accurate. This work demonstrated that, in the α direction of phase-space, such an approach can work between 0° and 20° , which includes the regimes where the flow over the suction surface is completely attached, partially separated, and fully separated. This range was the maximum available given physical limitations of the airfoil mounting, but we imagine that separated flows at higher angles of attack should also be able to be accurately modeled, given that they are phenomenologically similar (in terms of being fully separated) to those near 20° .

In terms of the applicability of the model for maneuvers with different pitch-rates (i.e. the $\dot{\alpha}$ direction of phase space), we see in Figure 3.6 that the models remain accurate for a range of values of pitch rates. Looking at Figure 3.9, however, we see that switching between models while pitching at a relatively fast rate can lead to some degradation of model accuracy. This is a known limitation of gain scheduling models in general[130].

The fact that the acquired data was phase-averaged over a number of cycles means that any unsteady phenomena that are not phase-locked with the pitching motions will be averaged out of the identified models. Particularly for separated boundary layers, such effects (which can occur on a faster timescale to the pitching motions) can be significant, even if they are not directly controllable by pitching motion. Further work could, for example, incorporate such dynamics into state estimators, which could improve the real-time predictive power of such models.

The data that is obtained for the cases of a pitching and stationary airfoil is also of fundamental fluid mechanical interest, which will be further investigated by investigating the time-varying velocity field using particle image velocimetry (PIV). Specifically, it would be interesting to explore whether a small number of measurements could be used to accurately predict not only the pressures and forces (as was done in the present work), but also the entire velocity field in the vicinity of the airfoil.

Appendix 1: Kalman filter design

The linear models (taking the form given in equation 3.2.1) identified in this work give a prediction of forces and pressures given knowledge of the airfoil pitching kinematics. In some situations, it might be possible to supplement knowledge of these kinematics (i.e., the system inputs) with some number of additional measurements. This section briefly describes the setup and design of a Kalman filter[78], that is used to improve the estimate of the state of the system using such additional measurements. Suppose we have a state space system of the form

$$\begin{aligned}\mathbf{x}_{i+1} &= \mathbf{A}\mathbf{x}_i + \mathbf{B}\mathbf{u}_i + \mathbf{G}\mathbf{w}_i \\ \mathbf{y}_i &= \mathbf{C}\mathbf{x}_i + \mathbf{D}\mathbf{u}_i + \mathbf{H}\mathbf{w}_i + \mathbf{v}_i,\end{aligned}$$

which is a generalization of equation 3.2.1 to include the influence of plant disturbances \mathbf{w} , as well as an output equation that includes sensor noise \mathbf{v} . For the purposes of this work, we will assume that $\mathbf{H} = 0$, $\mathbf{D} = 0$, and \mathbf{C} is a matrix that selects a subset of the states \mathbf{x} as outputs. The Kalman filter gives an estimate of the state $\hat{\mathbf{x}}$ from the system inputs \mathbf{u} and (potentially noisy) measurements \mathbf{y} , whose dynamics are governed by the equation

$$\hat{\mathbf{x}}_{i+1} = \mathbf{A}\hat{\mathbf{x}}_i + \mathbf{B}\mathbf{u}_i + \mathbf{L}(\mathbf{y}_i - \mathbf{C}\hat{\mathbf{x}}_i - \mathbf{D}\mathbf{u}_i).$$

Here the matrix \mathbf{L} gives the optimal state estimate for given disturbance and noise covariance matrices, $\mathbf{Q} = E(\mathbf{w}\mathbf{w}^T)$ and $\mathbf{R} = E(\mathbf{v}\mathbf{v}^T)$, respectively. Further details concerning Kalman filter

DISTRIBUTION A: Distribution approved for public release.

design and the computation of \mathbf{L} may be found in standard optimal control textbooks[136]. For this work, we take \mathbf{Q} and \mathbf{R} to be appropriately sized diagonal matrices, and set all diagonal entries to be equal aside from the entries of \mathbf{Q} corresponding to the lift and drag states, which we decrease by a factor of 10 to avoid excessive oscillations in the estimated force coefficients. We find that Kalman filter performance is relatively insensitive to changes in these weights.

DISTRIBUTION A: Distribution approved for public release.

Chapter 4

Lift enhancement of high angle of attack airfoils using periodic pitching

In this work, we study a sinusoidally pitching, two-dimensional flat plate airfoil at a Reynolds number of 100, across a range of pitching amplitudes, frequencies, mean angles of attack, and pitch axis locations. We report on the lift, drag, and wake structures present in different regions of parameter space. We examine the average and spectral properties of the forces on the airfoil, and use dynamic mode decomposition to examine the structures and frequency content of the wake. We give focus to a number of regions in parameter space where interesting behavior is observed. In particular, we find that in the regime where the flow on the upper surface of the airfoil is separated, but the steady wake is stable, pitching at a specific frequency excites a vortex shedding mode in the wake, leading to substantial increase in the lift and drag forces. This phenomena is insensitive to pitch-axis location and amplitude. At higher angles of attack where the wake for a steady airfoil exhibits periodic vortex shedding, we find that, in addition to this mean lift maxima, the interaction between the natural and forced modes gives rise to more complex behavior.

4.1 Introduction

The unsteady motion of airfoils at low Reynolds number and high angle of attack leads to a range of phenomena that cannot adequately be explained by classical aerodynamic theories. It is precisely these conditions that are encountered by small fliers, ranging from biological examples such as birds[153], insects[18, 120, 156], and bats, or manmade UAVs and MAVs. The vortex dynamics excited by airfoil motion, actuation, or indeed present in the natural flow at sufficiently high angles of attack, can significantly affect aerodynamic performance[87]. This motivates work that seeks to understand and control such phenomena, and indeed modeling the dynamics of pitching and plunging airfoils has attracted significant recent attention[22, 23, 10, 57, 61, 39, 168].

This work will investigate the interaction between periodic vortex shedding that can occur for bluff bodies (or airfoils at sufficiently large angle of attack), and imposed sinusoidal pitching motion. In the case of plunging motion, it has been observed that lock on[121] can occur between plunging frequency and natural vortex shedding[167, 31, 33], while similar phenomena have been found for surging oscillations over a wide range of Reynolds number[29]. We will show that similar phenomena are observed in the case of pitching motion. In experimental conditions, plunging oscillations may also lead to a bifurcation of the wake direction[32].

It has been observed that optimal pitching trajectories maximize the circulation that is entrained in leading edge vortices[90], linking the concepts explored here to the general notion of a formation

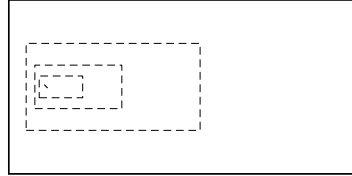


Figure 4.1: Computational domain used for this study, with the size and location of the airfoil shown. Dashed lines represent the borders of each nested grid.

number that can be used to explain characteristic sizes and frequencies associated with vortex phenomena[51].

While this work will only consider two-dimensional airfoils, we note that three dimensional phenomena can give rise to additional complexity. For example, aspect ratio effects being significant on lift enhancement due to periodic forcing[140], and in the case of three dimensional airfoils that are free to exhibit rolling motion, forced pitching can lead to self-excited roll oscillations[144].

There are strong parallels between studying the effect on lift and drag in the context of lifting airfoils, and in the investigation of thrust-generating airfoils[42], where it is found that propulsive efficiency is maximized when flapping produces a reverse von-Kármán wake that excites the least stable spatial mode of the mean wake flow[146, 145]. We describe the numerical method and scope of the work in section 4.2, before presenting our results in section 5.4. We will focus on presenting and analyzing results at parameters where the pitching motion triggers, strengthens, and interferes with vortex shedding.

4.2 Numerical method and scope of investigation

We use an immersed boundary projection method[139, 34] to perform direct numerical simulations of the incompressible Navier–Stokes equations. The domain consists of four nested grids about a flat plate airfoil. A diagram of the computational domain is shown in Figure 5.1. Each of the four grids contains 600 by 300 grid points, with a total computational domain extending 96 and 48 chord lengths in the streamwise and transverse directions, respectively. The Reynolds number (based on chord length and freestream velocity) is fixed at 100 throughout. The relative computational cheapness of such two-dimensional, low Reynolds number configurations makes thorough investigations of high-dimensional parameter spaces feasible. Resolution studies were performed to ensure that the resolution and extent of the domain were sufficient. To give an example of this, we show in Figure ?? results from applying Crank-Nicholson and third-order Runge-Kutta time steppers were used to evolve the linear and nonlinear terms respectively, with step size ranging between $\Delta t = 0.0005c/U$ and $\Delta t = 0.01c/U$, with the smaller range of Δt required to resolve pitching motions with larger frequencies and/or amplitudes. In all cases, we run the simulations for sufficiently long such that any limit cycle or long-time behavior is reached before the data that is used for analysis is collected. We consider airfoil kinematics of the form

$$\alpha(t) = \alpha_M + \alpha_A \sin(2\pi f^* t), \quad (4.2.1)$$

DISTRIBUTION A: Distribution approved for public release.

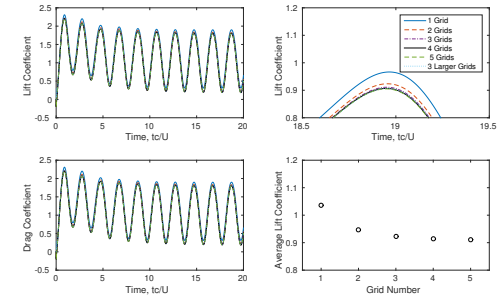


Figure 4.2: Resolution study to determine appropriate size of computational domain

where $f^* = fc/U$ is a dimensionless frequency. We perform simulations with the mean angle of attack varying in 5° increments between 15° and 45° , with pitching amplitudes of 1° , 2° , 5° and 10° . We consider frequencies in the range $f^* \in [0.01, 5]$, with approximately 20 frequencies used for each α_M and α_A . For some cases, additional frequencies are added to improve local resolution in parameter space. Performing these simulations with for pitching about the leading edge and midchord, this results in a total of approximately 1120 individual simulations.

4.3 Results

4.3.1 Static data

To give a sense for the behavior of the stationary airfoil, we show a typical lift curve in Figure 4.3. We observe the expected linear relationship between the angle of attack, α , and the lift coefficient, C_L for low angles of attack. Once the angle of attack becomes sufficiently large ($\alpha > 10^\circ$), flow separation on the upper surface of the airfoil leads to a shallow lift slope. At $\alpha \approx 20^\circ$, the flow is separated and steady. Beyond a critical angle of attack $\alpha_c \approx 27^\circ$, the steady solution becomes unstable, and periodic vortex shedding is observed. This is an example of a supercritical Hopf bifurcation that is seen in the wake of bluff bodies as the Reynolds number is increased[135]. Note that in the case of an airfoil at an angle of attack, the projected area $c \sin(\alpha)$ is the effective length parameter for determining the location of the bifurcation. For $\alpha > \alpha_c$, the system exhibits higher lift (and drag) than would occur at the unstable equilibrium solution.

4.3.2 Force analysis

In this section, we study the lift and drag forces for pitching motion with various amplitudes, frequencies, and mean angles of attack.

DISTRIBUTION A: Distribution approved for public release.

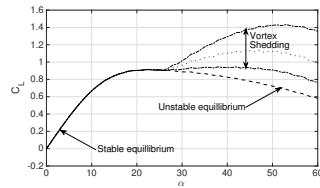


Figure 4.3: Lift curve for stationary airfoil, showing regions where the equilibrium is stable ($\alpha < 27^\circ$) and unstable ($\alpha > 27^\circ$), above which periodic vortex shedding occurs.

Figure 4.4 shows the mean lift coefficient as a function of the dimensionless frequency, f^* , for pitching with a range of amplitudes, α_A , and mean angles of attack, α_M . We observe a distinct local peak in C_L for all values of α_M and α_A , aside from pitching with low amplitudes ($\alpha_A = 1^\circ$ or 2°) about $\alpha_M = 15^\circ$. The location of this lift peak moves slightly as α_M varies, from approximately $f^* = 0.3$ at $\alpha_M = 20^\circ$, to $f^* = 0.23$ at $\alpha_M = 45^\circ$. For $\alpha_M \geq 30^\circ$, we observe a second peak emerging at approximately twice the frequency of the dominant peak. This suggests that we excite dynamics that give enhanced lift when pitching at both a fundamental frequency and its first harmonic. We note also that the size of the lift increment seems to be largest for the intermediate base angles of 25° and 30° .

Figure 4.5 shows the mean drag coefficient for the same range of parameters as Figure 4.4. We find that there are increases in drag that show similar behavior to those for the lift. To compare the changes in lift and drag more explicitly, we plot the ratio between mean lift and drag coefficients in Figure 4.6. For larger pitching amplitudes, there is an increase in the lift-to-drag ratio at certain frequencies. The frequency of the lift-to-drag peak shows similar behavior to the peaks in both lift and drag (note that, unlike the lift and drag forces, lift over drag decreases with increasing α_M). This finding is potentially important for the effectiveness of such motions in flight.

Turning our attention back to the lift coefficient, we plot in Figure 4.7 the increase in lift coefficient from the fixed-wing value at α_M , normalized by the amplitude of pitching. For angles of attack below the critical angle (α_c) at which vortex shedding occurs, the lift increment is slightly larger for larger α_A , even after normalizing, despite the fact that the mean lift is lower than the fixed-wing value across other frequencies. This could be due to the fact that, for larger α_A , the maximum angle of attack attained in a pitching cycle is closer to or exceeds α_c , and thus better able to excite vortex shedding. Conversely, for $\alpha_M \geq 25^\circ$, the normalized lift increment is slightly larger for smaller pitching amplitudes, though in some cases this is in line with the larger average lift increments present for lower pitching amplitudes across all frequencies.

To analyze the effect of pitch axis location, we show in Figure 4.8 the normalized lift increment (i.e., the same quantity plotted in Figure 4.7) for pitching about the leading edge, rather than the midchord. We find very similar results to pitching about the midchord, with maximum increased lift at dimensionless frequencies between 0.25 and 0.3. The lift increment is larger for pitching about the leading edge, which could be due to the increased range of motion of the trailing edge

DISTRIBUTION A: Distribution approved for public release.

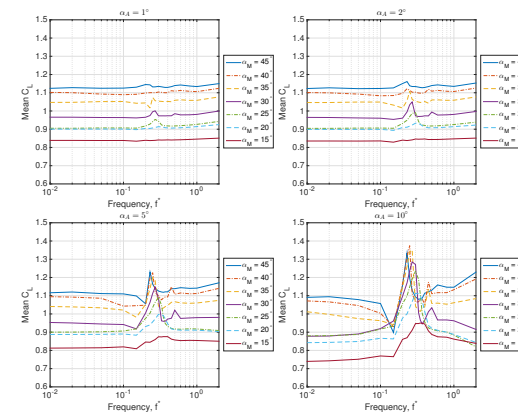


Figure 4.4: Mean lift coefficient for a range of pitching amplitudes α_A , frequencies, f^* , and mean angles of attack, α_M . Pitching is about the midchord.

for the same angular pitch amplitude. Note also that leading edge pitching will result in larger added mass forces, which for nonzero α_M will increase lift and decrease drag, particularly for high pitching frequencies. The remainder of this section will consider pitching about the midchord. The effect of pitch axis location will be investigated more thoroughly in the next section.

Figure 4.9 indicates how the mean lift compares to the maximum and minimum lift for $\alpha_A = 5^\circ$. Note that in some of the cases the lift is not periodic with the period of forcing, so these maximum and minimum values are the global extrema over many cycles. We observe (particularly clearly for lower mean angles of attack) that as the frequency increases from low values, the amplitude of the lift response increases, while the mean remains approximately constant. Above $f^* \approx 0.2$, the amplitude of the variation in lift decreases, but with the lift minimum rising more abruptly than the lift maximum falls. This asymmetry produces the higher average lift that is observed in the range $0.1 < f^* < 0.5$. For higher frequencies, larger added mass forces mean that the amplitude of the lift oscillations continue to increase, though the mean lift stays approximately constant.

To analyze the time-varying behavior in more detail, we take the discrete Fourier transform of the lift coefficient signal in time for each trial. The results for this are shown in Figure 4.10, for pitching amplitude $\alpha_A = 1^\circ$. For $\alpha_M \leq 25^\circ$, we observe one dominant frequency peak, corresponding to the pitching frequency f^* . Even though the undisturbed wake is stable at $\alpha = 25^\circ$, we still observe some frequency content near the almost-unstable vortex shedding mode across all pitching frequencies. For larger angles of attack, there is a second major peak in the spectra, corresponding to the vortex shedding frequency at the given α_M . In the region where these two frequencies

DISTRIBUTION A: Distribution approved for public release.

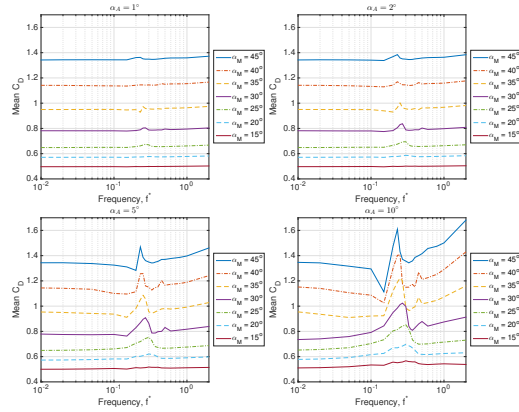


Figure 4.5: Mean drag coefficient for a range of pitching amplitudes α_A , frequencies, f^* , and mean angles of attack, α_M . Pitching is about the midchord.

are similar, there appear to be complex interactions between the dynamics associated with each frequency. As α_M grows larger, a distinct peak emerges at the first harmonic of the fundamental vortex shedding frequency, further complicating the frequency response of the system, which can now include, at very least, sums and differences of multiples of these frequencies.

4.3.3 Wake analysis with dynamic mode decomposition

Here we analyze the flow field in the wake of the body, in an attempt to study the underlying physics behind the phenomena observed in section 4.3.2. We will make use of the dynamic mode decomposition (DMD)[125, 126] which is a technique that can extract dynamical content from data, in the form of spatial modes and their associated growth/decay rates and frequencies of oscillation. We refer the reader to recent references for details of the DMD algorithm[126, 119, 149, 160] and its variants[27, 164, 71, 62, 63, 40].

We begin by considering a base angle $\alpha_M = 20^\circ$, which is prior to the Hopf bifurcation at which unforced vortex shedding occurs, and thus has a stable equilibrium wake. Figure 4.11 shows vorticity field snapshots for a variety of forcing frequencies with amplitude $\alpha_A = 1^\circ$. We observe that at around $f^* \approx 0.3$, the vorticity field is qualitatively different, with periodic vortex shedding being excited by the pitching motion. This immediately suggests that the increased lift observed at these pitching frequencies arises due to enhanced vortex formation. We note that the vorticity fields for pitching about the leading edge (left) and midchord (right) show similar results, with leading-edge pitching generally leading to stronger, more distinct vortices forming closer to the airfoil.

DISTRIBUTION A: Distribution approved for public release.

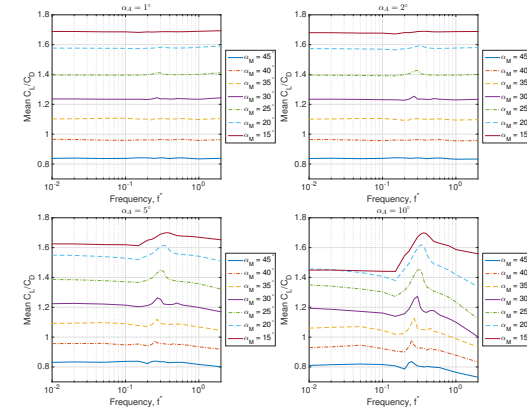


Figure 4.6: Mean of lift-to-drag ratio for a range of pitching amplitudes α_A , frequencies, f^* , and mean angles of attack, α_M . Pitching is about the midchord.

The vorticity fields shown in Figure 4.12 have the same parameters as those for Figure 4.11, but with a larger pitching amplitude of $\alpha_A = 5^\circ$. We again see the same phenomena where the forcing excites vortex shedding, but here distinct vortices form and persist downstream over a wider range of frequencies. This is consistent with the results from section 4.3.2, where for the $\alpha_M = 20^\circ$ case in Figures 4.4 we observe an enhanced lift over a wider range of frequencies for higher forcing amplitudes.

To investigate further the dynamics of the wakes, we perform DMD on the vorticity field. We use 191 snapshots for each case, with a time gap between snapshots of $\Delta t = 0.1c/U$. We take data from a region downstream of the body as our domain for DMD, to avoid complications associated with having the moving body in the domain. For clarity of results, we truncate the rank of our data to 20 proper orthogonal decomposition (POD)[66] modes. This is found to capture at least 99% of the energy of the flow.

While it is most often applied to data from systems without external forcing, DMD can be used to examine forced systems[147, 105, 92], though one must take care in the interpretation of its outputs. In this context, we show that it can be an effective tool to determine both the frequency content of the wake, and also if the wake “locks on” to a vortex shedding mode. As an aside, we note that more rigorous connections between DMD and Fourier analysis can be made[27].

Figure 4.13 shows the DMD eigenvalues, as well as the four largest amplitude modes, for a variety of forcing frequencies, for pitching about the leading edge (left) midchord (right) with amplitude $\alpha_A = 1^\circ$. In this section, we restrict our attention to frequencies near the vortex shedding frequency and frequency of maximum lift. Results at lower and higher frequencies are similar to the minimum

DISTRIBUTION A: Distribution approved for public release.

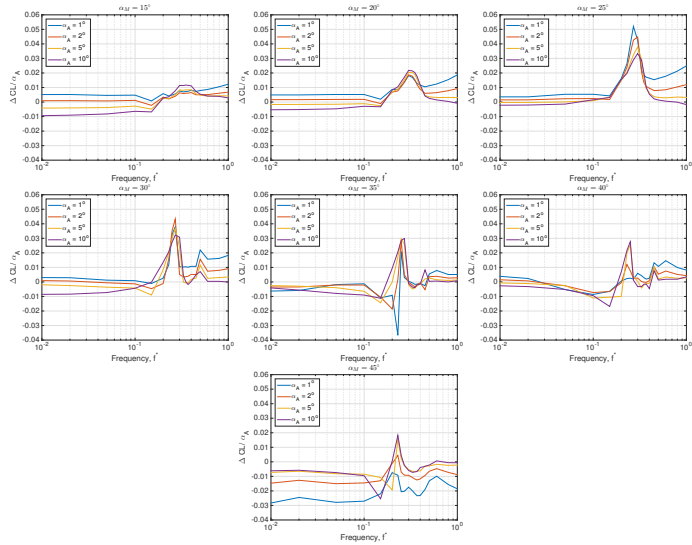


Figure 4.7: Mean lift coefficient increment over the fixed airfoil value, normalized by the amplitude of pitching α_A , across a range of pitching amplitudes α_A , frequencies, f^* , and mean angles of attack, α_M . Pitching is about the midchord.

DISTRIBUTION A: Distribution approved for public release.

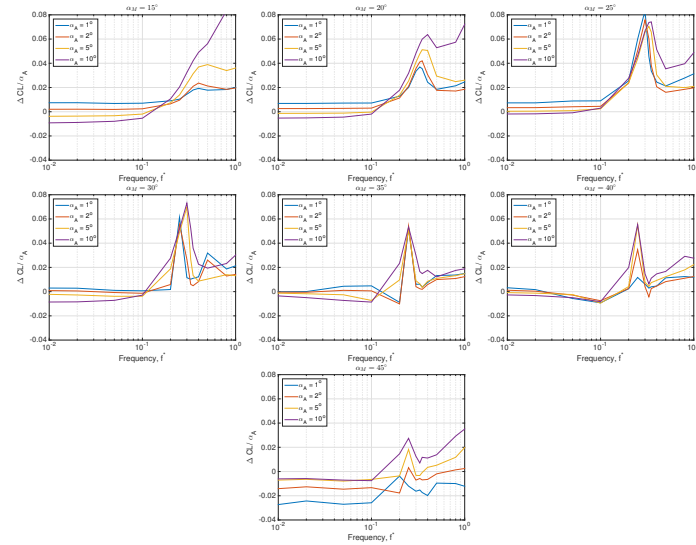


Figure 4.8: Mean lift coefficient increment over the fixed airfoil value, normalized by the amplitude of pitching α_A , across a range of pitching amplitudes α_A , frequencies, f^* , and mean angles of attack, α_M . Pitching is about the leading edge.

DISTRIBUTION A: Distribution approved for public release.

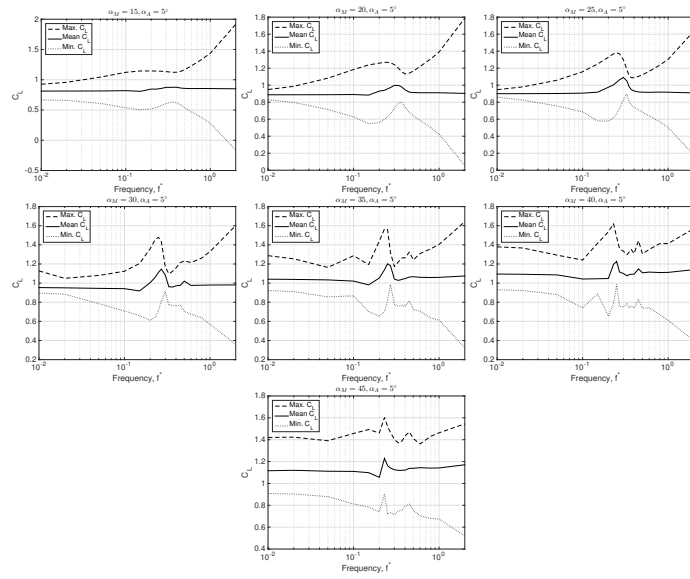


Figure 4.9: A comparison between the maximum, minimum, and mean lift coefficient attained for pitching with amplitude $\alpha_A = 5^\circ$, for a range of mean angles of attack, α_M , and frequencies, f^* . Pitching is about the midchord.

DISTRIBUTION A: Distribution approved for public release.

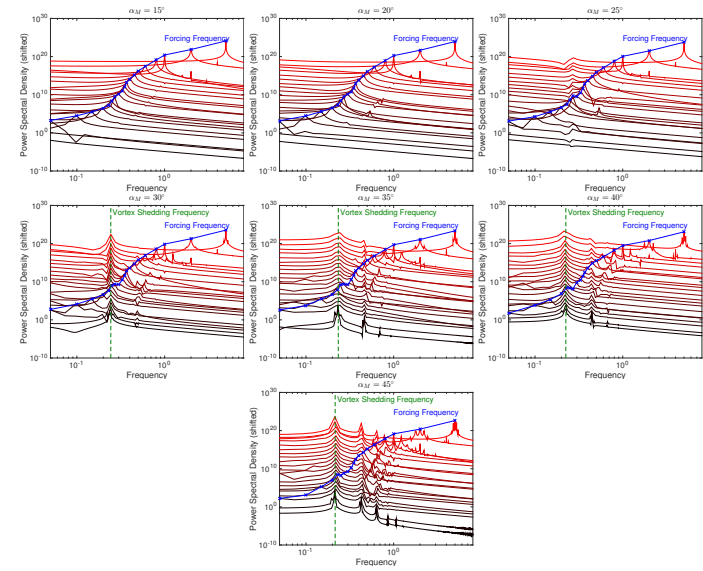


Figure 4.10: Power spectral densities of the lift force for pitching motion about the midchord with amplitude $\alpha_A = 1^\circ$. For clarity, the spectra for each forcing frequency is shifted by one order of magnitude, so the absolute scale of the vertical axis is not significant.

DISTRIBUTION A: Distribution approved for public release.

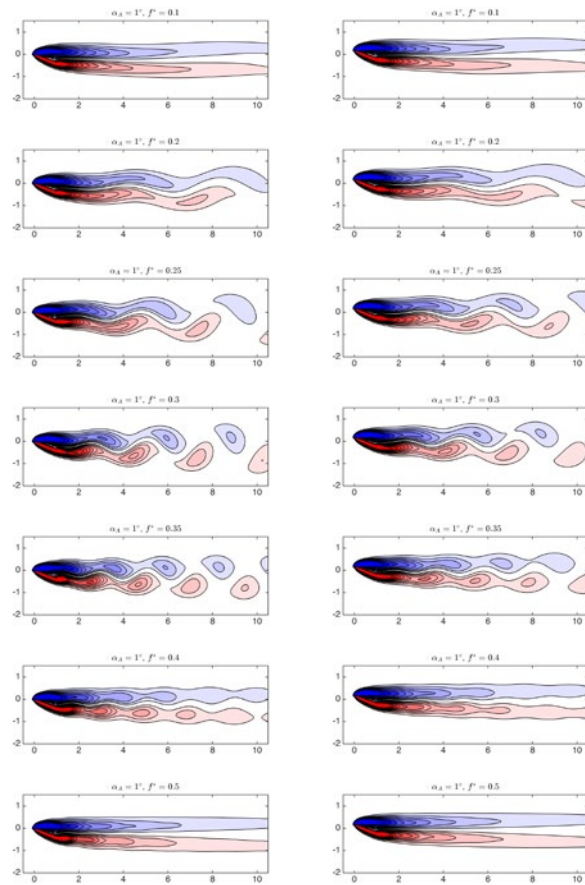


Figure 4.11: Instantaneous vorticity fields for pitching about the leading edge (left) and midchord (right) at a variety of frequencies, with $\alpha_M = 20^\circ$ and $\alpha_A = 1^\circ$.

DISTRIBUTION A: Distribution approved for public release.

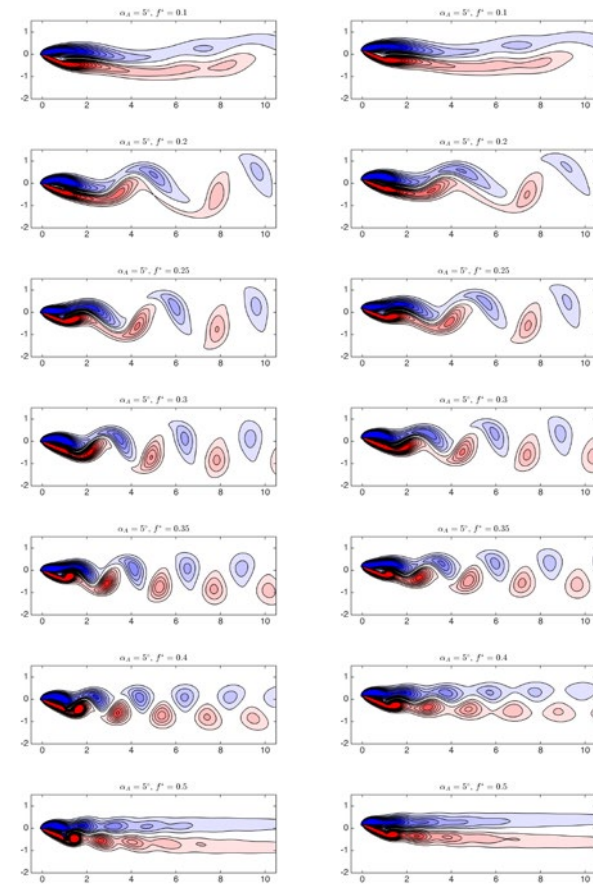


Figure 4.12: Instantaneous vorticity fields for pitching about the leading edge (left) and midchord (right) at a variety of frequencies, with $\alpha_M = 20^\circ$ and $\alpha_A = 1^\circ$.

DISTRIBUTION A: Distribution approved for public release.

and maximum frequencies considered here. Note that the real and imaginary components of the eigenvalues (in continuous time) indicate the growth rate and frequency of the associated DMD modes.

For this mean angle of attack ($\alpha_M = 20^\circ$), the maximum increase in lift occurs at $f^* = 0.3$. At this frequency, the DMD eigenvalues are at the frequency of pitching and its harmonics. Since vortex shedding is clearly observed in Figure 4.11, this suggests that it is locking onto the forcing frequency. For the surrounding frequencies ($f^* = 0.25$ and 0.35), we observe that the eigenvalues are scattered across a range of frequencies. This suggests that vortex shedding is not fully locking on to the forcing frequency, and that there is a broad range of frequency content present. We also find that the second, third and fourth DMD modes all have similar spatial wavelength, again indicating that certain features persist across a range of frequencies. Note that, unlike POD modes, DMD modes are not required to be orthogonal, and thus there can exist multiple DMD modes that are similar to each other, having slightly different frequencies of oscillation.

If we move further away from $f^* = 0.3$, we find that the DMD modes again lie on harmonics of the forcing frequency. In these cases (i.e., for $f^* = 0.2$ and 0.4 plotted here, and for other cases not shown), it appears that the least stable mode in the wake is not being excited, as we are not close enough in frequency to do so. This also explains why there is no significant lift increase at these frequencies. The similarity between pitching at the leading edge and midchord suggests that these observations are not particularly sensitive to pitch-axis location.

Figure 4.14 shows plots of the same quantities and parameters as Figure 4.13, but for pitching with amplitude $\alpha_A = 5^\circ$. Broadly speaking, the results are similar, with DMD eigenvalues lying on the imaginary axis at multiples of the forcing frequency for $f^* = 0.2, 0.3$ and 0.4 , and located in a significantly more scattered arrangement with numerous modes of similar frequency content and spatial structure for $f^* = 0.25$ and 0.35 . We find that the oscillating modes have higher amplitude in this case, with the “lock-on” mode having higher amplitude than the mean mode for leading edge pitching at $f^* = 0.3$. We further note that, unlike the case for $\alpha_A = 1^\circ$, the mean flow (i.e., the DMD mode with a corresponding eigenvalue close to 0) looks substantially different between low frequency oscillation, where the wake seems to spread out substantially a short distance downstream of the airfoil, and high frequency oscillation, where the wake appears to be narrower with regions of high vorticity persisting far downstream. Referring back to Figure 4.12, the enhanced spreading of the mean flow is seemingly due to the larger vortices drifting above (for negative vorticity) and below (positive vorticity) the airfoil as they are shed. This phenomenon could also explain why the lift-to-drag ratio is often maximized at pitching frequencies slightly larger than those at which maximum lift occurs. The enhanced spreading at lower frequencies increases drag, so lift-to-drag benefits exist only at higher frequencies, where the wake remains thinner.

Thus far, we have only analyzed the wake for a case where the base flow is stable. We now turn our attention to the case, $\alpha_M = 30^\circ$, where the flow exhibits a vortex shedding limit cycle. Figure 4.15 shows vorticity field snapshots, as well as DMD eigenvalues and modes (only showing the four highest amplitude modes) for pitching about a mean angle $\alpha_M = 30^\circ$ with amplitude $\alpha_A = 1^\circ$, for a variety of pitching frequencies. The wakes for $f^* = 0.2, 0.3, 0.35$ and 0.4 all look very similar, with high amplitude DMD eigenvalues at the natural vortex shedding frequency, and lower amplitude eigenvalues at the pitching frequency. This is consistent with Figure 4.10, where the subplot for $\alpha_M = 30^\circ$ shows a larger peak at the vortex shedding frequency, and a lower peak at the forcing frequency. For $f^* = 0.25$, the forcing and vortex shedding frequencies are almost identical, which appears to give stronger vortex formation, and in turn the increase in lift seen in Figure 4.4.

DISTRIBUTION A: Distribution approved for public release.

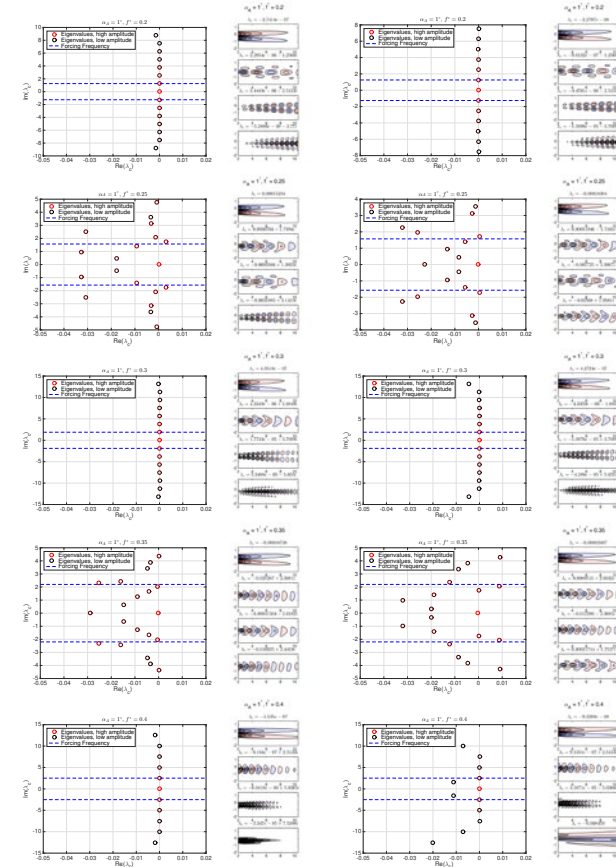


Figure 4.13: DMD eigenvalues, and the real components of the 4 largest amplitude modes (ordered by amplitude), for pitching about the leading edge (left), and midchord (right) at a variety of frequencies, with amplitude $\alpha_A = 1^\circ$, and mean angle of attack $\alpha_M = 20^\circ$. Eigenvalues that are colored red correspond to modes with larger amplitudes.

DISTRIBUTION A: Distribution approved for public release.

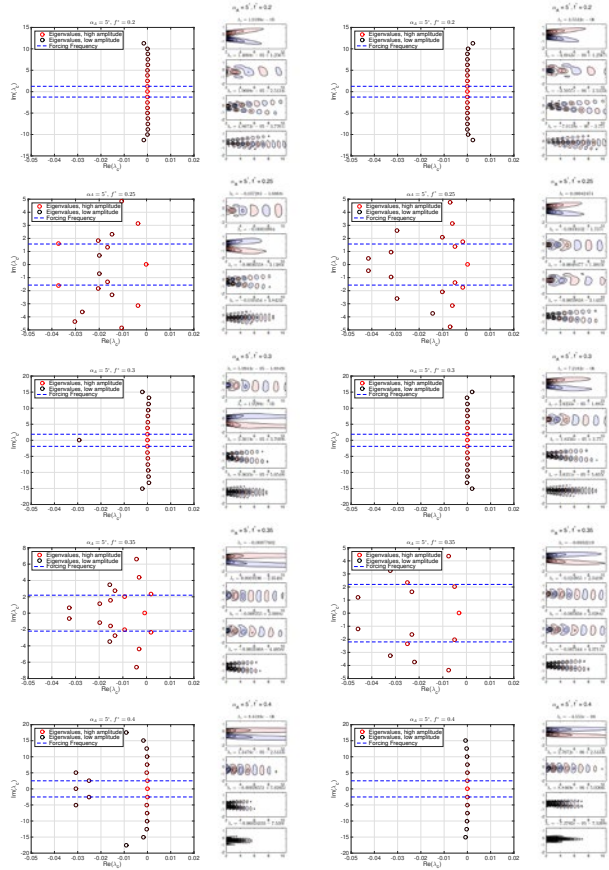


Figure 4.14: DMD eigenvalues, and the real components of the 4 largest amplitude modes (ordered by amplitude), for pitching about the leading edge (left), and midchord (right) at a variety of frequencies, with amplitude $\alpha_A = 5^\circ$, and mean angle of attack $\alpha_M = 20^\circ$. Eigenvalues that are colored red correspond to modes with larger amplitudes.

DISTRIBUTION A: Distribution approved for public release.

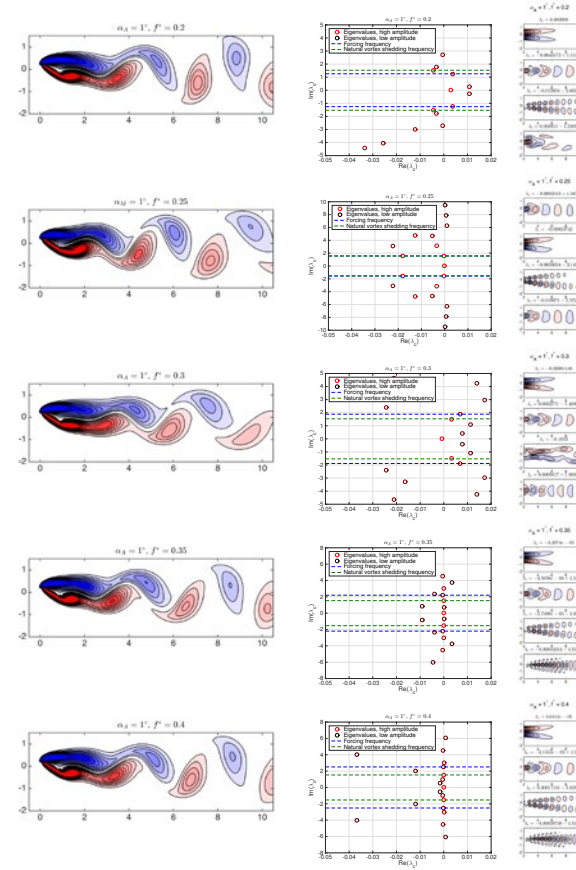


Figure 4.15: Wake snapshots, DMD eigenvalues, and the real components of the 4 largest amplitude modes (ordered by amplitude), for midchord pitching at a variety of frequencies, with amplitude $\alpha_A = 1^\circ$, and mean angle of attack $\alpha_M = 30^\circ$. Eigenvalues that are colored red correspond to modes with larger amplitudes.

DISTRIBUTION A: Distribution approved for public release.

4.4 Discussion and conclusions

For angles of attack below the critical angle where unforced vortex shedding first occurs (α_c), it was found that pitching at a certain frequency can excite vortex shedding in the wake, leading to higher mean lift. The magnitude and width in frequency range of the lift increment increases significantly as the forcing amplitude increases. This is perhaps a similar phenomenon to the widening of the “resonance horn” [20] observed by Choi et al. [29] for the case of a surging and plunging airfoil (though in that case, the system was above the critical bifurcation parameter). Note, however, that comparing Figures 4.4 and 4.14 indicates that there can be a significant increase in lift even without frequency lock-on.

For α_M above the critical angle for vortex shedding, there is a similar peak in the mean lift coefficient when the pitching frequency is close to the natural vortex shedding frequency or its first harmonic. When the natural and forcing frequencies are different, the interactions between the two frequencies can lead to complex frequency spectra in the forces and wakes. Note in particular that pitching some amount below the vortex shedding frequency can lead to a notable decrease in mean lift for $\alpha_A \geq 5^\circ$ at $\alpha_M \geq 35^\circ$.

While periodic pitching at the preferred frequency where vortex shedding is excited or enhanced also leads to an increase in drag, the differences in effect that pitching has on the two force components leads to an increase in the lift-to-drag ratio for frequencies slightly above the frequency for which the lift is maximized. It is interesting to note that while the frequency at which the maximum lift increment occurs decreases slightly as α_M increases (in agreement with the slight decrease in natural vortex shedding frequency), the frequency giving maximum lift-to-drag ratio increases with α_M . Indeed, for high α_M it seems that the maximum lift-to-drag ratio typically occurs between the peaks in lift and drag located at the vortex shedding frequency and its first harmonic, where there is a local lift minimum, and thus also a slightly more substantial drag minimum.

Beyond α_c , the interactions between the pitching and vortex shedding frequencies can lead to complex frequency spectra in both the forces (as seen in Figure 4.10) and wakes (Figures 4.13-4.15). There are numerous methods by which one can analyze frequency content, and here we show how DMD can clearly distinguish between cases where all frequencies present are harmonics of the pitching frequency, and where there is a broad range of frequency content.

There has been much effort in the past to understand, model, and predict unsteady aerodynamic forces, moments, pressures, and indeed many other quantities of interest for moving airfoils. Particularly in the case of separated flow, these dynamics are often highly nonlinear. One might seek to get around this by linearizing about a certain fixed point (say an angle of attack), in the hope that a linear model would at least be locally accurate. The findings presented here suggest that such an approach might be problematic, since a linear model (e.g., a transfer function) can only predict the magnitude and phase of a response to sinusoidal forcing, but not any change in the mean value. Thus, such effects must be accounted for separately, or a more complex modeling framework used.

Further work in this investigation will compare the findings to the results of stability analyses of the stable and unstable equilibrium wakes, and the mean of the vortex shedding wake, and will use wind tunnel experiments to investigate whether the phenomena observed persist for higher Reynolds numbers.

Chapter 5

Nonlinear reduced-order models of fluids systems using extended dynamic mode decomposition

Data-driven approximations to the Koopman operator have much potential for capturing and illuminating the dynamics exhibited by the Navier-Stokes equations. In this work, we show that the elements of an identified finite dimensional approximation to the Koopman operator can be utilized for the construction of accurate nonlinear reduced-order models. We present a modification to the extended dynamic mode decomposition algorithm through the inclusion of a regularization parameter, which we find often gives more accurate models. The performance of models identified using our proposed method are compared to those found by performing a Galerkin projection of the governing equations onto proper orthogonal decomposition modes, for the canonical case of two-dimensional flow past a circular cylinder. We demonstrate that identifying nonlinear models using EDMD is particularly advantageous when the data available is noisy, or is only available within certain regions of space or time.

5.1 Introduction

A much-desired goal in fluid mechanics, and indeed many other fields, is to obtain simple models that are capable of predicting the behavior of seemingly complex systems. Low-dimensional models can not only improve our fundamental understanding of such systems, but are often required for purpose of efficient and accurate prediction, estimation and control. Broadly speaking, one can obtain low-dimensional information about a system (whether it be in the form of a reduced-order model, or simply spatial modes corresponding to certain energetic or dynamic characteristics) in numerous ways, potentially using some combination of data collected from simulations and experiments, and theoretical knowledge of the system, such as the governing partial differential equations (PDEs).

Purely data-driven methods can include those developed particularly for fluids applications, such as the dynamic mode decomposition (DMD) [125, 126], or those which are appropriated from other communities, such as the eigensystem realization algorithm (ERA) [82, 72], which was first applied to study spacecraft structures, but has more recently been appropriated to model a wide range of fluids systems [25, 2, 68, 69, 22, 23, 15, 67, 49]. DMD has been used to study a wide range of problems arising in fluid mechanics (e.g., [119, 128, 127, 100, 129, 43, 58, 70, 83, 93, 55, 123, 45]), with many subsequent variants further increasing its range of utility and applications [27, 164, 149,

71, 62, 63, 40, 106, 124, 98, 122]. One limitation of the methods mentioned so far is that (when considered in the context of data-driven reduced-order modeling techniques) they are linear, in the sense that the reduced order model that is identified is in the form of a linear system of ordinary differential equations (ODEs).

While there have been a number of examples of nonlinear data-driven modeling techniques used in fluids applications [85, 102, 104, 52, 11, 37, 77, 60, 39, 24], their widespread use has been more limited, and the underlying theory is less established, than linear techniques. More details concerning the application of data-driven modeling techniques in fluid mechanics can be found in recent review articles [21, 113].

Perhaps the most common method to obtain a nonlinear reduced order model for fluids systems comes via a projection of the governing equations onto a low-dimensional basis that is optimal for capturing the energy of the data, i.e., the proper orthogonal decomposition (POD) [86, 17, 66], a procedure referred to as Galerkin projection. Galerkin projection (GP) has been used to extract models for many different fluids systems, a non-exhaustive list includes flow past a cylinder at low Reynolds number [41, 96, 95], grooved channels [41] the wall region of turbulent boundary layers [6, 103], flat plate boundary layers [111], turbulent plane Couette flow [91, 134], turbulent pipe flow [19] cavity oscillations [116, 115], mixing layers [110, 150, 13], and compressible flows [118]. One significant drawback of GP models is that they ignore modes that are low in energy, but are required for the dissipation of energy in the full system. A number of modifications have been proposed to address this concern, as well as other issues with such models. Refs. [6] and [103] use an eddy viscosity term that accounts for energy dissipated into unmodeled modes, [99] investigates a hierarchy of eddy viscosity formulations, while [157, 158] incorporate LES closure modeling strategies. Refs. [35] and [36] summarize a number of calibration techniques that can be used to improve the accuracy of Galerkin models, and also discuss the various ways in which the error of such models can be quantified. Ref. [12] employs a subspace rotation technique to stabilize the models, which, unlike other calibration techniques, maintains consistency with the original governing equations. Ref. [13] imposes constraints to balance the turbulent kinetic energy of the resulting model. All of these modifications of Galerkin projection increase the “data-driven” nature of the method. Ref. [97] gives an in-depth summary and analysis of many issues, variations, progress, and open problems on the topic of Galerkin projection models, while [84] gives a clear expository introduction of the main ideas in Galerkin projection, with examples.

While we mentioned above that DMD could be classified as a “linear” method, connections between the DMD algorithm and the Koopman operator [119, 89] give promise that it can ultimately be used to model and understand nonlinearities. In this work, we will propose a method for obtaining nonlinear reduced order models that is based upon a recently-developed extension of DMD [160], referred to as extended DMD (EDMD), in which nonlinearities can be accounted for by an appropriate choice of observables. In particular, we will explore how this algorithm can be tailored to identify nonlinear models that have the same (or similar) form as those that would be obtained through projection of the governing equations onto a low-dimensional basis obtained from data. In this sense, the nonlinear models that we identify in this work will come from EDMD, but will have similar form to those given by GP. We note that this is a different approach to using dominant DMD modes as an alternative to POD modes for a basis for projection [143]. A further recently-proposed approach uses DMD to efficiently approximate just the nonlinear component of the dynamics [5], as an alternative to the discrete empirical interpolation method [14, 26].

We lastly note that several previous works consider this dichotomy between using projection onto governing equations, or using time-resolved data, to identify models, most often for linear systems. For example, [69] considers models identified directly using ERA and models identified by considering each of the pertinent physical processes individually, while [64] discusses the use of

DISTRIBUTION A: Distribution approved for public release.

both GP models and ARMAX system identification methods with physically motivated terms to model (and subsequently control) flow over a backwards-facing step.

The structure of this work is as follows. Sect. 5.2 introduces POD and Galerkin projection. Aside from GP being used for the purposes of comparison to EDMD models, the POD section will also be important for the purposes of defining observables for EDMD. Sect. 5.3 describes DMD and EDMD, and introduces the particular form of the EDMD, as well as a regularized variant thereof, that will be utilized for system identification purposes. Models will be identified and tested in Sect. 5.4 on data obtained from numerical simulations of flow past a circular cylinder, the results of which are discussed in further detail in Sect. 5.5.

5.2 Proper orthogonal decomposition and Galerkin projection

While the main focus of this work concerns reduced-order models obtained from EDMD algorithms, GP models will serve as both a basis for comparison of model performance, and to guide our choice of observable functions when using EDMD. With this in mind, in this summary we give a brief summary of POD and Galerkin projection.

5.2.1 Proper orthogonal decomposition

The goal of the proper orthogonal decomposition (POD) is to obtain a set of empirical spatial modes that optimally represent a given dataset from an energetic standpoint. Assume that we can decompose the dynamics of some system $\mathbf{u}(x, t)$ (which could be the time-varying velocity field of a fluid, say) by

$$\mathbf{u}(x, t) = \mathbf{u}_0(x) + \sum_{i=1}^{\infty} \mathbf{u}_i(x) a_i(t), \quad (5.2.1)$$

where $\mathbf{u}_0(x)$ is some fixed (often average) data, and $\{\mathbf{u}_i(x)\}_{i=1}^{\infty}$ are a set of orthonormal basis functions (modes). POD takes these modes to be those which successively capture the most energy of the velocity field. Each POD mode \mathbf{u}_i satisfies the integral

$$\int_{\Omega} R_{i,j}(x, x') \mathbf{u}_i(x') dx' = \lambda \mathbf{u}_i(x),$$

where $R_{i,j}(x, y) = E[\mathbf{u}_i(x) \mathbf{u}_j(y)]$, with E being the expectation. As indicated by Eq. (5.2.1), POD is normally performed after first subtracting the mean (or perhaps an equilibrium point) from the data. This approach has the advantage that \mathbf{u}_0 satisfies the required non-homogeneous boundary conditions, meaning that all other modes \mathbf{u}_i will satisfy homogenous boundary conditions, so any linear combination of modes of the form given by Equation (5.2.1) will automatically satisfy the correct boundary conditions of the problem at hand. In discrete terms, if we arrange finite-dimensional data collected from a simulation or experiment into a matrix \mathbf{Y} , with each column representing a snapshot of data at a given time, then the POD modes are the columns of \mathbf{U} in the singular value decomposition $\mathbf{Y} = \mathbf{U}\mathbf{\Sigma}\mathbf{V}^*$. Here the i^{th} entry of the diagonal matrix $\mathbf{\Sigma}$ corresponds to the energy contained in the i^{th} POD mode. In this discrete formulation, for simplicity we are omitting any rescaling of the data that should be performed so that the modes are orthonormal with respect to the usual inner product. That is, if \mathbf{u}_i and \mathbf{u}_j are columns of \mathbf{U} , then we really should have

$$\int_{\Omega} \mathbf{u}_j^*(x') \mathbf{u}_i(x') dx' \approx \sum_{k=1}^n \mathbf{u}_j^*(x_k) \mathbf{u}_i(x_k) dx_k = \delta_{ij},$$

DISTRIBUTION A: Distribution approved for public release.

rather than $\mathbf{u}_i^* \mathbf{u}_i = \delta_{ij}$. The original data \mathbf{Y} can then be represented in terms of POD coefficients by $\tilde{\mathbf{Y}} = \mathbf{U}^* \mathbf{Y}$. If we wish to reduce the dimension of this data, we may do so in an optimal way (with respect to energy content) by simply truncating the columns of \mathbf{U} beyond a certain point, which corresponds to removing POD modes that are of sufficiently low energy. Doing this gives a reduced order approximation of the data $\tilde{\mathbf{Y}}_r = \mathbf{U}_r^* \mathbf{Y}$, where \mathbf{U}_r contains the first r columns of \mathbf{U} . Note that there are alternative truncation techniques that may be more effective than energy maximization for certain applications, for example balanced POD [112] gives a reduced order linear state space model that is optimal with respect to a given set of sensors and actuators.

5.2.2 Galerkin projection

The idea behind GP is to approximate the governing PDEs that describe a given system with a low-dimensional set of ODEs. This is accomplished by projecting the equations onto spatial POD modes identified using the methods described in Sect. 5.2.1. We begin with the incompressible Navier–Stokes equations:

$$\begin{aligned} \frac{\partial \mathbf{u}}{\partial t} &= -(\mathbf{u} \cdot \nabla) \mathbf{u} - \nu \Delta \mathbf{u} - \nabla P \\ \nabla \cdot \mathbf{u} &= 0. \end{aligned} \quad (5.2.2)$$

If we take the (spatial) inner product of Eq. (5.2.2) with a given mode \mathbf{u}_j , we obtain

$$\left\langle \frac{\partial \mathbf{u}}{\partial t}, \mathbf{u}_j \right\rangle = -\langle (\mathbf{u} \cdot \nabla) \mathbf{u}, \mathbf{u}_j \rangle - \nu \langle \Delta \mathbf{u}, \mathbf{u}_j \rangle - \langle \nabla P, \mathbf{u}_j \rangle. \quad (5.2.3)$$

Substituting in the finite-dimensional approximation of Eq. (5.2.1), we obtain

$$\dot{\mathbf{a}} = \mathbf{L} \mathbf{a} + \mathbf{Q}(\mathbf{a}, \mathbf{a}) + \mathbf{f}, \quad (5.2.4)$$

where \mathbf{L} is a linear operation (i.e., a matrix), \mathbf{Q} is a bilinear operator (which can be represented as a 3-tensor), and \mathbf{f} is a vector, each defined based on the identified spatial POD modes by

$$\mathbf{L}_{ij} = -\nu \langle \Delta \mathbf{u}_j, \mathbf{u}_i \rangle, \quad \mathbf{Q}_{ijk} = -\langle (\mathbf{u}_j \cdot \nabla) \mathbf{u}_k, \mathbf{u}_i \rangle, \quad \mathbf{f} = -\langle \nabla p, \mathbf{u}_i \rangle. \quad (5.2.5)$$

This gives a means of approximating the Navier–Stokes equations by a set of nonlinear ODEs. As mentioned in Sect. 6.1, there are many modifications that have been proposed for this general procedure, most typically to account for the energy transfer to unmodeled modes (i.e., the energy cascade to finer spatial scales). For cases where spatial symmetries exist (e.g., in the streamwise and azimuthal directions for circular pipe flow), one can show that the POD modes must become Fourier modes, which can simplify their computation. It is also possible to “factor out” such symmetries by using an optimally chosen moving frame of reference [114, 117].

5.3 Reduced-order models using extended dynamic mode decomposition

This section introduces our proposed modeling approach. Sect. 6.2.1 describes the DMD algorithm, before Sect. 5.3.2 discusses the EDMD extension and how it may be used to obtain nonlinear models. Sect. 5.3.3 gives a regularized modification to EDMD that we find to be advantageous when using EDMD for such purposes. When viewed as a method for reduced-order modeling, the main difference between the approach discussed here and that introduced in Sect. 5.2 is in how the temporal dynamics are identified: GP uses the governing equations, whereas DMD/EDMD uses only data to identify dynamics.

5.3.1 Dynamic Mode Decomposition

Following the notation introduced in [113], suppose we collect pairs of snapshots of data $(\mathbf{y}_i, \mathbf{y}_i^\#)$, which are separated by a fixed time interval Δt . \mathbf{y}_i is often taken to be a velocity field snapshot, but more generally it is a vector consisting of a number of observations/measurements of an evolving dynamical system at a given point in time. We arrange the snapshot pairs as columns of the matrices \mathbf{Y} and $\mathbf{Y}^\#$ (where the data in a given column of $\mathbf{Y}^\#$ was collected Δt after the equivalent column of \mathbf{Y}). Note that if we begin with a sequential time-series of data, then \mathbf{Y} and $\mathbf{Y}^\#$ are simply formed using all of the snapshots excluding the last and first columns, respectively. Let \mathbf{Y} and $\mathbf{Y}^\#$ each be n by m matrices, so we have m pairs of snapshots, each of size n . One can define (see [149]) DMD modes and eigenvalues as the eigendecomposition of the matrix

$$\mathbf{A} = \mathbf{Y}^\# \mathbf{Y}^+, \quad (5.3.1)$$

where \mathbf{Y}^+ is the Moore–Penrose pseudoinverse of a matrix \mathbf{Y} . While useful as a definition, one does not typically compute \mathbf{A} directly, since in the typical case where $n \gg m$, \mathbf{A} is a very large $n \times n$ matrix with rank at most $\min(m, n)$. Thus it is usually beneficial to first project the data onto a lower dimensional subspace, which is often taken from the columns of \mathbf{U} in the singular value decomposition $\mathbf{Y} = \mathbf{U} \mathbf{\Sigma} \mathbf{V}^*$ (possibly truncating columns of \mathbf{U} corresponding to small singular values). From Sect. 5.2.1, this subspace consists of the POD modes of the data. If we let $\tilde{\mathbf{y}} = \mathbf{U}^* \mathbf{y}_k$ be the representation of a given snapshot \mathbf{y} in the POD basis, and let $\tilde{\mathbf{Y}} = \mathbf{U}^* \mathbf{Y}$ and $\tilde{\mathbf{Y}}^\# = \mathbf{U}^* \mathbf{Y}^\#$ following the same notation as introduced in Sect. 5.2.1, then the equivalent of Eq. (6.2.1) in POD space is

$$\tilde{\mathbf{A}} = \tilde{\mathbf{Y}}^\# \tilde{\mathbf{Y}}^+. \quad (5.3.2)$$

A reduced order approximation of the identified dynamics can be obtained by restricting the number of POD modes upon which to project. This is achieved by taking the first r columns of \mathbf{U} , and working in the space of POD coefficients $\mathbf{a}_k = \mathbf{U}_r^* \mathbf{y}_k$. DMD then results in a simple linear dynamical system model of the form

$$\mathbf{a}_{k+1} = \tilde{\mathbf{A}}_r \mathbf{a}_k, \quad (5.3.3)$$

where $\tilde{\mathbf{A}}_r = \mathbf{U}_r^* \mathbf{Y}^\# \mathbf{Y}^+ \mathbf{U}_r$.

5.3.2 Extended dynamic mode decomposition and nonlinear models

A fundamental limitation to models extracted from DMD is their linearity, which can make them entirely unable to model fundamentally nonlinear features that arise in fluid flows. In the context of DMD being an approximation of the Koopman operator, this limitation amounts to Koopman eigenfunctions not lying within the span of the data. Following [160], rather than applying the DMD algorithm directly to the state \mathbf{y} , we may define to define a set of observables $\psi(\mathbf{y})$ (where $\psi: \mathbb{R}^n \rightarrow \mathbb{R}^k$ for some k) that span a space more conducive to approximating the true dynamics. Explicitly, we may proceed with the same DMD procedure described in Sect. 6.2.1, but take the columns of the matrices \mathbf{Y} and $\mathbf{Y}^\#$ to be pairs $(\psi(\mathbf{y}_1), \psi(\mathbf{y}_1^\#))$. The EDMD matrix (which can be viewed as a finite-dimensional approximation to the Koopman operator) is then given by

$$\mathbf{A} = \mathbf{Y}^\# \mathbf{Y}^+ = \left[\psi(\mathbf{y}_1^\#) \ \psi(\mathbf{y}_2^\#) \ \cdots \ \psi(\mathbf{y}_m^\#) \right] \left[\psi(\mathbf{y}_1) \ \psi(\mathbf{y}_2) \ \cdots \ \psi(\mathbf{y}_m) \right]^+. \quad (5.3.4)$$

While $\psi(\mathbf{Y}) = \mathbf{U}_r^* \mathbf{Y}$ gives an optimal transformation of the data from an energetic perspective (and is what Eq. (6.2.2) represents in the EDMD framework), it might not be a suitable transformation for correct identification of the dynamics. To this end, we use the form of Galerkin projection models

to guide an alternative transformation. Expressing the POD coefficients as before by $\mathbf{a} = \mathbf{U}_r^* \mathbf{y}$, we let

$$\mathbf{q} = \psi(\mathbf{y}) = \begin{bmatrix} \mathbf{a} \\ \text{vec}(\mathbf{a} \otimes \mathbf{a}) \end{bmatrix}. \quad (5.3.5)$$

Here $\text{vec}(\mathbf{a} \otimes \mathbf{a})$ denotes a vector of all non-redundant quadratic couplings between POD coefficients, i.e. $(a_1)^2, a_1 a_2, (a_2)^2$, etc. If we keep r POD modes, then we have observables of dimension $k = r + r(r + 1)/2$, with the possible addition of an additional constant observable to account for the mean of the data. We will not closely concern ourselves with how closely we may approximate the true Koopman operator using such a choice of observables, but will rather show that, in any case, the elements of the identified dynamics on this space of observables may be used to construct a nonlinear model of the system dynamics. To this end, we start by explicitly writing the identified dynamics using this approach by

$$\begin{bmatrix} a_1 \\ a_2 \\ \vdots \\ a_r \\ (a_1)^2 \\ a_1 a_2 \\ \vdots \\ (a_r)^2 \end{bmatrix}_{t+\Delta t} = \begin{bmatrix} l_1^1 & l_2^1 & \cdots & l_r^1 & q_1^{11} & q_1^{12} & \cdots & q_r^{rr} \\ l_2^1 & l_2^2 & \cdots & l_2^r & q_2^{11} & q_2^{12} & \cdots & q_2^{rr} \\ \vdots & \vdots & \ddots & \vdots & \vdots & \vdots & \ddots & \vdots \\ l_r^1 & l_r^2 & \cdots & l_r^r & q_r^{11} & q_r^{12} & \cdots & q_r^{rr} \\ l_{11}^1 & l_{11}^2 & \cdots & l_{11}^r & q_{11}^{11} & q_{11}^{12} & \cdots & q_{11}^{rr} \\ l_{12}^1 & l_{12}^2 & \cdots & l_{12}^r & q_{12}^{11} & q_{12}^{12} & \cdots & q_{12}^{rr} \\ \vdots & \vdots & \ddots & \vdots & \vdots & \vdots & \ddots & \vdots \\ l_{rr}^1 & l_{rr}^2 & \cdots & l_{rr}^r & q_{rr}^{11} & q_{rr}^{12} & \cdots & q_{rr}^{rr} \end{bmatrix} \begin{bmatrix} a_1 \\ a_2 \\ \vdots \\ a_r \\ (a_1)^2 \\ a_1 a_2 \\ \vdots \\ (a_r)^2 \end{bmatrix}_t. \quad (5.3.6)$$

Focusing on a single POD coefficient (i.e., one of the first r rows of Eq. 5.3.6), we have that

$$a_k(t + \Delta t) = \sum_{i=1}^r l_k^i a_i(t) + \sum_{\substack{i,j=1 \\ j \leq i}}^r q_k^{ij} a_i(t) a_j(t), \quad (5.3.7)$$

which is the same form as Eq. (5.2.5), but in discrete-time. Thus, by taking the first r rows of the \mathbf{A} matrix obtained from performing EDMD with observables given by Eq. (5.3.5), we may obtain a system of nonlinear equations that can accurately model the evolution of the POD coefficients of the system in discrete time.

While we may expect that the first r rows of \mathbf{A} give an accurate model for the evolution of POD coefficients, in general we should not expect the same for the evolution of the quadratic monomials of POD coefficients. This is because the equations for the evolution of these terms should involve cubic terms, which are not spanned by our observables. Incidentally, this suggests that using any basis of polynomial observables for approximating the Koopman operator for the Navier-Stokes problems might be problematic. One possible alternative, not explored in this work, is to use the Kernel variant of EDMD [161] with an appropriately chosen kernel function that better spans the Koopman eigenfunctions.

5.3.3 A modification to DMD/EDMD

When in the least squares regime (i.e., when there are fewer observables than the number of snapshot pairs), Eqs. (6.2.1) and (5.3.4) can give solutions with large entries in \mathbf{A} . Empirically, these entries can be significantly larger in magnitude than those expected, say, from performing a Galerkin projection. It also appears that this “overfitting” can give models that lack stability. To mitigate these observations, we propose a simple modification to DMD/EDMD that penalizes

DISTRIBUTION A: Distribution approved for public release.

the size of entries in \mathbf{A} . Note that the same process can be applied to both DMD and EDMD, whenever the data matrix \mathbf{Y} has more columns than rows. When this is the case, Eq. (5.3.4) gives the solution to the minimization problem

$$\mathbf{A} = \text{argmin}_{\mathbf{M}} \|\mathbf{M}\mathbf{Y} - \mathbf{Y}^\# \|_F^2. \quad (5.3.8)$$

We may add a penalization on the size of the entries of \mathbf{A} to formulate a joint least squares problem

$$\mathbf{A} = \text{argmin}_{\mathbf{M}} \left(\|\mathbf{M}\mathbf{Y} - \mathbf{Y}^\# \|_F^2 + \beta^2 \|\mathbf{M}\|_F^2 \right), \quad (5.3.9)$$

where β is a parameter that determines the extent to which large entries in \mathbf{M} are penalized. The element-wise nature of the Frobenius norm means that Eq. (5.3.9) may be rearranged to give

$$\mathbf{A} = \text{argmin}_{\mathbf{M}} \left\| \mathbf{M} [\mathbf{Y} \ \beta \mathbf{I}] - [\mathbf{Y}^\# \ \mathbf{0}] \right\|_F^2, \quad (5.3.10)$$

where \mathbf{I} and $\mathbf{0}$ are appropriately sized matrices. Note that this modification of DMD/EDMD is similar to the principle of Tikhonov regularization. Eq. (5.3.10) has an explicit solution, given by

$$\mathbf{A} = \mathbf{Y}^\# [\mathbf{Y} \ \beta \mathbf{I}]^+. \quad (5.3.11)$$

We remark that this regularization is equivalent as adding to the data set pairs of snapshots where each observable goes from some nonzero value β to 0 over a timestep of Δt . It should also be noted that Tikhonov regularization methods have been used previously as a method of calibrating GP models[35], and have also been used for other system identification techniques, such as finite impulse response models[76]. More generally, one can add a variety of different forms of penalty terms to obtain a desired balance between competing objectives. For example, in the context of EDMD, [162] uses a $L_{1,2}$ minimization to obtain what in our notation would be a solution with a small number of nonzero columns of \mathbf{A} .

5.4 Example: flow past a circular cylinder

We test our proposed method using the much-studied example of 2D flow past a circular cylinder. Beyond a critical Reynolds number of approximately 47 [107], the equilibrium becomes unstable and the system will instead converge upon a limit cycle characterized by periodic vortex shedding. We take data for $Re = 60$, with the initial condition close to the unstable equilibrium. The data captures the initial growth of an instability near the unstable equilibrium, through to convergence to the limit cycle. This is an example where regular DMD will fail (in the sense of identifying an appropriate reduced order model), since the process (which is a Hopf bifurcation) is fundamentally nonlinear. In particular, beyond the critical Reynolds number, the nonlinear terms must become non-negligible to balance the growth of the unstable linear dynamics, leading to the observed limit cycle behavior.

We will explore the performance of both EDMD and GP models on this system for a range of data, including that which is noisy and spatially truncated or sparse. The data was obtained from direct numerical simulation using an immersed boundary projection method [139, 34]. Selective frequency damping [3] was used to obtain the unstable equilibrium solution. To focus on the transitional region of the dynamics, the snapshots to be used were collected after first running the simulation from the unstable equilibrium for $250 \frac{D}{U}$ time units. The simulation was performed on a domain consisting of five nested grids, as shown in Fig. 5.1. Each grid is uniform, with the finest

DISTRIBUTION A: Distribution approved for public release.



Figure 5.1: Computational domain used for numerical simulation of flow past a circular cylinder. Dashed lines represent the borders of each nested grid. The gray shading denotes the region from which data was collected for modeling purposes

grid having a grid spacing of $0.02D$ in each direction, and each successively larger grid having double the grid spacing of the previous. The full domain has size $256D \times 64D$. This large domain was chosen so as to resolve both the flowfield on the region of the grid used for analysis (shown in gray), and the forces incident on the cylinder, to a high degree of accuracy.

This comparison between the performance of EDMD and GP models begins in a scenario where both models work relatively well: where clean data encompassing a large spatial domain is available across a window of time spanning all of the distinct dynamic regimes. While we find that GP models can indeed outperform the EDMD models that we identify in favorable conditions, we will proceed to demonstrate that in the cases where the data is noisy or restricted, EDMD models can perform substantially better.

5.4.1 Data arrangement and selection

The data to be used was taken from the gray shaded region in Fig. 5.1. As mentioned previously, we evolve the system from the equilibrium for some time ($250\frac{D}{U}$) before collecting data, then collect 1000 snapshots separated by a uniform timestep $\Delta t = 0.2\frac{D}{U}$. This time interval spans the growth of the instability from near the equilibrium, through to the convergence of the flow to a periodic limit cycle. We note that Galerkin projection in particular is quite sensitive to the resolution and extent of data chosen. For this reason, we do not claim that the GP models that we identify are the most accurate that can be obtained for such a system, but still serve as a basis for comparison to the EDMD models that are identified for the same choice of data.

The EDMD procedure requires a selection of observables. Despite narrowing down this choice substantially by choosing to work with linear and quadratic monomials of POD coefficients, there can still be some additional ambiguity that should be explicitly clarified. To begin with, one must decide how whether to subtract the mean flow from the data before applying POD. This step is almost always performed when performing POD, partly because then any reconstruction of the flow using a linear combination of POD modes will automatically satisfy the required boundary conditions [66]. Conversely, it is almost never done with DMD; doing so can lead to an undesirable equivalence to taking a discrete Fourier transform [27]. Furthermore, if one is to subtract a “mean”, for this flow one could conceivably take this to be any of the mean of the limit cycle, the mean of the data, or even the unstable equilibrium velocity field. To emphasize the fact that we are approaching this procedure from a data-driven perspective, and to be consistent with the subspace used for both procedures, here we first subtract the mean of the data before performing POD (for both GP and EDMD models). Note that this is different to what is typically done when constructing GP models for such a system, where the mean is most typically taken to be the mean of the limit cycle (e.g., [95]). The mean and POD modes identified in this manner, as well as their relative energy content

and the temporal evolution of their coefficients, are shown in Fig. 5.2.

We further note that subtracting the mean of the velocity field before performing POD does not result in all of the observables used for EDMD having zero mean, as $(a_i)^2$ is always non-negative. When performing EDMD, we can also choose whether to explicitly include this mean mode as an observable, which amounts to allowing for a constant term in Eq. 5.3.6. We will most often choose to do this, though will discuss this in more detail later. On top of all of these details, the regularization introduced in Sect. 5.3.3 introduces an additional parameter whose value must be set, which we will discuss in the next section.

5.4.2 Comparison between EDMD and GP models, regularization, and model order dependence

This section analyzes the performance of both EDMD and GP models of a range of orders in modeling the dynamics of the flow past a cylinder. We begin with some sample results. Fig. 5.3 shows the performance of both Galerkin projection, and the EDMD approach outlined in Sect. 5.3, in identifying a model that can predict the evolution of the first three POD coefficients. For this system, the dynamics of these coefficients are known to evolve on a paraboloid [95]. We observe that the EDMD model is more accurate than the GP model in terms of obtaining both the correct transient and limit cycle behavior. Fig. 5.4 shows that the same findings hold when the dimension of the models increase to 9. We keep β at a fixed value of 0.5 for both of these examples, which will be the default unless otherwise mentioned.

In order to study more systematically the accuracy of models of various order, we compare in Fig. 5.5 the identified limit cycle amplitude (defined based on the coefficient of the first POD mode) and frequency for models of order 3–28. As well as showing results for EDMD models identified with $\beta = 0.5$, we additionally show the performance of models identified with an optimized value of β , where the optimal is found based on a direct search over the range $0 \leq \beta \leq 2$. This comparison shows that the results are relatively insensitive to β , and that the one initially chosen value tends to perform reasonably well across all model orders. It would be possible, however, to develop more sophisticated methods to tune β using the data available. To do this, one could apply standard extrema-seeking algorithms to find a value of β that allows the identified model to best match the data, by some chosen metric. One could also explore the possibility of replacing the $\beta \mathbf{I}$ term in Eq. 5.3.10 with a diagonal matrix with different entries, though this then loses the direct connection to the joint least squares problem formulated in Eq. 5.3.9.

In general, EDMD models are more accurate than GP models at predicting the limit cycle characteristics for models of order less than 8, while GP models are more accurate for high order, except for models of order 14, where the GP model performs uncharacteristically poorly. While for this simple system the high order models are not required to obtain an accurate representation of the system dynamics, it is important to verify that the proposed algorithm remains capable of identifying stable and accurate models as the model order increases, in order to be of use for more complex fluids systems.

5.4.3 Model prediction for untrained conditions

An important feature of any identified model is the ability to predict the behavior of the system along trajectories in phase space that are not contained in the data used for model identification.

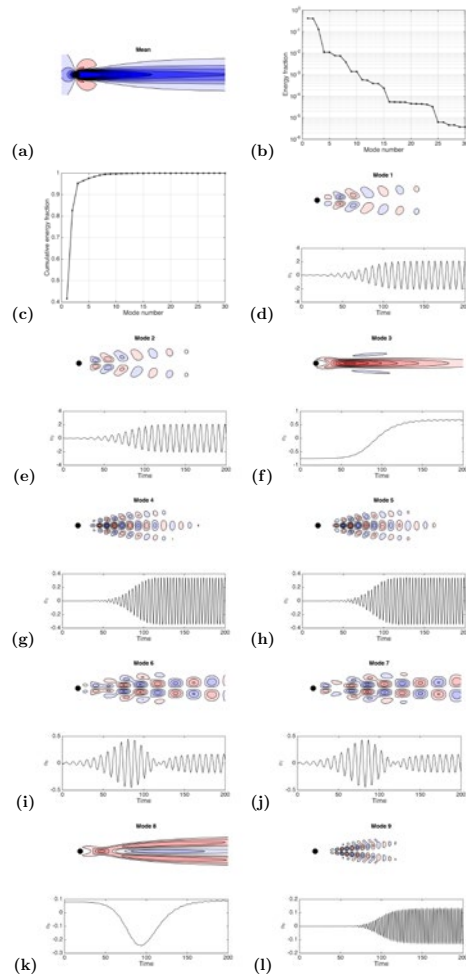


Figure 5.2: (a) Mean mode, (b) relative energy content and (c) cumulative energy content of the first 30 POD modes identified from data collected as the flow transitions from near the unstable equilibrium to the limit cycle. (d)-(l) Contours of streamwise velocity for the first nine POD modes, and their corresponding time-varying coefficients

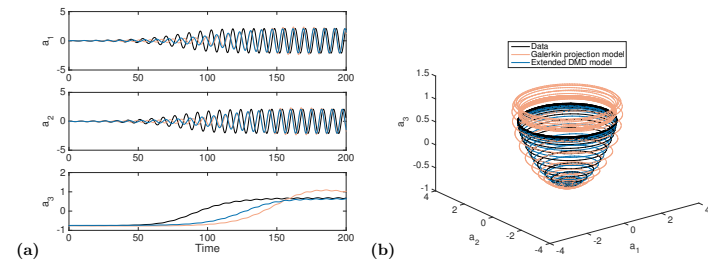


Figure 5.3: Performance of 3rd order GP and EDMD nonlinear models in predicting the evolution of POD coefficients for transitional flow past a cylinder, showing (a) time evolution and (b) phase portrait plots. The Galerkin and EDMD phase portrait models are allowed to evolve for 800 dimensionless time units to confirm limit cycle behavior

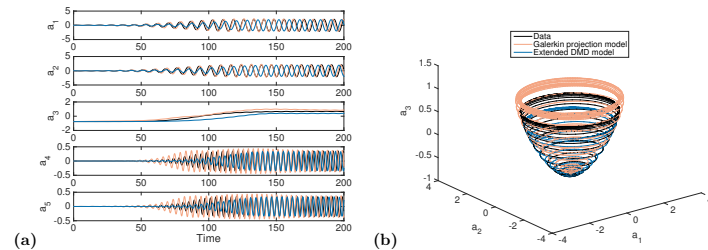


Figure 5.4: Performance of 9th order GP and EDMD nonlinear models in predicting the time-evolution of POD coefficients for transitional flow past a cylinder, showing (a) time evolution and (b) phase portrait plots. Only the first 5 modes are shown on the left, while the phase portrait shows the projection onto the first 3 modes. The Galerkin and eEMD phase portrait models are allowed to evolve for 800 dimensionless time units to confirm limit cycle behavior

DISTRIBUTION A: Distribution approved for public release.

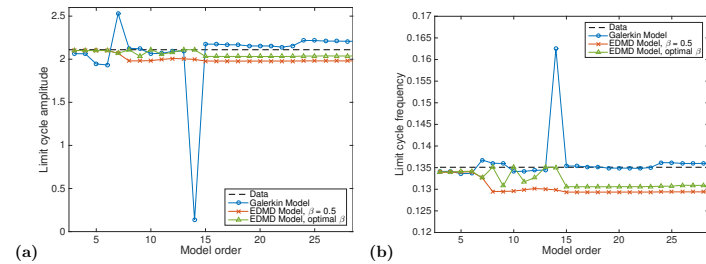


Figure 5.5: Prediction of the limit cycle amplitude (a) and frequency (b) of the first POD mode from both EDMD and GP models

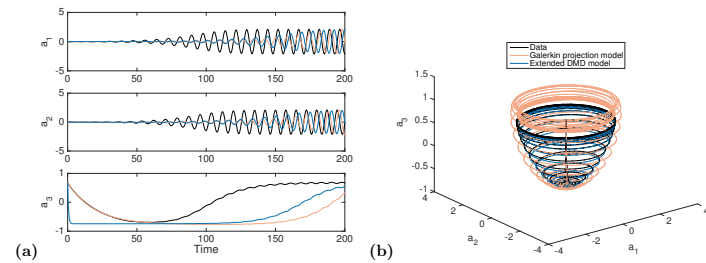


Figure 5.6: Performance of 3rd order GP and EDMD nonlinear models in predicting the evolution of POD coefficients for transitional flow past a cylinder, showing (a) time evolution and (b) phase portrait plots. The initial condition is taken to be the mean of the limit cycle

This ensures the practical utility of such a model, and increases confidence that the “correct” system dynamics are being captured. We show in Fig. 5.6 the performance of 3rd order EDMD and GP models in predicting the evolution of the first 3 POD coefficients, starting at the mean of the limit cycle. We observe that the GP model more accurately captures the initial transient as the flow approaches the slow manifold (paraboloid), though as before the EDMD model is more accurate in predicting the subsequent approach to the limit cycle. Note that there are two main reasons why this model might be somewhat inaccurate in the untrained region: not only are the dynamics in this region untrained, but the POD basis is additionally no longer energetically optimal (in terms of energy) for this dataset, so low order models in particular might not capture features that are both energetically and dynamically important.

DISTRIBUTION A: Distribution approved for public release.

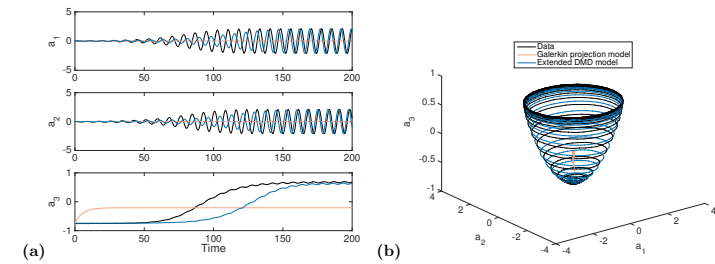


Figure 5.7: Performance of 3rd order GP and EDMD nonlinear models in predicting the evolution of POD coefficients for transitional flow past a cylinder, showing (a) time evolution and (b) phase portrait plots. The Galerkin and EDMD phase portrait models are identified from data that is corrupted by noise of standard deviation $\sigma = 0.05U$. $\beta = 0.5$

5.4.4 Noisy data

An important quality for any modeling procedure to possess is a robustness to noisy data, such as that which might be acquired from experiments. In Fig. 5.7, we show the results of identifying 3rd order models to the same data as considered previously, but corrupted by Gaussian white noise, with magnitude of 5% of the freestream velocity. It is observed that the EDMD model retains its accuracy, whereas the GP model captures none of the observed features of the system. This result is interesting, since the noise-corrupted data is actually being used to identify the dynamics in the case of EDMD, whereas GP only uses the data to obtain a spatial basis. As well as showing the robustness of the EDMD modeling procedure, these results highlight the sensitivity of GP to this basis selection.

5.4.5 Data from a restricted spatial domain

Another potential drawback of GP models is that they require spatially resolved data across a wide domain, ideally such that the boundary conditions are constant. In Fig. 5.8, we attempt to obtain reduced order models using a small portion of the domain. Unlike GP, EDMD is still able to produce an accurate model with such a restricted data set. Here, we are only using the data collected from this limited domain to compute POD, so the modes that are computed will differ somewhat from the modes shown in Fig. 5.2. The fact that EDMD models in this case retain their accuracy for both noisy data and restricted spatial domains suggests that this modeling framework could be particularly useful for experimental data, which often possesses both limitations.

An advantage of EDMD is that it does not require spatially resolved data, which is required for the computation of spatial derivatives in GP. In Fig. 5.9, we show that EDMD can produce an accurate ROM with only data from a small number of sparse, randomly chosen points. This gives cause for optimism that the method could additionally be used in experiments for which only point sensor measurements are available, rather than the spatially resolved flowfields, which can be more costly and time consuming to obtain. While the selection of the sensor locations in this case was

DISTRIBUTION A: Distribution approved for public release.

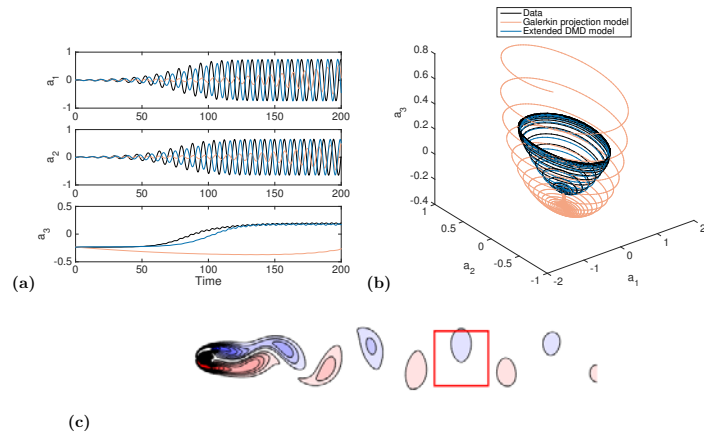


Figure 5.8: Performance of 3rd order GP and EDMD nonlinear models in predicting the evolution of POD coefficients for transitional flow past a cylinder, showing (a) time evolution and (b) phase portrait plots. Only data contained from inside the square shown in (c) is used for model identification. The EDMD models were obtained with $\beta = 0.1$

DISTRIBUTION A: Distribution approved for public release.

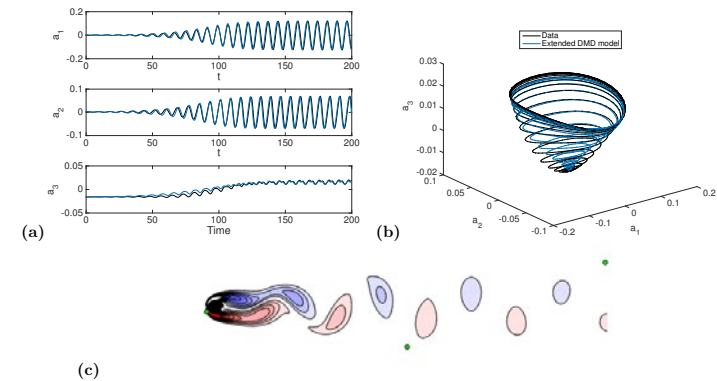


Figure 5.9: Performance of 3rd order GP and EDMD nonlinear models in predicting the evolution of POD coefficients for transitional flow past a cylinder, showing (a) time evolution and (b) phase portrait plots. Only data sampled at green circles shown in (c) are used for model identification

random, we observed empirically that best results were obtained when the sensor locations were spread across different spatial regions of the domain. When using only a small number of point sensors, we found that better models were obtained when we did not include a constant term in our set of observables. We additionally did not use any form of regularization.

5.4.6 Data from limited temporal sampling

In this section, we explore the ability of EDMD and GP models in predicting the evolution of a system using only a small amount of temporal data. As in Sect 5.4.5, we compute POD modes (including the mean modes) from the subset of data that is used. Note in particular that this means that the POD basis that we use as our state space will be different to those identified from the full dataset. In Fig. 5.10, we show the results of applying both EDMD and GP when using only the first 40%, 20%, and 10% of the time series of data used for the previous sections. We find that, even when the data available is significantly reduced and has clearly not reached the limit cycle, the EDMD models still accurately predict the presence (and to some extent, the location) of the limit cycle. This is in contrast to the GP model, where the limited data available renders the model qualitatively incorrect for all amounts of data used. Note that the results in this section did not use any form of regularization.

DISTRIBUTION A: Distribution approved for public release.

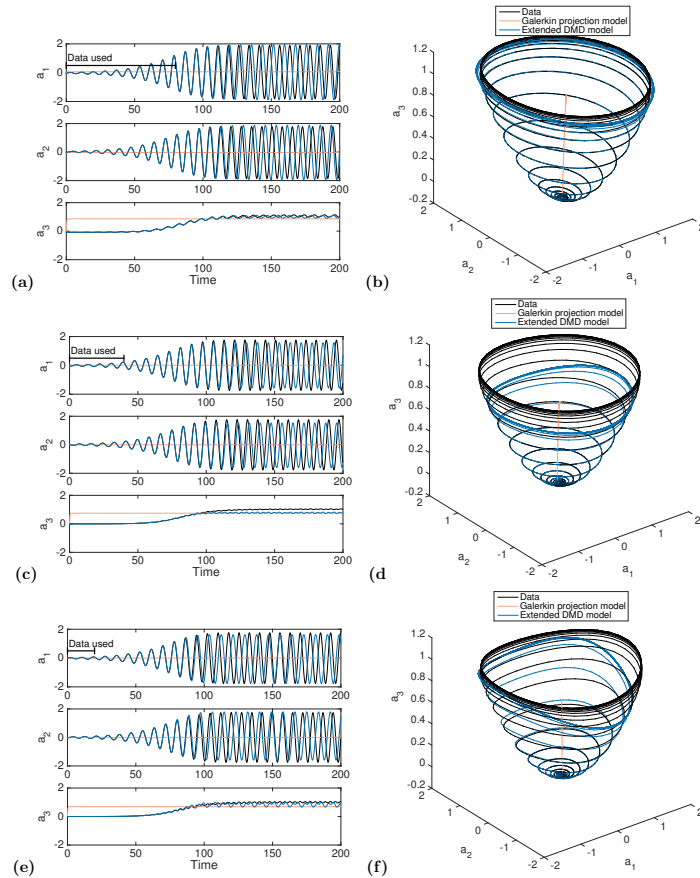


Figure 5.10: Performance of 3rd order GP and eDMD nonlinear models in predicting the evolution of POD coefficients for transitional flow past a cylinder, showing (a) time evolution and (b) phase portrait plots. Models are identified using only the first 400 (top), 200 (center) and 100 (bottom) snapshots of data, as shown

DISTRIBUTION A: Distribution approved for public release.

5.5 Discussion and conclusions

This work has introduced a method to extract low-order, nonlinear models from time-resolved data, by utilizing an extension of the DMD algorithm. Through the use of a variety of different types of data from a simple example of a nonlinear fluids system, we have attempted to evaluate the relative performance of this method in a range, in comparison with Galerkin projection.

We believe that the advantages of the present approach are numerous. We have demonstrated that this data-driven approach appears to be more robust to noisy data, and exhibits greater flexibility in terms of the spatial extent and resolution of data for which the method produces accurate models. We therefore hold strong hopes that this method will be useful in particular to model experimental data, which often contains such limitations.

Beyond this, the present method requires no explicit knowledge of the underlying governing equations, though here knowing at least the form of the nonlinearity was advantageous. In particular, note that the correct form of the observables is most likely important when the nonlinear model is used to extrapolate a small amount of data, and ultimately correctly predict the limit cycle in Sect. 5.4.6. In other words, if the correct form of the nonlinearity is known, then even a small sample of data can be sufficient to identify a model that is at least qualitatively accurate. This finding has important implications for more complicated systems, where sampling across all possible regimes and/or locations in phase space may be infeasible.

In Sect. 5.4.1, it was observed that EDMD models are particularly accurate when the dimension of the model is small, in comparison to both GP models of the same order, and EDMD models of higher order. The fact that GP models are less accurate for lower model orders is unsurprising, since (without any additional modification) they have no way of accounting for the effect of unmodeled modes. EDMD models, on the other hand, can at least account for the time-averaged effect of modes that are not explicitly included as variables. Note, however, that unmodeled modes with highly intermittent dynamics could be impossible to accurately account for. As the model order increases, GP models should be expected to become more accurate, as the effect of unmodeled modes reduces. Conversely, we find that EDMD models can become less accurate and robust, possibly due to the rapid increase in the number of parameters requiring to be fit. Note that a phenomenon has been observed previously in polynomial identification [102].

The mathematical machinery behind DMD and its variants involves a least squares (or minimum norm, in the underconstrained case) fit of data. In this sense, the method presented in this work shares strong similarities with a number of other methods that have been used to identify nonlinear systems in fluids, such as polynomial identification [102], modified quadratic stochastic estimation [94] Volterra system identification [11], and linear parameter varying system identification [60], which all employ a similar type of least-squares coefficient-fitting methodology in their respective algorithms. The recently developed SINDy [24] (sparse identification of nonlinear dynamics) also employs a similar basic framework, though with an additional sparsity-promoting algorithm to decide upon the appropriate observables from a larger library, which is particularly useful when the form of the nonlinearity is unknown. In this sense, we do not claim that the algorithm we use is exceptionally novel, but hope that this exposition, both in terms of the connections of DMD and Koopman theory, and in highlighting a number of situations where such a modeling approach might be advantageous or necessary. On the former point, one could hope that EDMD, with the correct choice of observables, can allow for accurate prediction not just of Koopman eigenvalues and eigenmodes, but also Koopman eigenfunctions. There is indeed strong evidence to suggest that identified Koopman eigenfunctions can indeed give an accurate characterization of the dynamics of the cylinder wake near the limit cycle [7]. We do not make any claims that we have achieved such convergence here over the full transient regime, but rather show that the results can still be useful

DISTRIBUTION A: Distribution approved for public release.

from a practical, model-reduction standpoint. We do not make any claims that we have achieved such convergence here, but show that the results can still be useful from a practical, model-reduction standpoint. As well as pursuing this direction, further work could seek to utilize such models for purposes of flow control. Preliminary investigations also suggest that such EDMD-based models can be effective at identifying stability properties, such as eigenvalues of the linearized system at equilibrium points.

Chapter 6

Characterizing and correcting for the effect of sensor noise in the dynamic mode decomposition

Dynamic mode decomposition (DMD) provides a practical means of extracting insightful dynamical information from fluids datasets. Like any data processing technique, DMD's usefulness is limited by its ability to extract real and accurate dynamical features from noise-corrupted data. Here we show analytically that DMD is biased to sensor noise, and quantify how this bias depends on the size and noise level of the data. We present three modifications to DMD that can be used to remove this bias: (i) a direct correction of the identified bias using known noise properties, (ii) combining the results of performing DMD forwards and backwards in time, and (iii) a total least-squares-inspired algorithm. We discuss the relative merits of each algorithm, and demonstrate the performance of these modifications on a range of synthetic, numerical, and experimental datasets. We further compare our modified DMD algorithms with other variants proposed in recent literature.

6.1 Introduction

With advances in both experimental techniques and equipment, and computational power and storage capacity, researchers in fluid dynamics can now generate more high-fidelity data than ever before. The presence of increasingly large data sets calls for appropriate data analysis techniques, that are able to extract tractable and physically relevant information from the data. Dynamic mode decomposition allows for the identification and analysis of dynamical features of time-evolving fluid flows, using data obtained from either experiments or simulations. In contrast to other data-driven modal decompositions such as the proper orthogonal decomposition (POD), DMD allows for spatial modes to be identified that can be directly associated with characteristic frequencies and growth/decay rates. Following its conception, DMD was quickly shown to be useful in extracting dynamical features in both experimental and numerical data [125, 126]. It has subsequently been used to gain dynamic insight on a wide range of problems arising in fluid mechanics [e.g., 128, 127, 70] and other fields [e.g., 59].

DMD has a strong connection to Koopman operator theory [81, 88], as exposed in [119], and further reviewed in [89], which can justify its use in analyzing nonlinear dynamical systems. Since its original formulation, numerous modifications and extensions have been made to DMD. [27] highlights the connection that DMD shares with traditional Fourier analysis, as well as proposing an optimized algorithm that recasts DMD as an optimal dimensionality reduction problem. This

concept of finding only the dynamically important modes has also been considered in subsequent works of [164] and [71]. All of these works are motivated, in part, by the fact that by default DMD will output as many modes as there are pairs of snapshots (assuming that the length of the snapshot vector is greater than the number of snapshots), which is arbitrary with respect to the dynamical system under consideration. In reality, one would prefer to output only the modes and eigenvalues that are present (or dominant) in the data. When the data is corrupted by noise (as will always be the case to some degree, especially for experimental data), this process becomes nontrivial, since noisy data might have a numerical rank far larger than the dimension of the governing dynamics of the system. Further to this, one cannot expect to have a clean partition into modes that identify true dynamical features, and those which consist largely of noise.

Simple ways of achieving this objective can involve either first projecting the data onto a smaller dimensional basis (such as the most energetic POD modes) before applying DMD, or by choosing only the most dynamically important DMD modes after applying DMD to the full data. One can also truncate the data to a dimension larger than the assumed dimension of the dynamics, and then apply a balanced truncation to the resulting dynamical system to obtain the desired reduced order model. This approach is sometimes referred to as *over-specification* in the system identification community [see, e.g., 75]. Keeping a higher dimension of data than that of the assumed dynamics can be particularly important for input-output systems that have highly energetic modes that are not strongly observable or controllable [112]. Ideally, any algorithm that restricts the number of DMD modes that are computed should also additionally be computationally efficient. A fast method to perform DMD in real time on large datasets was recently proposed in [62], while a library for efficient parallel implementation of number of common modal decomposition and system identification techniques is described in [16]. An extension of DMD that potentially allows for better representation of nonlinear data has also recently been proposed [160], and although the computational costs increase dramatically with the dimension of the system, a kernel method described in [161] reduces the cost to be comparable to standard DMD.

One of the major advantages of DMD over techniques such as global stability analysis, for example, is that it can be applied directly to data, without the need for the knowledge or construction of the system matrix, which is typically not available for experiments [126]. For this reason, analysis of the sensitivity of DMD to the type of noise typically found in experimental results is of particular importance. The effects of noise on the accuracy of the DMD procedure was systematically investigated in the empirical study of [44], for the case of a synthetic waveform inspired by canonical periodic shear flow instabilities. More recently, [101] have extended this type of analysis to more complex data with multiple frequencies, as might be found in typical fluids systems. The present work builds upon these previous studies by analytically deriving an expression that explicitly shows how DMD should be affected by noise, for the case where the noise is assumed to be sensor noise that is uncorrelated with the dynamics of the system. Our analysis complements the “noise-robust” DMD formulation in [63] by explicitly quantifying the influence of noise on DMD. Further, while our analysis is consistent with the total least-squares formulation in [63], we use the insights gained from our analysis to develop alternative techniques to total least-squares DMD that may be preferable in certain applications. Ultimately, the availability of multiple “noise-aware” DMD algorithms allows the user to approach dynamical analysis of noisy data from multiple angles, thus garnering more confidence in the computations. We note that the case of process noise, where noise can interact with the dynamics of the system, is also the subject of recent work [8].

Our analysis uses a recent characterization of DMD [149], which highlights the connection of DMD to related techniques that are used in other communities for the extraction of dynamical information from data. Many linear system identification techniques are closely related in that they are based around singular value decomposition of a data matrix; aside from DMD there is

the eigensystem realization algorithm [72] and balanced proper orthogonal decomposition [112], for example. Indeed, the origin of such an approach seems to date back to the work of [65].

In this work, we first show that the dominant effect of noise on DMD is often deterministic. This not only allows us to accurately predict its effect, but also allows for a correction to be implemented to recover the noise-free dynamics. As well as directly correcting for the noise, we present two other modifications of DMD, that both are able to remove this bias without needing to know the noise characteristics. Sect. 6.2 develops the theory that characterizes the effect of noise on DMD, which subsequently motivates the formulation of our modified algorithms, which we term *noise-corrected* DMD (ncDMD), *forward-backward* DMD (fbDMD) and *total least-squares* DMD (tlsDMD). In Sect. 6.3, we analyze the performance of these algorithms on a number of synthetic data sets, which are corrupted by Gaussian white noise. We additionally investigate how the algorithms perform on data with both sensor and process noise. In Sect. 6.4, we use numerical and experimental data from flow past a cylinder undergoing periodic vortex shedding, to demonstrate the utility of the proposed modifications of DMD for real fluids data.

6.2 Characterizing noise in dynamic mode decomposition

This section details the methodology that is used to analyze the effect of noise in DMD. After introducing DMD in Sect. 6.2.1, the effect of sensor noise in the data on the results of DMD is studied in Sect. 6.2.2, which in particular shows that DMD is biased to sensor noise. Sects. 6.2.3–6.2.5 formulate three different modifications of the DMD algorithm that are designed to remove this bias.

6.2.1 Dynamic mode decomposition

DMD has undergone a number of formulations, interpretations and modifications since its inception. Common to all methods is the requisite collection and arrangement of data, summarized now. Suppose we collect snapshots of data \mathbf{x}_i , which we assemble as columns in the data matrix Z . For fluids systems \mathbf{x}_i will typically be a velocity field snapshot, but more generally it is a vector of observations of an evolving dynamical system at a given time. From Z , we select all pairs of columns that are sampled at a time difference Δt apart, and place them into the matrices X and Y (where the data in a given column of Y was collected Δt after the equivalent column of X). Note that if Z consists of a sequential time-series of data, then X and Y are simply Z with the last and first columns excluded, respectively. Let X and Y each be n by m matrices, so we have m pairs of snapshots, each of size n . By not explicitly requiring a single time-series of data, we allow for larger or irregular time gaps between snapshot pairs, the concatenation of data from multiple time-series, and for the removal of any corrupted or spurious data. Recently, [149] proposed an interpretation of DMD modes and eigenvalues as the eigendecomposition of the matrix

$$A = YX^+, \quad (6.2.1)$$

where X^+ denotes the Moore-Penrose pseudoinverse of a matrix X . While this is a succinct interpretation, and one which will be useful in the ensuing analysis, it is typically not an efficient (or even feasible) means of performing DMD (as discussed in [149]). This is especially true when $n \gg m$, which is often the case in high-dimensional fluids systems. Instead, since X and Y have rank at most $\min(m, n)$, it is typically more efficient to first project the data onto a subspace that is (at most) of this dimension. One way to do this is by projecting the original snapshots onto the POD modes of the data, which is implicitly done in all DMD algorithms. Note that the POD

modes of X are the columns of U in the singular value decomposition $X = U\Sigma V^*$ (though typically POD is performed after first subtracting the temporal mean of the data, which is not done here). We present here a typical algorithm to compute DMD, that is most similar to that proposed in [149] as *exact* DMD.

Algorithm 2 (DMD).

1. Take the reduced singular value decomposition (SVD) of X , letting $X = U\Sigma V^*$.
2. (Optional) Truncate the SVD by only considering the first r columns of U and V , and the first r rows and columns of Σ (with the singular values ordered by size), to obtain U_r , Σ_r , and V_r .
3. Let $\tilde{A} := U_r^* Y V_r \Sigma_r^{-1}$.
4. Find the eigenvalues μ_i and eigenvectors w_i of \tilde{A} , with $\tilde{A}w_i = \mu_i w_i$.
5. Every nonzero μ_i is a DMD eigenvector, with a corresponding DMD mode given by $\varphi_i := \mu_i^{-1} Y V_r \Sigma_r^{-1} w_i$.

This method is similar to the original formulation in [126], but for the fact that in step 5 the DMD modes are no longer restricted to lie within the column space of X . We also explicitly provide the optional step of truncating the SVD of X , which might be done if the system is known to exhibit low dimensional dynamics, or in an attempt to eliminate POD modes that contain only noise. We note that this is not the only means to reduce the dimension of the identified system dynamics, nor is it necessarily optimal. Indeed, [164] develops a method that optimizes the projection basis in parallel while performing a DMD-like eigendecomposition. [71] takes a different approach, seeking a small number of nonzero modes from the full eigendecomposition that best approximate the system dynamics. An empirical comparison between these various dimensionality-reduction techniques will be given in Sect 6.3.3. Note that the continuous eigenvalues λ_{ci} of the system are related to the discrete time eigenvalues identified via DMD via $\lambda_{ci} = \log(\mu_i)/\Delta t$. The growth rate γ_i and frequency ω_i associated with DMD mode φ_i are then given by $\lambda_{ci} = \gamma_i + i\omega_i$.

The matrix \tilde{A} is related to A in Eq. (6.2.1) by $\tilde{A} = U_r^* A U_r$. While A can be viewed as an approximating linear propagation matrix in \mathbb{R}^n (i.e., the space of original data vectors), \tilde{A} is the equivalent propagation matrix in the space of POD coefficients, which we will sometimes refer to as POD space. Another interpretation of \tilde{A} is that it is the spatial correlation matrix between the POD modes U_r , and the same POD modes shifted by the assumed dynamics A [126]. If we let $\tilde{\mathbf{x}}_k = U_r^* \mathbf{x}_k$ be the representation of a given snapshot \mathbf{x} in the POD basis and let $\tilde{X} = U_r^* X$ and $\tilde{Y} = U_r^* Y$, then it is easy to verify that the equivalent of Eq. (6.2.1) in POD space is

$$\tilde{A} = \tilde{Y} \tilde{X}^+. \quad (6.2.2)$$

Eq. (6.2.2) will be useful for the subsequent analysis performed in this paper.

6.2.2 Sensor noise in DMD

In this work we use the term sensor noise to describe additive noise that affects only our measurements of a given system, and does not interact with the true dynamics. If we have a discrete-time dynamical system

$$\mathbf{x}(t + \Delta t) = F[\mathbf{x}(t)],$$

DISTRIBUTION A: Distribution approved for public release.

then we assume that our measurements take the form

$$\mathbf{x}_m(t) = \mathbf{x}(t) + \mathbf{n}(t),$$

where $\mathbf{n}(t)$ is a random noise vector. For the purposes of this paper, we will take each component of $\mathbf{n}(t)$ to be independent and normally distributed with zero mean and a given variance. For instance, zero mean. I don't think we need to be pedantic about the probability theory here, but probably good to be a little more specific than this. With X and Y as described in Sect. 6.2.1, suppose that we measure $\tilde{X}_m = X + N_X$ and $\tilde{Y}_m = Y + N_Y$, where N_X and N_Y are random matrices of sensor noise. Note that some (or most) columns of random data in N_X might also be in N_Y , but shifted to a different column. We will assume that the noise is independent of the true data, and is independent in both space and time, so that each element of a given noise matrix is a random variable taken from a fixed zero-mean normal distribution. From Eq. (6.2.2), the measured DMD matrix \tilde{A}_m can be computed from

$$\begin{aligned} \tilde{A}_m &= \tilde{Y}_m \tilde{X}_m^+ = (\tilde{Y} + \tilde{N}_Y)(\tilde{X} + \tilde{N}_X)^+ \\ &= (\tilde{Y} + \tilde{N}_Y)(\tilde{X} + \tilde{N}_X)^* [(\tilde{X} + \tilde{N}_X)(\tilde{X} + \tilde{N}_X)^*]^+ \\ &= (\tilde{Y} \tilde{X}^* + \tilde{N}_Y \tilde{X}^* + \tilde{Y} \tilde{N}_X^* + \tilde{N}_Y \tilde{N}_X^*) \left[\tilde{X} \tilde{X}^* + \tilde{N}_X \tilde{X}^* + \tilde{X} \tilde{N}_X^* + \tilde{N}_X \tilde{N}_X^* \right]^+, \end{aligned} \quad (6.2.3)$$

where we have used the identity $M^+ = M^*(MM^*)^+$. Note that here the $\tilde{\cdot}$ notation means that the data is expressed in the POD basis obtained from the noisy data. We perform our analysis in this POD space rather than with the original data to allow for truncation of low energy modes, and because the computation of the pseudoinverse X^+ can be prohibitive for large datasets. We expect that the presence of noise should result in some error in the computation of \tilde{A}_m (in comparison to the noise free matrix \tilde{A}) and thus some amount of error in the computed DMD eigenvalues and modes. Since elements of \tilde{A}_m are statistical quantities dependent on the noise, it will make sense to compute statistical properties of the matrix. We begin by computing $\mathbb{E}[\tilde{A}_m]$, the expected value of the computed DMD matrix. Provided that we have truncated any POD modes with zero energy, $\tilde{X} \tilde{X}^*$ should be invertible. If the noise terms are sufficiently small, then we can make use of the matrix perturbed inverse expansion $(M + P)^{-1} = M^{-1} - M^{-1} P M^{-1} + \dots$, where higher order terms will be small for $M \gg P$. Eq. 6.2.3 then becomes

$$\tilde{A}_m = (\tilde{Y} \tilde{X}^* + \tilde{N}_Y \tilde{X}^* + \tilde{Y} \tilde{N}_X^* + \tilde{N}_Y \tilde{N}_X^*) (\tilde{X} \tilde{X}^*)^{-1} \left[I - (\tilde{N}_X \tilde{X}^* + \tilde{X} \tilde{N}_X^* + \tilde{N}_X \tilde{N}_X^*) (\tilde{X} \tilde{X}^*)^{-1} + \dots \right]. \quad (6.2.4)$$

Taking the expected value of Eq. (6.2.4), we may classify the terms into three categories: a deterministic terms that does not involve \tilde{N}_X or \tilde{N}_Y (which ends up being \tilde{A}), terms involving one or three noise matrices, which will have expected values of 0 (e.g., $\tilde{N}_Y \tilde{X}^* (\tilde{X} \tilde{X}^*)^{-1}$), and terms which involve two or four noise matrices. It is terms this latter category that may have non-zero expected values, and thus bias the result of applying DMD to noisy data. Discarding terms containing a single noise matrix, and additionally discarding higher order terms from the expansion, we have

$$\begin{aligned} \mathbb{E}(\tilde{A}_m) &= \tilde{A} (I - \mathbb{E}(\tilde{N}_X \tilde{N}_X^*) (\tilde{X} \tilde{X}^*)^{-1}) + \mathbb{E}(\tilde{N}_Y \tilde{X}^* \tilde{N}_X) \tilde{X}^+ + \mathbb{E}(\tilde{N}_Y \tilde{X}^* \tilde{X} \tilde{N}_X^*) (\tilde{X} \tilde{X}^*)^{-1} \\ &\quad + \tilde{Y} \mathbb{E}(\tilde{N}_X^* (\tilde{X} \tilde{X}^*)^{-1} \tilde{N}_X) \tilde{X}^+ + \tilde{Y} \mathbb{E}(\tilde{N}_X^* (\tilde{X} \tilde{X}^*)^{-1} \tilde{X} \tilde{N}_X^*) (\tilde{X} \tilde{X}^*)^{-1} \\ &\quad + \mathbb{E} \left[\tilde{N}_Y \tilde{N}_X^* (\tilde{X} \tilde{X}^*)^{-1} (I - \tilde{N}_X \tilde{N}_X^* (\tilde{X} \tilde{X}^*)^{-1}) \right], \end{aligned} \quad (6.2.5)$$

where we have noted that $\tilde{Y} \tilde{X}^* (\tilde{X} \tilde{X}^*)^{-1} = \tilde{Y} \tilde{X}^+ = \tilde{A}$. Assuming that the noise is sufficiently small compared with the true data, we can further neglect the term involving four noise matrices.

DISTRIBUTION A: Distribution approved for public release.

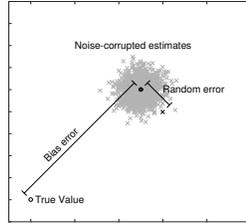


Figure 6.1: Illustrative diagram showing how the error in estimation of a given quantity can be decomposed into bias error (being the difference between the true and expected value of the identified quantity), and random error (representing the fluctuation in the estimated quantity between different noise realizations)

The largest of the remaining terms will be that which contains the product $\tilde{N}_X \tilde{N}_X^*$. The remaining terms do not necessarily have zero mean, but for the purposes of this investigation will be neglected. Our results will demonstrate that this simplification is justifiable. This reduces Eq. (6.2.5) to the following expression, relating the identified and true DMD matrices:

$$\mathbb{E}(\tilde{A}_m) = \tilde{A}(I - \mathbb{E}(\tilde{N}_X \tilde{N}_X^*)(\tilde{X}\tilde{X}^*)^{-1}). \quad (6.2.6)$$

It might seem surprising that Eq. (6.2.6) contains N_X , but not N_Y . The reason for this will become apparent in Sect. 6.2.5, where casting DMD in an optimization framework shows that the standard algorithm is optimal only when assuming that all of the noise is in Y , but not X . From a mathematical point of view, it is because the expression $\tilde{A} = Y\tilde{X}^+$ is linear in Y but not in \tilde{X} , which is why perturbations to \tilde{X} do not have to propagate through the equation in an unbiased manner. Note that the same analysis can be performed without transforming into POD space (i.e., without the $\tilde{\cdot}$ notation), with the analogous expression to Eq. (6.2.6) being

$$\mathbb{E}(A_m) = A(I - \mathbb{E}(N_X N_X^*)(X X^*)^{-1}), \quad (6.2.7)$$

subject to $X X^*$ being invertible. For systems where the size of each snapshot is larger than the number of snapshots (i.e., $n > m$, which is typical for fluids systems), $X X^*$ will not be invertible, thus motivating our choice to work in POD space. Moreover, one might want the option to truncate all but a certain number of POD modes, in order to obtain a low-dimensional model for the dominant system dynamics. Up until this point, we have not made a distinction between the POD modes of the clean data, X , and the noisy measured data, X_m , with the latter typically being all that we have access to. This issue will be explicitly addressed in Sect. 6.2.3.

Eq. (6.2.6) shows that DMD is biased to sensor noise. In practice, the importance of this finding will depend on how the magnitude of this bias compares to the random component of error, that will fluctuate with different samples of random noise. Figure 6.1 shows an illustration of how bias and random components of error contribute to the total error in the estimation of some quantity from noisy data. Appendix 1 provides scaling arguments that suggest that the bias will be the dominant component of error in DMD whenever $m^{1/2}SNR > n^{1/2}$, where SNR is the signal-to-noise ratio. When this is the case, it would be particularly advantageous if one had access

DISTRIBUTION A: Distribution approved for public release.

to a bias-free alternative to DMD. The remainder of this section will present a number of such alternatives.

6.2.3 Direct correction of sensor noise bias in DMD

Referring back to Eq. (6.2.6), we can form a bias-free estimate of the true DMD matrix \tilde{A} via

$$\tilde{A} \approx \tilde{A}_m(I - \mathbb{E}(\tilde{N}_X \tilde{N}_X^*)(\tilde{X}\tilde{X}^*)^{-1})^{-1}. \quad (6.2.8)$$

Making this modification in practice requires an accurate estimate of both the noise covariance, $\mathbb{E}(\tilde{N}_X \tilde{N}_X^*)$, and the true data covariance, $\tilde{X}\tilde{X}^*$, in POD space. For noise that is sufficiently small, we can utilize the approximation

$$\tilde{X}\tilde{X}^* = U^* X X^* U \approx U_m^* X_m X_m^* U_m = \Sigma_m^2, \quad (6.2.9)$$

where $U_m \Sigma_m V_m^*$ is the singular value decomposition of the noisy data, X_m . This allows for us to express the bias of DMD in terms of quantities that are measurable from noisy data. The assumption that $X X^* = (X_m - N_X)(X_m - N_X)^* \approx X_m X_m^*$ can be further refined by retaining the $N_X N_X^*$ term, but for small noise this higher order term will typically be small enough to neglect after being inserted into Eq. (6.2.8). The assumption that $U \approx U_m$ will largely be justified by means of results that show the utility of this analysis. Analyzing the precise relationship between U and U_m in more detail is beyond the scope of this work, and is indeed an active area of research. We direct the interested reader to relevant results in perturbed SVD's [137, 138, 9], random inner product matrices [28, 141], and POD-type operations on noisy data [48, 133, 169].

Assuming that the noise is uniform as well as spatially and temporally independent, then $\mathbb{E}(\tilde{N}_X \tilde{N}_X^*) = \mathbb{E}(U^* N_X N_X^* U) = U^* m \sigma_N^2 U = m \sigma_N^2 I$, where σ_N^2 is the variance of each independent component of the noise matrix. With this assumption, and the approximation given in Eq. (6.2.9), Eq. (6.2.8) becomes

$$\tilde{A} \approx \tilde{A}_m(I - m \sigma_N^2 \Sigma_m^{-2})^{-1}. \quad (6.2.10)$$

If the noise is sufficiently small, then a perturbed inverse approximation gives

$$\tilde{A} \approx \tilde{A}_m(I + m \sigma_N^2 \Sigma_m^{-2}). \quad (6.2.11)$$

We thus have derived a correction to the bias that is present in the original DMD matrix A_m due to the effect of sensor noise. We note that this approximation relies on an accurate knowledge of the noise covariance matrix. There are numerous means to estimate noise properties from data, see [108], for example. The approximations used in deriving this expression also rely on the magnitude of the noise being smaller than that of the true data within each non-truncated POD mode. We now state explicitly the algorithm by which we can correct for the effect of sensor noise in the DMD algorithm, which we refer to as noise-corrected DMD, or ncDMD:

Algorithm 3 (Noise-corrected DMD (ncDMD)).

1. Compute \tilde{A}_m from the measured data as per steps 1–3 of Algorithm 2
2. Compute the approximation of \tilde{A} from Eq. (6.2.10)
3. Compute the DMD eigenvalues and modes via steps 4–5 of Algorithm 2, using the bias-free estimate of \tilde{A} .

DISTRIBUTION A: Distribution approved for public release.

As was also noted in Sect 6.2.2, we could have performed all of the above analysis without first projecting onto the space of POD coefficients, which gives us the following as analogous to Eqs. (6.2.10) and (6.2.11) respectively, subject to the appropriate inverses existing:

$$A \approx A_m(I - m\sigma_N^2(X_m X_m^*)^{-1})^{-1} \approx A_m(I + m\sigma_N^2(X_m X_m^*)^{-1}). \quad (6.2.12)$$

While this approach might be computationally prohibitive for many applications of DMD (since it requires inverting large $n \times n$ matrices), it could in theory be more accurate, since it doesn't rely on any assumption that the POD modes for the measured and true data are sufficiently close to each other. Note again that XX^* can only be invertible if $m > n$, as otherwise it cannot be full rank.

6.2.4 Forward-backward DMD

If we were to swap the data in X and Y , then (for suitably well behaved data) we should expect to identify the inverse dynamical system, with state propagation matrix B_m (or \tilde{B}_m in POD space), which approximates the true dynamics B (and \tilde{B}). Note that it is not guaranteed that the dynamics of the original system are invertible, but this assumption should not be too restrictive for the majority of physical systems under consideration (particularly after projection onto an appropriate POD subspace). It is argued in Appendix 1 that sensor noise has the effect of shifting the computed DMD eigenvalues to appear to be more stable than they actually are (i.e., moving them further inside the unit circle). Since our analysis was independent of the nature of the data, we should expect the same effect to be present for the computation of the inverse system. However, if \tilde{B} is invertible, then we should have $\tilde{B} = \tilde{A}^{-1}$, meaning that we should be able to compute an estimate of the forward-time propagation matrix using backward-time DMD, via $\tilde{A}_m^{back} = \tilde{B}_m^{-1}$. However, given that the eigenvalues of \tilde{B}_m should have their growth rates underestimated, those of the eigenvalues of \tilde{A}_m^{back} will be overestimated. Specifically, from consideration of Eq. (6.2.6), we have

$$\mathbb{E}(\tilde{B}_m) \approx \tilde{B} \left(I - \mathbb{E}(\tilde{N}_X \tilde{N}_X^*) (\tilde{X} \tilde{X}^*)^{-1} \right),$$

and so

$$\tilde{A}_m^{back} \approx \left(I - \mathbb{E}(\tilde{N}_X \tilde{N}_X^*) (\tilde{X} \tilde{X}^*)^{-1} \right)^{-1} \tilde{A}, \quad (6.2.13)$$

where we are using the fact that the noise and POD energy components are the same for forward- and backward-DMD. We can then combine estimates of the dynamics from forward- and backward-time DMD to obtain

$$\tilde{A}_m \tilde{A}_m^{back} = \tilde{A} \left(I - \mathbb{E}(\tilde{N}_X \tilde{N}_X^*) (\tilde{X} \tilde{X}^*)^{-1} \right) \left(I - \mathbb{E}(\tilde{N}_X \tilde{N}_X^*) (\tilde{X} \tilde{X}^*)^{-1} \right)^{-1} \tilde{A} = \tilde{A}^2. \quad (6.2.14)$$

We thus have the estimate

$$\tilde{A} \approx (\tilde{A}_m \tilde{A}_m^{back})^{1/2}. \quad (6.2.15)$$

Note that this square root will in general be non-unique, and thus determining which root is the relevant solution could be nontrivial. One reasonable method, if there is any ambiguity, is to take the square root which is closest to \tilde{A}_m (or \tilde{A}_m^{back}). See [53] for a more detailed discussion of the computation of matrix square roots. As an aside, note that if we assume that we know the equivalent continuous time matrices $\tilde{A}_m^c = \log(\tilde{A}_m)/\Delta t$ and $\tilde{A}_m^{c,back} = \log(\tilde{A}_m^{back})/\Delta t$, then the equivalent of Eq. (6.2.15) is

$$\tilde{A}^c \approx \frac{1}{2}(\tilde{A}_m^c + \tilde{A}_m^{c,back}).$$

We are now in a position to formalize this algorithm, which we refer to as *forward-backward* DMD or fbDMD.

DISTRIBUTION A: Distribution approved for public release.

Algorithm 4 (forward-backward DMD (fbDMD)).

1. Compute \tilde{A}_m from the measured data as per steps 1–3 of Algorithm 2
2. Compute \tilde{B}_m from the measured data as per steps 1–3 of Algorithm 2, where X and Y are interchanged
3. Compute the approximation of \tilde{A} from Eq. (6.2.15)
4. Compute the DMD eigenvalues and modes via steps 4–5 of Algorithm 2, using the improved estimate of \tilde{A} from step 4.

Note that in the case where most data snapshots are in both X and Y (e.g., for a sequential time series of data) we can reduce the computational cost of steps 1–2 in Algorithm 4 by first taking the SVD of the entire data set, and then working in the space of the resulting POD modes.

6.2.5 Total least-squares DMD

For the case where the number of snapshots, m , is greater than the size of each snapshot, n , the DMD matrix A can be interpreted as the least-squares solution to the overdetermined system $AX = Y$. When $n > m$, then the solution for the now underdetermined system is the minimum Frobenius norm solution to $AX = Y$. In both cases, this solution is $A = YX^+$. Note that it is possible to turn an under-determined system into an over-determined system by truncating the number of POD modes used to less than m (truncating to precisely m results in a unique solution when the data is full column rank, with no loss of data). A least-squares solution of this form minimizes the error in Y , but implicitly assumes that there is no error in X . This can explain why the bias in DMD (Eq. (6.2.6)) is dependent on \tilde{N}_X , but not \tilde{N}_Y . That is, in the least-squares case DMD can be viewed as finding

$$A : Y + E_Y = AX, \quad \text{minimizing } \|E_Y\|_F,$$

where $\|\cdot\|_F$ denotes the Frobenius norm of a matrix. When doing backwards-time DMD in Sect. 6.2.4, we conversely assume that Y is known exactly and minimize the error in X . That is, assuming the identified dynamics are invertible, we find

$$A : Y = A(X + E_X), \quad \text{minimizing } \|E_X\|_F.$$

For this reason, combining forward- and backward-time DMD takes into account the error in both X and Y . A more direct means of doing this is to use a single algorithm that finds a least-squares solution for the error in both X and Y . It is possible to adapt standard TLS algorithms [53] to a DMD setting, which we perform here. We seek

$$A : (Y + E_Y) = A(X + E_X), \quad \text{minimizing } \|E\|_F, \quad \text{where } E = \begin{bmatrix} E_X \\ E_Y \end{bmatrix}.$$

The expressions $Y + E_Y$ and $X + E_X$ can be interpreted as $Y_m - N_Y$ and $X_m - N_X$. To solve for this, we can rearrange the equation to obtain

$$\begin{bmatrix} A & -I \end{bmatrix} \begin{bmatrix} X + E_X \\ Y + E_Y \end{bmatrix} = 0. \quad (6.2.16)$$

DISTRIBUTION A: Distribution approved for public release.

We would now like to assume that $2n < m$. This might not be the case, particularly for high-dimensional fluids data. To get around this, and improve computational tractability, we may project Eq. (6.2.16) onto a POD subspace of dimension $r < m/2$, to obtain

$$[\tilde{A} \quad -I] \begin{bmatrix} \tilde{X} + \tilde{E}_X \\ \tilde{Y} + \tilde{E}_Y \end{bmatrix} = 0. \quad (6.2.17)$$

This POD projection step is in contrast to the TLS DMD formulation in [63], where a projection is performed onto a basis determined from an augmented snapshot matrix $Z = \begin{bmatrix} X \\ Y \end{bmatrix}$. We find that the present formulation yields more accurate eigenvalues in a number of examples. Note that the nullspace of $[\tilde{A} \quad -I]$ is r -dimensional, meaning that the $2r$ by m matrix $\begin{bmatrix} \tilde{X} + \tilde{E}_X \\ \tilde{Y} + \tilde{E}_Y \end{bmatrix}$ can have rank at most r .

Let the full SVD of $\begin{bmatrix} \tilde{X} \\ \tilde{Y} \end{bmatrix}$ be given by $U\Sigma V^*$. If the data is noisy, we should expect that all $2r$ diagonal entries of Σ are nonzero. By the Eckart-Young theorem [46], the nearest (in the sense of Frobenius norm) rank r matrix will be given by

$$\begin{bmatrix} \tilde{X} + \tilde{E}_X \\ \tilde{Y} + \tilde{E}_Y \end{bmatrix} = U\Sigma_{1:r}V^*,$$

where $\Sigma_{1:r}$ contains the leading r singular values of Σ , with the rest replaced by zeros. We then have that

$$\begin{bmatrix} \tilde{X} + \tilde{E}_X \\ \tilde{Y} + \tilde{E}_Y \end{bmatrix} = U\Sigma_{1:r}V^* = \begin{bmatrix} U_{11} & U_{12} \\ U_{21} & U_{22} \end{bmatrix} \begin{bmatrix} \Sigma_1 & 0 \\ 0 & 0 \end{bmatrix} \begin{bmatrix} V_1^* \\ V_2^* \end{bmatrix} = \begin{bmatrix} U_{11}\Sigma_1 V_1^* \\ U_{21}\Sigma_1 V_1^* \end{bmatrix},$$

where U_{ij} are r by r matrices, and V_1 is the first r columns of V . Rearranging this equation, we obtain the total least-squares estimate for \tilde{A} :

$$\tilde{A} = U_{21}U_{11}^{-1}. \quad (6.2.18)$$

Note that this derivation requires that U_{11} be invertible. While the derivation includes the full SVD of the augmented data, Eq. (6.2.18) indicates that we only need the first r columns of U , meaning that only a reduced SVD is required. Algorithm 5 summarizes this total least-squares approach to DMD, which we refer to as *total least-squares* DMD, or *tlsDMD*.

Algorithm 5 (total least-squares DMD (tlsDMD)).

1. Collect data X and Y , and project onto $r < m/2$ POD modes to obtain \tilde{X} and \tilde{Y} .
2. Take the SVD of $\begin{bmatrix} \tilde{X} \\ \tilde{Y} \end{bmatrix}$, letting $\begin{bmatrix} \tilde{X} \\ \tilde{Y} \end{bmatrix} = U\Sigma V^*$.
3. Partition the $2r$ by $2r$ matrix U into r by r sub-matrices, letting $U = \begin{bmatrix} U_{11} & U_{12} \\ U_{21} & U_{22} \end{bmatrix}$ (note that only the first r columns need to be computed).
4. Compute the total least-squares DMD matrix \tilde{A} , using Eq. (6.2.18).
5. Compute the DMD eigenvalues and modes using steps 4–5 of Algorithm 2.

An alternative and more focused exposition of *tlsDMD* is given in [63]. We note that Algorithm 5 is not identical to that presented in this work (due to the lack of pre-truncation of POD modes), however we find that Algorithm 5 gives marginally better results in terms of the accuracy of identified eigenvalues.

DISTRIBUTION A: Distribution approved for public release.

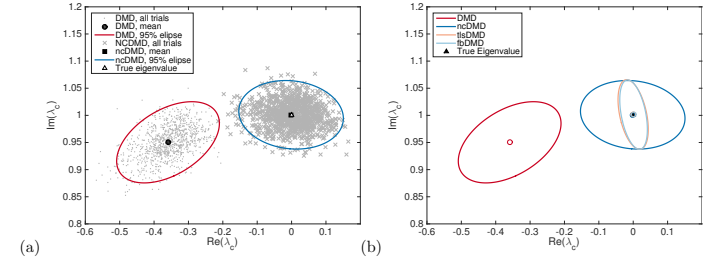


Figure 6.2: (a) Eigenvalues (in continuous-time) identified from regular DMD (Algorithm 2, dots) and noise-corrected DMD (Algorithm 3, crosses) from 100 snapshots of data from Eq. (6.3.1), with $\Delta t = 0.1$ and $\sigma_N^2 = 0.01$. Only one of the complex conjugate pair of eigenvalues is shown. The mean and 95% confidence ellipse of 1000 trials are given for each data set. (b) shows the mean and 95% confidence ellipse for the same data set for Algorithms 2–5

6.3 Results with synthetic data

In this section we will test our proposed modifications to DMD on a number of examples. Using known dynamics with the addition of random noise will allow us to examine the performance of these proposed modifications (Algorithms 3–5) in comparison to regular DMD (Algorithm 2). We begin by considering a simple 2-dimensional linear system in Sect. 6.3.1. In Sect. 6.3.2, we consider the same system with an expanded set of observables, which tests the important case of high-dimensional data that is described by low-dimensional dynamics. Sect. 6.3.3 compares the performance of the proposed modifications of DMD to other DMD variants in recent literature, while Sect. 6.3.4 considers the problem of identifying dynamics that are quickly decaying and obscured by dominant modes and noise, a case where DMD-like algorithms could be of most use. Finally, in Sect. 6.3.5 we analyze how the proposed DMD modifications treat process noise.

6.3.1 Example: A periodic linear system

We consider first a simple two-dimensional linear system, with dynamics given by

$$\dot{x} = \begin{bmatrix} 1 & -2 \\ 1 & -1 \end{bmatrix} x. \quad (6.3.1)$$

This system has (continuous-time) eigenvalues $\lambda_{c1,2} = \pm i$, so gives purely periodic dynamics, with no growth or decay. We discretize with a timestep $\Delta t = 0.1$, so the discrete-time eigenvalues are then $\lambda_{1,2} = e^{\pm i\Delta t}$. We use 100 timesteps of data (i.e., $m = 99$), corrupted with Gaussian white noise of variance $\sigma_N^2 = 0.01$. The identified continuous-time eigenvalues from both regular DMD (Algorithm 2), and the direct noise-correction (Algorithm 3) are shown in Fig. 6.2(a), for 1000 different trials from the initial condition $x_0 = [1 \ 0.1]^T$. We assume that the correction term is given by $m\sigma_N^2 I_n$, and observe that this corrects almost perfectly for the bias in the DMD algorithm in terms of identifying eigenvalues. Also shown in Fig. 6.2(a) are ellipses representing

DISTRIBUTION A: Distribution approved for public release.

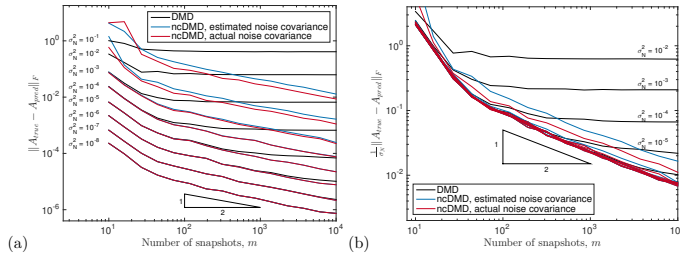


Figure 6.3: Error in the estimated propagation matrix \tilde{A} arising from performing DMD and ncDMD on noise-corrupted data generated from Eq. (6.3.1), for different values of m and σ_N^2 . In (a) the error is given as $\|\tilde{A}_{\text{true}} - \tilde{A}_{\text{pred}}\|_F$, while in (b) this quantity is normalized by the standard deviation of the noise, σ_N . In both cases, the error is averaged over 100 trials for each m and σ_N^2 . Note that for clarity, (b) excludes the two largest noise levels shown in (a)

the 95% confidence region, with the major and minor axes of the ellipse aligned with the principal component directions of the eigenvalue data. For clarity, in the presentation of subsequent results, we will omit individual data points and show only such ellipses. In Fig. 6.2(b) we show the mean and 95% confidence ellipses for Algorithms 4 and 5. As with ncDMD, both fbDMD (Algorithm 4) and tIsDMD (Algorithm 5) accurately correct for the bias in the mean of the identified eigenvalue. Further to this, fbDMD and tIsDMD also both reduce the area of the 95% confidence ellipse, which indicates that they are more likely to attain a closer approximation to the correct eigenvalue on any given trial.

Focusing back on comparing Algorithms 2 and 3, we show results for a variety of values of m and σ_N^2 in Fig. 6.3. In Fig. 6.3(a), rather than looking at the error in the eigenvalues, we instead consider the Frobenius norm of the difference between the true and identified propagation matrices, $\|\tilde{A}_{\text{true}} - \tilde{A}_{\text{pred}}\|_F$. For very small noise, the correction makes little difference, since the random error is larger than the bias error. For larger values of noise, we observe that the error saturates when using standard DMD, which is due to the presence of the bias term identified in Sect. 6.2.2, which has a size independent of the number of samples, m . We note that the magnitude of this bias term is proportional to σ_N^2 , as predicted by Eq. (6.2.10). Evidence of this error saturation phenomena can also be seen in past studies of the effect of sensor noise on DMD [44, 164, 101]. After this bias term is corrected for, we see that the error decays proportional to $m^{-1/2}$ for all values of noise, as predicted from the analysis in Appendix 1. The more rapid decay in error with m for small numbers of samples seems to arise from the fact that the data has not yet completed one full period of oscillation. Fig. 6.3 shows the corrections to DMD made using both the sampled ($N_X N_X^*$) and theoretical ($m\sigma_N^2 I$) covariance matrices. Normally the sample noise covariance would not be known, and so we demonstrate here that the theoretical covariance achieves almost the same decrease in error. Fig. 6.3(b) shows that the ncDMD error curves collapse when the error is normalized by the standard deviation of noise, σ_N (note that we could also multiply the error by the SNR to get the same scaling).

Fig. 6.4 shows the performance of Algorithms 4 and 5 on the same data as Fig. 6.3. Again, we

DISTRIBUTION A: Distribution approved for public release.

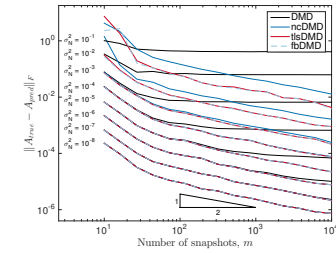


Figure 6.4: Error in the estimated propagation matrix \tilde{A} arising from performing DMD, ncDMD, fbDMD, and tIsDMD on noise-corrupted data generated from Eq. (6.3.1), for different values of m and σ_N^2 . The error is given as $\|\tilde{A}_{\text{true}} - \tilde{A}_{\text{pred}}\|_F$, and is averaged over 100 trials for each m and σ_N^2

find that both of these algorithms can prevent the error saturation present in standard DMD, and indeed can perform noticeably better than Algorithm 3 for larger noise levels. Algorithms 3-5 all appear to exhibit the same asymptotic behavior as the number of snapshots, m , increases, with the error decreasing proportional to $m^{-1/2}$.

A common means to mitigate the effect of noisy data is to collect multiple time-series of data, and process this in such a way to improve the results over just using one data set. One can ask the question if it is better to concatenate the snapshots of data from each time series and apply DMD to this collection, or to apply DMD to phase-averaged data. Our results suggest that the latter option is preferable if using standard DMD, since adding additional pairs of snapshots will not decrease the error beyond a certain level, due to this bias saturation at large m . If we are using ncDMD, fbDMD, or tIsDMD, however, then we should get the same scalings regardless of which option is chosen, since in both cases the error should be proportional to $p^{-1/2}$, where p is the number of trials of data collected.

6.3.2 A periodic linear system with a high-dimensional state of observables

This example considered in Sect. 6.3.1 has $m \gg n$, which is atypical of many fluids systems for which DMD is used. To consider the case where the size of the state n is larger than the number of snapshots m , we expand the state of our system to include time-shifts of the data. In this sense, we have new observables given by

$$\mathbf{z}_k = \begin{bmatrix} \mathbf{x}_k \\ \mathbf{x}_{k-1} \\ \vdots \\ \mathbf{x}_{k-q} \end{bmatrix}, \quad (6.3.2)$$

with the size of the state $n = 2(q+1)$. This periodic system can equivalently be viewed as a traveling wave, which is now observed over a larger spatial domain. Similar data (but with a non-zero growth rate) was considered in [44] and [164]. Since the dynamics are still only two-dimensional despite the higher dimensional state, we use only the first two POD modes of the data to identify

DISTRIBUTION A: Distribution approved for public release.

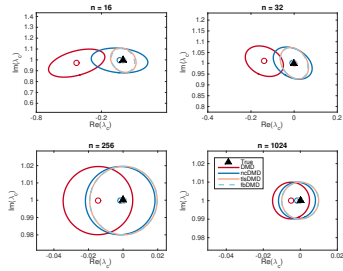


Figure 6.5: Mean and 95% confidence ellipses of continuous-time eigenvalues identified by applying regular DMD (Algorithm 2), noise-corrected DMD (Algorithm 3), forward-backward DMD (Algorithm 4) and total least-squares DMD (Algorithm 5) on 1000 trials of noisy data generated by Eq. (6.3.1), and observed as in Eq. (6.3.2). Here the number of snapshots m is fixed to be 50, $\Delta t = 0.1$, and $\sigma_V^2 = 0.1$. Only one of the complex conjugate pair of eigenvalues is shown

a 2×2 propagation matrix \tilde{A} . The next section will examine alternative means of performing this dimensionality reduction.

Fig. 6.5 shows the statistical results (in terms of DMD eigenvalues) of performing variants of DMD on such data, using $m = 50$ and a range of snapshot sizes, n . We find that a bias exists for regular DMD, but the magnitude of this bias decreases as the size of each snapshot increases (note that the scale between subplots changes, though the aspect ratio remains the same). We find that Algorithms 3–5 all outperform regular DMD in terms of giving mean (expected) eigenvalues that are closer to the true value. For small state sizes, Algorithms 4 and 5 also give a smaller confidence ellipse, though this is not observed for larger state sizes. As the size of the state increases, the bias component of the error of DMD (evidenced by the difference between the true and mean identified eigenvalue) becomes smaller relative to the random component of the error (indicated by the size of the confidence ellipse). This means that the modifications to DMD presented in Algorithms 3–5 give the largest improvement when the size of the state is small, due to the fact that in this regime the bias component of error is larger than the random component. Note that these conclusions may be predicted from the scaling laws given in Eqs. (6.5.2) and (6.5.5). Moreover, one can verify that as the size of the state (n) increases, the size of the ellipses decrease proportional to $n^{-1/2}$.

6.3.3 Comparison to other modified DMD algorithms

Without any modification, applying DMD on noisy data will give $\min(m, n)$ eigenvalue-mode pairs, many of which may be mostly or entirely due to noise, particularly if the underlying dynamics are low-dimensional. For this reason, a number of modifications of DMD that aim to identify a small number of dynamically important modes have been developed. The most simple means of reducing the dimension of the data is to simply project onto a reduced number of POD modes, which is explicitly mentioned as an optional step in Algorithm 2. This projection step was also used within Algorithms 3–5 in Sect. 6.3.2. A number of alternative means to obtain a small number of dynamic modes from DMD-type algorithms have been proposed, as briefly mentioned in Sect. 6.1. These

DISTRIBUTION A: Distribution approved for public release.

variants all start with the observation that standard DMD can be formulated within an optimization framework, in the sense that it identifies a least-squares or minimum-norm propagation matrix for a given data set. [27] proposes a modification termed *optimized* DMD that seeks to find optimal low-rank dynamics that best matches a sequential time-series of data. While the fact that this method optimizes over the entire time-sequence of data rather than just pairwise snapshots should increase its robustness to noise, the non-convexity of the optimization potentially limits its utility. Optimal Mode Decomposition (OMD, [56, 164]) finds an optimal low-dimensional subspace on which the identified dynamics reside, rather than assuming that this subspace is simply the most energetic POD modes. This approach was shown to give an improvement on the DMD eigenvalues obtained for noisy data in [164]. Sparsity-promoting DMD (spDMD, [71]) adds an l_1 regularization term that penalizes the number of DMD modes with non-zero coefficients in the approximation of the time-series of data.

This section will compare OMD and spDMD with the algorithms presented in the present work. Of the algorithms presented here, we will focus on fbDMD (Algorithm 4), which was found to perform equally well as tlsDMD, and better than ncDMD, in Sects. 6.3.1 and 6.3.2. Fig. 6.6 shows identified eigenvalue statistics (mean and confidence ellipses) for each of these algorithms, using the same data as that for Fig. 6.5. We observe that OMD gives a more accurate mean eigenvalue than DMD, and a confidence ellipse of approximately the same size. spDMD gives a mean identified eigenvalue that is closer again to the mean, although the variance in the eigenvalues identified for each trial is larger. We note that spDMD occasionally produced erroneous results, which were excluded as outliers from the statistical analysis. This highlights an important advantage to the modifications to DMD presented here - the algorithms are given in closed form, and do not rely on an appropriate selection of parameters and tolerances that are most likely required for an optimization procedure. In all of the cases, fbDMD (and tlsDMD, which is not shown but barely distinguishable from fbDMD) gives the best estimate of the true eigenvalue.

While these results suggest that fbDMD/tlsDMD is more accurate than OMD and spDMD, we must remember that the results from one data set do not show the global superiority of any given algorithm. Indeed, one could most likely find data sets for which any given algorithm is superior (by some chosen metric) to others. We conclude this section by noting that it should be possible to combine the optimization procedures presented in [27], [164], and [71]) with the modifications to DMD presented here. Indeed, a simple means to do this might be to modify Algorithm 4 so that the results of applying a given algorithm forwards and backwards in time are geometrically averaged, as in Eq. (6.2.15).

6.3.4 Identifying hidden dynamics

The systems considered in Sects. 6.3.1 and 6.3.2 could be considered “easy” in the sense that the dominant dynamics are simple, and of consistently larger magnitude than the noise. Indeed, it is not difficult to qualitatively identify such dynamics by eye from simply looking at some visualization of the data. A more difficult case occurs when some of the dynamics are of low magnitude and/or are quickly decaying, and thus might quickly be lost among the noise in the measurements. A major benefit of data processing techniques such as DMD is the ability to identify dynamics that might otherwise remain hidden. With this in mind, we now consider a superposition of two sinusoidal signals that are traveling across a spatial domain in time, with the amplitude of one mode growing, and the other decaying:

$$f(x, t) = \sin(k_1 x - \omega_1 t) e^{\gamma_1 t} + \sin(k_2 x - \omega_2 t) e^{-\gamma_2 t} + n_\sigma(x, t), \quad (6.3.3)$$

DISTRIBUTION A: Distribution approved for public release.

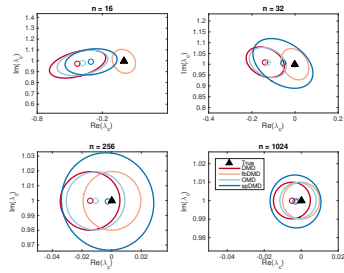


Figure 6.6: Mean and 95% confidence ellipses of continuous-time eigenvalues identified by applying regular DMD (Algorithm 2), forward-backward DMD (Algorithm 5), OMD and spDMD for noisy data generated from 1000 trials of data generated by Eq. (6.3.1), and observed as in Eq. (6.3.2). Here the number of snapshots m is fixed to be 50, $\Delta t = 0.1$, and $\sigma_N^2 = 0.1$. Only one of the complex conjugate pair of eigenvalues is shown

where we set $k_1 = 1$, $\omega_1 = 1$, $\gamma_1 = 1$, $k_2 = 0.4$, $\omega_2 = 3.7$ and $\gamma_2 = -0.2$. We thus have the superposition of a growing, traveling wave, and a decaying signal that is quickly hidden by the unstable dynamics. The four continuous-time eigenvalues of this data are $\gamma_1 \pm \omega_1$ and $\gamma_2 \pm \omega_2$. This data is again similar to that considered in [164] and [44], if we neglect the decaying dynamics. Fig. 6.7 shows the data with white noise of standard deviation $\sigma = 0.5$. Fig. 6.8 shows the performance of various DMD-type algorithms in identifying one of the dominant eigenvalues ($1+i$) and one of the “hidden” eigenvalues ($-0.2+3.7i$). Mean eigenvalues and error ellipses are computed from 1000 different noise samples. Unsurprisingly, all methods are quite accurate at identifying the dominant eigenvalue, though the variants proposed in the present work show improvements in both the mean and scatter over the 1000 trials. In terms of the hidden eigenvalue, we observe that DMD (as well as OMD) estimates a decay rate that is almost double the true value. In contrast, all of ncDMD, fbDMD, and tlsDMD predict the eigenvalue accurately, with a reduction in the error of the mean eigenvalue between DMD and fbDMD (for example) of 88%. In addition, we note that the scatter in the identified hidden eigenvalue across the trials is smaller for fbDMD and tlsDMD (as indicated by smaller confidence ellipses).

6.3.5 Differentiating between process and sensor noise

This section will primarily address the issue of comparing and distinguishing between the effects of process and sensor noise. We consider the Stuart-Landau equation, which has been used as a model for the transient and periodic dynamics of flow past a cylinder in the vortex shedding regime [95, 7]. In discrete time, we can express this system in polar coordinates by

$$\begin{aligned} r_{k+1} &= r_k + dt(\mu r_k - r_k^3 + n_r), \\ \theta_{k+1} &= \theta_k + dt(\gamma - \beta r_k^2 + \frac{n_\theta}{r_k}), \end{aligned} \tag{6.3.4}$$

DISTRIBUTION A: Distribution approved for public release.

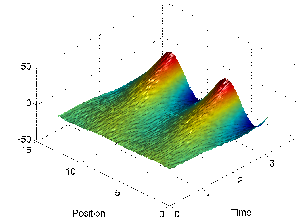


Figure 6.7: Visualization of data generated by Eq. (6.3.3), with $k_1 = 1$, $\omega_1 = 1$, $\gamma_1 = 1$, $k_2 = 0.4$, $\omega_2 = 3.7$, $\gamma_2 = -0.2$, and $\sigma = 0.5$

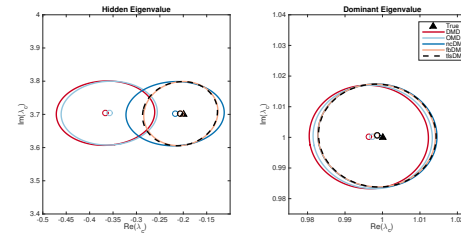


Figure 6.8: Mean and 95% confidence ellipses of continuous-time eigenvalues identified by applying regular DMD (Algorithm 2), OMD, noise-corrected DMD (Algorithm 3), forward-backward DMD (Algorithm 4) and total least-squares DMD (Algorithm 5) to 1000 trials of noisy data generated by Eq. (6.3.3), with $k_1 = 1$, $\omega_1 = 1$, $\gamma_1 = 1$, $k_2 = 0.4$, $\omega_2 = 3.7$, $\gamma_2 = -0.2$, and $\sigma = 0.5$

DISTRIBUTION A: Distribution approved for public release.

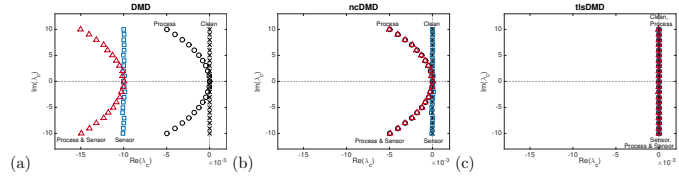


Figure 6.9: Eigenvalues identified using (a) DMD, (b) ncDMD, and (c) tIsDMD for the Stuart-Landau equation (Eq. (6.3.4)), with 100,000 snapshots of data from Eq. (6.3.5), with $r_0 = 1$, $\mu = 1$, $\gamma = 1$, $\beta = 0$, and $dt = 0.01$. Data with sensor noise, process noise, neither and both are considered, with noise levels for process and sensor noise being $\sigma_p^2 = 0.01$ and $\sigma_N^2 = 10^{-4}$ respectively. Note that in the absence of sensor noise, DMD and ncDMD are identical

where we have included process noise terms n_r and n_θ , which are assumed to be independent in time, and sampled from separate zero-mean Gaussian distributions with variance σ_p^2 . We take as our data snapshots of the form

$$\mathbf{x}_k = [e^{-Ji\theta_k} \ e^{(-J+1)i\theta_k} \ \dots \ e^{Ji\theta_k}]^T, \quad (6.3.5)$$

for some integer J . We may add sensor noise to this data as in previous sections. For $\mu > 0$, Eq. (6.3.4) contains a stable limit cycle at $r = \sqrt{\mu}$, with period $2\pi/(\gamma - \beta\mu)$. Starting on the limit cycle, we consider data with process noise, sensor noise, neither, and both. Without any noise, the eigenvalues identified from this data will lie upon the imaginary axis, at locations given by $\lambda_c = ij(\gamma - \mu\beta)$. Process noise acts to perturb the system from its limit cycle, which ultimately leads to phase diffusion, and a “bending” of the eigenvalues such that they instead lie on a parabola. The behavior of this system with process noise is described more extensively in [8]. Fig. 6.9 shows the results of applying variants of DMD on data generated by Eq. (6.3.4) with $\mu = 1$, $\gamma = 1$, $\beta = 0$, and $dt = 0.01$, with data collected using Eq. (6.3.5) with $J = 10$. Applying DMD on noise-free data gives eigenvalues along the imaginary axis, while data from the system with process noise gives a parabola of eigenvalues, as expected. For data collected using Eq. (6.3.5), each data channel will be orthogonal in time, and will contain the same energy. As a result, sensor noise will act to shift all identified eigenvalues into the left half plane by the same amount, as observed in Fig. 6.9(a). Fig. 6.9(b) shows that applying ncDMD accurately corrects for this shift, for the system with and without process noise. This shows that it is possible to distinguish between the effects of these two forms of noise, given only an estimate of the magnitude of the sensor noise. That is, we are able to eliminate the effects of the noise that is due to imperfections in our observations, while retaining the effects of actual disturbances to the system. Fig. 6.9(c) shows that tIsDMD corrects for the effects of both process and sensor noise, which is desirable if one wishes to recover the dynamics of the noise-free system. The results for fbDMD are not shown, but were very similar to those for tIsDMD. The ability of tIsDMD and fbDMD on process noise is not surprising, since they treat X and Y in a symmetric manner, and thus consider phase diffusion both forwards and backwards in time.

DISTRIBUTION A: Distribution approved for public release.

6.4 Results with numerical and experimental data

Having analyzed the performance of the various proposed modifications of DMD on synthetic data sets, we now turn our attention to data obtained from fluids simulations and experiments. We will focus on the canonical case of the unsteady wake of a circular cylinder exhibiting periodic vortex shedding. In Sect. 6.4.1 we present results from data obtained from a two-dimensional direct numerical simulation, while Sect. 6.4.2 considers data obtained from PIV measurements in a water channel.

6.4.1 Cylinder wake: simulation data

We use an immersed boundary projection method [139, 34], with a domain consisting of a series of nested grids, with the finest grid enclosing the body, and each successive grid twice as large as the previous. The finest grid consists of uniformly spaced points with grid spacing equal to $0.02D$ (where D is the cylinder diameter), extending $2D$ upstream and $4D$ downstream of the center of the cylinder, and spanning $4D$ in the direction normal to the flow. Each successively larger grid contains the same number of grid points, with twice the grid spacing as the previous grid. The coarsest grid spans $24D$ in the streamwise direction and $16D$ in the normal direction. Uniform boundary conditions are used to first solve the Navier-Stokes equations on the largest grid, with each smaller grid using the next larger grid for boundary conditions. The numerical scheme uses a 3rd order Runge-Kutta time stepper, with a time step of $0.01D/U_\infty$, where U_∞ and D are the freestream velocity and cylinder diameter, respectively. The Reynolds number $Re = \frac{U_\infty D}{\nu}$ was set to be 100, where ν is the kinematic viscosity. This Reynolds number is above that for which the wake is stable (47, [107]), and below that for which 3-dimensional instabilities emerge (approximately 194, [163]). At this Reynolds Number, the wake is hence unstable, and approaches a single periodic limit cycle characterized by a von-Kármán vortex street in the wake. The data to be analyzed was taken from 234 snapshots of the vorticity field, spaced $0.1D/U$ time units apart. This corresponds to approximately 4 complete periods of vortex shedding. We truncate the data to only consider first 15 POD modes. These first 15 POD modes contain 99.99% of the total energy of the clean data, and 92.96% of the total energy of the data after the addition of Gaussian white noise with standard deviation $\sigma = 0.2U/D$. Thus it is almost entirely noise that is truncated for the noisy data.

Fig. 6.10 shows results from applying various variants of DMD to such data. Though not shown, the results of applying tIsDMD were visually indistinguishable as using fbDMD. Since we are artificially adding noise, we can compare the results using noisy data to those generated from the noise-free data. When applying regular DMD to noisy data, we observe significant errors in the growth rate associated with the highest-frequency eigenvalues (Fig. 6.10(a)). For an oscillatory system such as this, the DMD eigenmodes are very similar to the POD modes, with a DMD mode corresponding to $\lambda_c \approx 0$ that is almost the mean flow, and the modes associated with conjugate pairs of DMD eigenvalues corresponding to pairs of POD modes with equal energy, see [27] for further discussion of this phenomenon. This means that the observed measured eigenvalues are in line with the analysis given in Sect. 6.2.2 and Appendix 1, since the lower energy POD modes oscillate the most. We can see the effect of this error in Fig. 6.10(b), which shows the prediction of a number of POD coefficients as evolved by the identified system, starting from the true initial condition. The dominant, low frequency POD modes are accurately predicted, but the higher “harmonics” are erroneously predicted to decay when using regular DMD. ncDMD improves the performance marginally, while fbDMD and tIsDMD both almost completely remove the erroneous

DISTRIBUTION A: Distribution approved for public release.

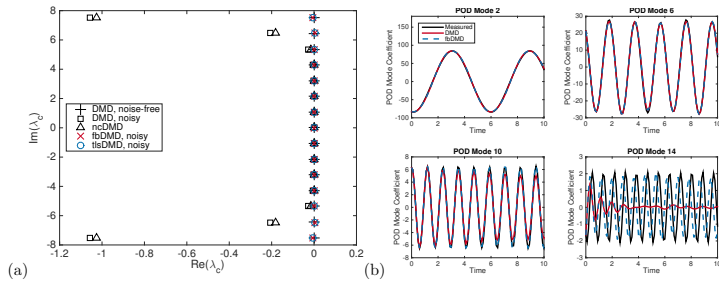


Figure 6.10: (a) Eigenvalues and (b) POD coefficients identified from applying DMD, ncDMD, fbDMD, and tsDMD to DNS vorticity data from a cylinder wake at $Re = 100$. Noisy data was corrupted with Gaussian white noise with $\sigma = 0.2U/D$

decay of the high-frequency modes.

As well as considering eigenvalues, we also validate in Fig. 6.11 that the modifications of DMD do not adversely affect the identified DMD modes. This is shown both visually in Fig. 6.11(a), and quantitatively in Fig. 6.11(b), where we give the inner product $\langle \phi_{i, \text{noisy}}, \phi_{i, \text{clean}} \rangle$ of the i^{th} modes identified from clean and noisy data, where we have pre-scaled the modes to be of unit norm. We enumerate the modes by the imaginary component of the associated eigenvalue, with mode 0 corresponding to the eigenvalue on the real axis. For modes that come in complex conjugate pairs, we arbitrarily consider those with positive imaginary component. We see that both fbDMD and tsDMD marginally outperform regular DMD, in terms of identifying modes that are at least as close to those identified from noise-free data. The decrease in the inner product as the mode number increases is indicative of noise being more significant in higher-frequency modes, which contain less energy.

6.4.2 Cylinder wake: experimental data

We now turn our attention to data acquired from water channel experiment. An anodized aluminum cylinder of diameter $D = 9.5 \text{ mm}$ and length $L = 260 \text{ mm}$ was immersed in a recirculating, free-surface water channel with freestream velocity $U_\infty = 4.35 \text{ cm/s}$. This gives a Reynolds number $Re = \frac{DU_\infty}{\nu} = 413$. Further details of the experimental setup and methodology are provided in [148]. We apply variants of DMD to 500 snapshots from a vorticity field of size 135×80 . Fig. 6.12 shows the identified eigenvalues and the predicted POD coefficients from the models identified from DMD and tsDMD. As in Sect. 6.4.1, we first project onto the 15 most energetic POD modes. Note that some eigenvalues (typically quickly decaying) are outside the range of the plot. As was the case with DNS data, we observe that DMD gives eigenvalues that are further into the left half plane than and of the other methods. This manifests in the erroneous prediction of decaying POD coefficients (Fig. 6.12(b)), particularly for modes that are less energetic, and more rapidly oscillating. We thus conclude that more accurate low-dimensional models for the experimental results can be achieved by using tsDMD. We note that this improvement can be attained without explicit knowledge of

DISTRIBUTION A: Distribution approved for public release.

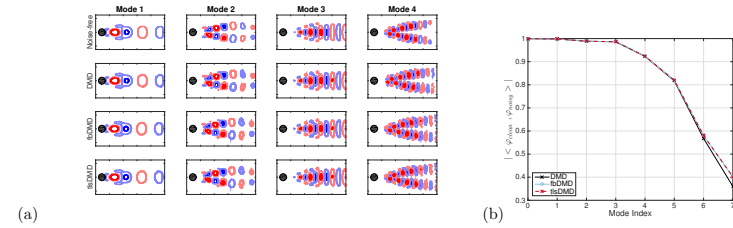


Figure 6.11: (a) A subset of the DMD modes (real components) computed from applying various variants of DMD to DNS data of flow around a cylinder. (b) Inner product between (normalized) clean modes, and modes obtained from noisy data (with $\sigma_N = 0.2U_\infty/D$)

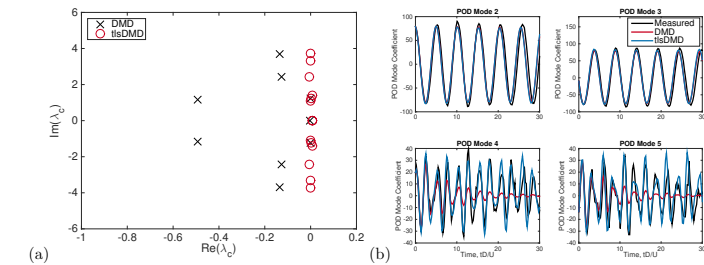


Figure 6.12: (a) Eigenvalues and (b) POD coefficients identified from applying DMD and tsDMD to experimental vorticity data

the process and sensor noise characteristics.

6.5 Discussion and conclusions

It was shown in Sect. 6.2 that simple linear algebraic considerations can allow us to derive an estimate for the bias that exists in all standard formulations of DMD. This subsequently led to the formulation of the three modified algorithms that we suggest can be used to eliminate this bias. Sect. 6.3 showed that this predicted bias is indeed present in the results of DMD. Directly correcting for this bias term (Algorithm 3, ncDMD) was shown to almost completely eliminate this bias. While this modification demonstrates that our characterization of the dominant effects of noise was accurate, its usefulness is limited by the fact that it requires an accurate estimate of the noise covariance. Additionally, the presence of a Σ^{-2} term in correction factor used in ncDMD makes this computation unsuitable for cases with small singular values that are not truncated. On the other hand, the correction factor in Algorithm 3 may be applied to existing DMD results

DISTRIBUTION A: Distribution approved for public release.

with minimal computational effort. Algorithms 4 (fbDMD) and 5 (tlsDMD), which do not require knowledge of the noise characteristics, were also found to correct for the bias, and also were able to reduce the random error across many noise realizations (as seen by smaller associated confidence ellipses in Fig. 6.2, for example). Furthermore, fbDMD and tlsDMD were found in Sect. 6.3.5 to also compensate for the effect of process noise. This feature could be desirable or undesirable, depending on the purpose for which DMD is being applied. Note that this is also consistent for the findings in Sect. 6.4.2, where for a notionally periodic system, tlsDMD was found to give eigenvalues very close to the imaginary axis, despite (presumably) the presence of both sensor and process noise.

In practice, the examples examined in Sects. 6.3.4, 6.4.1 and 6.4.2 suggest an overarching principle: while regular DMD can be accurate for identifying dominant dynamics that have much larger amplitudes than the noise in the data, accurate identification of the eigenvalues associated with lower amplitude modes (and in particular, their real components) can be significantly improved when using the modified DMD algorithms presented here. Conversely, if one is primarily concerned with the identification of modes and their frequencies of oscillation, and less concerned with accurate identification of growth/decay rates, then the effect of sensor noise is comparatively minimal, and subsequently the choice of DMD algorithm is less important.

Fundamentally, the bias in DMD arises because the algorithm is essentially a least-squares algorithm, which is designed for cases where the “independent” variable (which in DMD takes the form of the data X) is known accurately, and the “dependent” variable Y contains the noise/error. In reality, since X and Y should both be affected by noise, minimizing the error in both the X and Y “directions” can allow for a more accurate answer to be obtained. One drawback of tlsDMD is that it requires taking the SVD of a larger matrix. Note that for cases where $n > m$ (i.e., the size of each snapshot is larger than the number of snapshots) and there is no truncation of POD modes corresponding to small singular values, DMD gives the minimum Frobenius norm (of A) solution to $AX = Y$. In this case, in principle neither fbDMD or tlsDMD should yield any improvements. In reality, however, if there is noise in the data, then we do not necessarily want an exact fit to the data, but rather an unbiased estimate of the noise-free dynamics. We may obtain this by truncating POD modes that are deemed to be mostly noise, and use some variant of DMD to identify the remaining dynamics. tlsDMD and fbDMD give very similar results, which suggests that fbDMD can be viewed as a computationally cheaper alternative to approximating the results of tlsDMD. Note that while fbDMD is often computationally cheaper, it relies on being able to invert the matrix B_m , which might be an ill-conditioned operation for some data.

In Sect. 6.3.3, we compared the variants presented here with two recent optimization algorithms that have been proposed. The results show our algorithms outperforming both sparsity promoting DMD and OMD. Note that since these algorithms are not in closed form, but instead contain optimization procedures, the results depend somewhat on the specification of the relevant optimization parameters. In this comparison, our use of Algorithms 3-5 relied upon the projection onto a low dimensional subspace before applying DMD-type algorithms. We particularly note that the tlsDMD algorithm proposed here is slightly different from that given in [63] due to this POD projection, which we found empirically to give improved results. We suggest that this is because the initial truncation of low-energy POD modes has a filtering effect that better isolates the true dynamics, at least for the datasets considered here. One could imagine, however, that in certain cases this projection could lead to significant degradation of results. For example, where the dynamically important modes are highly dissimilar to the dominant POD modes, the flexibility for the projection basis to be modified could be particularly advantageous. In such cases, sparsity promoting DMD or OMD could give more favorable results. In general, it is relatively common in system identification to use a subspace that is larger than the dimension of the underlying dynamics, and then later truncate to obtain a reduced order model of an appropriate size/rank. This can be particularly

DISTRIBUTION A: Distribution approved for public release.

important when the dealing with specific system inputs and outputs [112]. [73] discuss a number of ways in which true dynamic modes can be distinguished for noisy modes, in the context of the eigensystem realization algorithm. [149] further discusses how DMD modes can be scaled, from which appropriate modes can be chosen. The spDMD algorithm in [71] essentially automates this procedure, and comes with the additional potential advantage of not requiring a-priori knowledge of the dimension of the reduced order dynamics to be identified. Note that it is also possible to combine the modifications to DMD proposed here with the OMD and spDMD optimization procedures, which could result in further improvements in some circumstances.

Though we used a large number of trials when testing our results on synthetic data in order to obtain statistically meaningful findings, in reality one would most likely not have this luxury with real data. In this case, it is important to understand for the size and quality of the data to be analyzed, both the best algorithm to use, and the amount of confidence that should be had in the results of the chosen algorithm.

While this work has been motivated by and has largely focused on sensor noise (that is, noise which only affects measurements, and not the system dynamics), the characterization and removal of process noise (i.e., disturbances to the system states) is entirely another matter. Interestingly, the effect of process noise was identified analytically in [8] to be a parabolic decay in the growth rate of identified eigenvalues with increasing frequency. It turns out that a similar effect is observed here for the case of measurement noise. Isolating sensor noise from process noise (especially with limited prior information about the statistics of either) is an important and challenging task, particularly when dealing with more complex, turbulent flows, where the true dynamics exist on a wide range of spatial and temporal scales. The fact that DMD, ncDMD and tlsDMD/fbDMD each perform differently on these different forms of noise could itself be an important tool to this end.

Particularly in experimental data, users might typically preprocess data in a number of ways before considering applying DMD-type algorithms. It could be advantageous to investigate precisely how various averaging and smoothing operations affect the subsequent analysis of dynamics, and subsequently whether such post-processing and analysis can be achieved through a single algorithm.

Ultimately, having a larger selection of possible algorithms should be of benefit to researchers who desire the dynamical information that DMD-type algorithms can provide, who can choose based on the size of the data, amount of noise present, required accuracy of the results, and amount of computational resources available. One of the major advantages of DMD (and related algorithms) advocated in [126] is the fact that it requires only direct data measurements, without needing knowledge of any underlying system matrix, thus making it well suited to use on experimentally acquired data. Inevitably, however, data from experiments is always affected to some extent by noise. It is thus important to properly understand and quantify how noise can influence the results of DMD. Conversely, the quest for high quality data can often require large investments of both time and money. Formulating algorithms that are more robust to noisy data can be a cheaper alternative to obtain results of sufficient accuracy. As it becomes easier to generate and store increasingly large datasets, it is also important to recognize that simply feeding larger quantities of data (e.g., more snapshots) into a given algorithm does not guarantee desired improvements in the accuracy of their outputs, as illustrated in Figures 6.3 and 6.4.

The problem that fluid dynamicists face in extracting tractable information from large datasets is not unique to fluids, and rather transcends a wide variety of fields of study (although other fields are often not afforded the luxury of knowing the underlying differential equations). It is valuable to recognize and make use of the parallels in previous and current developments across a wide range of fields. We likewise hope that other areas can benefit from the work that is motivated by the desire to understand how fluids flow.

DISTRIBUTION A: Distribution approved for public release.

Appendix 1: Quantifying the size of the bias in DMD

We seek to quantify the magnitude of this bias present in DMD that was derived in Sect. 6.2.2, subject to certain simplifying assumptions on the nature of the data and noise. If the noise is uniform, and spatially and temporally independent, then $\mathbb{E}(\tilde{N}_X \tilde{N}_X^*) = \mathbb{E}(U^* N_X N_X^* U) = U^* m \sigma_N^2 U = m \sigma_N^2 I$, where σ_N^2 is the variance of each independent component of the noise matrix. Furthermore, if we assume that we are projecting onto the POD modes of the clean data, then $(\tilde{X} \tilde{X}^*) = \Sigma^2$, where $U \Sigma V^*$ is the singular value decomposition of X . Thus with these assumptions, Eq. (6.2.6) can be simplified to give

$$\mathbb{E}(\tilde{A}_m) = \tilde{A}(I - m \sigma_N^2 \Sigma^{-2}). \quad (6.5.1)$$

The (diagonal) entries Σ_i^2 of Σ^2 have the interpretation of being the energy content of the i^{th} POD mode. We then should expect that $\Sigma_i^2 \sim m n q_i \sigma_X^2$, where σ_X^2 is the RMS value of the elements in the data matrix X , and $q_i = \frac{\Sigma_i^2}{\text{Trace}(\Sigma^2)}$ is the proportion of the total energy of the system contained in the i^{th} POD mode. For this scaling, we make the assumption that adding/removing rows and columns of data (i.e., varying m and n) does not affect either σ_X or q_i . The bias term $m \sigma_N^2 \Sigma^{-2}$ is a diagonal matrix whose i^{th} entry has a size $(e_b)_i$ proportional to

$$(e_b)_i \sim \frac{1}{n q_i SNR^2}, \quad (6.5.2)$$

where SNR is the signal-to-noise ratio. Thus sensor noise has the effect of reducing the diagonal entries of the computed \tilde{A}_m matrix by a multiplicative factor of $1 - \frac{\sigma_N^2}{n q_i \sigma_X^2}$, which means that POD coefficients are predicted to decay more rapidly than they actually do. This effect is most pronounced for lower energy modes, for which the q_i is smaller. We thus expect to identify with DMD (continuous-time) eigenvalues that are further into the left half plane than they should be (or would be if we applied DMD to noise-free data). [44] argues in the case of periodic data that the growth rate of the eigenvalues should typically be the most challenging to identify, since there are a range of pre-existing methods that can identify frequencies. Here we have argued that it is precisely this growth rate that is most affected by noise. Importantly, the amount of bias is independent of m , which suggests that the bias component of the error will be particularly dominant when we have a large number of low-dimensional snapshots. Importantly, this suggests that one cannot always effectively reduce the effect of noise by simply using more snapshots of data, since the bias error will eventually become the dominant error.

While we can now quantify the magnitude of the bias in DMD, we do not as yet know how it compares to the random component of the error that would arise from a given realization of noise. To do this, we will estimate the typical size of the variance of individual entries of \tilde{A} , using the standard definition

$$\text{var} [\tilde{A}_{ij}] = \mathbb{E} \left\{ \left((\tilde{Y}_m \tilde{X}_m^+)_{ij} - \mathbb{E} [(\tilde{Y}_m \tilde{X}_m^+)_{ij}] \right) \left((\tilde{Y}_m \tilde{X}_m^+)_{ij} - \mathbb{E} [(\tilde{Y}_m \tilde{X}_m^+)_{ij}] \right) \right\}. \quad (6.5.3)$$

Referring back to Eq. (6.2.3), if we exclude terms that are quadratic or higher in noise, and assume that the noise covariance matrix is sufficiently close to its expected value, we find that

$$\begin{aligned} (\tilde{Y}_m \tilde{X}_m^+) - \mathbb{E} [(\tilde{Y}_m \tilde{X}_m^+)] &= (\tilde{Y} + \tilde{N}_Y)(\tilde{X} + \tilde{N}_X)(\tilde{X} \tilde{X}^* + \tilde{X} \tilde{N}_X^* + \tilde{N}_X \tilde{X}^* + \tilde{N}_X \tilde{N}_X^*)^{-1} - \tilde{Y} \tilde{X}^+ - \mathbb{E}(\tilde{N}_X \tilde{N}_X^*) \Sigma^{-2} \\ &= [\tilde{Y} \tilde{X}^+ (\tilde{X} \tilde{N}_X^* + \tilde{N}_X \tilde{X}^*) + \tilde{N}_Y \tilde{X}^* + \tilde{Y} \tilde{N}_X^*] \Sigma^{-2}. \end{aligned}$$

Elements of the terms $\tilde{X} \tilde{N}_X^*$, $\tilde{N}_X \tilde{X}^*$, $\tilde{N}_Y \tilde{X}^*$, and $\tilde{Y} \tilde{N}_X^*$ are uncorrelated sums over m random terms, with each term in the sum having variance $n q_i \sigma_X^2 \sigma_N^2$ where as before q_i is the energy fraction

DISTRIBUTION A: Distribution approved for public release.

in the i^{th} POD mode. This means that the sum will have variance $m n q_i \sigma_X^2 \sigma_N^2$. Assuming that $\tilde{Y} \tilde{X}^+ (= \tilde{A})$ does not greatly change the magnitude of quantities that it multiplies, and assuming that q_i remains constant when varying m and n , this means that we find that

$$\text{var} [\tilde{A}_{ij}] \sim \frac{\sigma_N^2}{m n \sigma_X^2}. \quad (6.5.4)$$

Thus the expected size of the random error in applying DMD to noisy data is

$$e_r \sim \frac{1}{m^{1/2} n^{1/2} SNR}. \quad (6.5.5)$$

Comparing Eq. (6.5.5) with Eq. (6.5.2), we propose that the bias in DMD will be the dominant source of error whenever

$$m^{1/2} SNR > n^{1/2}.$$

DISTRIBUTION A: Distribution approved for public release.

Bibliography

- [1] Mukund Acharya and Metwally H Metwally. Unsteady pressure field and vorticity production over a pitching airfoil. *AIAA journal*, 30(2):403–411, 1992.
- [2] S. Ahuja and C. W. Rowley. Feedback control of unstable steady states of flow past a flat plate using reduced-order estimators. *Journal of Fluid Mechanics*, 645:447–478, 2010.
- [3] Espen Åkervik, Luca Brandt, Dan S Henningson, Jérôme Hœpfner, Olaf Marxen, and Philipp Schlatter. Steady solutions of the Navier-Stokes equations by selective frequency damping. *Physics of Fluids*, 18(6):068102, 2006.
- [4] Md Mahbub Alam, Y Zhou, HX Yang, H Guo, and J Mi. The ultra-low reynolds number airfoil wake. *Experiments in fluids*, 48(1):81–103, 2010.
- [5] Alessandro Alla and J Nathan Kutz. Nonlinear model order reduction via dynamic mode decomposition. *arXiv preprint arXiv:1602.05080*, 2016.
- [6] Nadine Aubry, Philip Holmes, John L Lumley, and Emily Stone. The dynamics of coherent structures in the wall region of a turbulent boundary layer. *Journal of Fluid Mechanics*, 192: 115–173, 1988.
- [7] Shervin Bagheri. Koopman-mode decomposition of the cylinder wake. *Journal of Fluid Mechanics*, 726:596–623, 2013.
- [8] Shervin Bagheri. Effects of weak noise on oscillating flows: Linking quality factor, floquet modes, and koopman spectrum. *Physics of Fluids (1994-present)*, 26(9):094104, 2014. doi: <http://dx.doi.org/10.1063/1.4895898>. URL <http://scitation.aip.org/content/aip/journal/pof2/26/9/10.1063/1.4895898>.
- [9] Zhidong Bai and Jack W Silverstein. *Spectral analysis of large dimensional random matrices*. Springer, 2009.
- [10] Yeon Sik Baik, Luis P Bernal, Kenneth Granlund, and Michael V Ol. Unsteady force generation and vortex dynamics of pitching and plunging aerofoils. *Journal of Fluid Mechanics*, 709:37–68, 2012.
- [11] M. Balajewicz and E. Dowell. Reduced-order modeling of flutter and limit-cycle oscillations using the sparse Volterra series. *Journal of Aircraft*, 49(6):1803–1812, 2012.
- [12] Maciej Balajewicz, Irina Tezaur, and Earl Dowell. Minimal subspace rotation on the Stiefel manifold for stabilization and enhancement of projection-based reduced order models for the compressible Navier-Stokes equations. *arXiv preprint arXiv:1504.06661*, 2015.

- [13] Maciej J Balajewicz, Earl H Dowell, and Bernd R Noack. Low-dimensional modelling of high-reynolds-number shear flows incorporating constraints from the Navier–Stokes equation. *Journal of Fluid Mechanics*, 729:285–308, 2013.
- [14] Maxime Barrault, Yvon Maday, Ngoc Cuong Nguyen, and Anthony T Patera. An ‘empirical interpolation’ method: application to efficient reduced-basis discretization of partial differential equations. *Comptes Rendus Mathématique*, 339(9):667–672, 2004.
- [15] Brandt A Belson, Onofrio Semeraro, Clarence W Rowley, and Dan S Henningson. Feedback control of instabilities in the two-dimensional blasius boundary layer: The role of sensors and actuators. *Physics of Fluids (1994-present)*, 25(5):054106, 2013.
- [16] Brandt A Belson, Jonathan H Tu, and Clarence W Rowley. A parallelized model reduction library. *ACM T. Math. Software*, 2013.
- [17] Gal Berkooz, Philip Holmes, and John L Lumley. The proper orthogonal decomposition in the analysis of turbulent flows. *Annual review of fluid mechanics*, 25(1):539–575, 1993.
- [18] J. Birch and M. Dickinson. Spanwise flow and the attachment of the leading-edge vortex on insect wings. *Nature*, 412:729–733, 2001.
- [19] J Borggaard, A Duggleby, A Hay, T Iliescu, and Z Wang. Reduced-order modeling of turbulent flows. In *Proceedings of MTNS*, 2008.
- [20] Philip L Boyland. Bifurcations of circle maps: Arnol’d tongues, bistability and rotation intervals. *Communications in Mathematical Physics*, 106(3):353–381, 1986.
- [21] S. L. Brunton and B. R. Noack. Closed-loop turbulence control: progress and challenges. *Applied Mechanics Reviews*, 67:050801, September 2015. doi: 10.1115/1.4031175.
- [22] Steven L Brunton, Clarence W Rowley, and David R Williams. Reduced-order unsteady aerodynamic models at low reynolds numbers. *Journal of Fluid Mechanics*, 724:203–233, 2013.
- [23] Steven L Brunton, Scott T M Dawson, and Clarence W Rowley. State-space model identification and feedback control of unsteady aerodynamic forces. *Journal of Fluids and Structures*, 50:253–270, 2014.
- [24] Steven L Brunton, Joshua L Proctor, and J Nathan Kutz. Discovering governing equations from data by sparse identification of nonlinear dynamical systems. *Proceedings of the National Academy of Sciences*, 113(15):3932–3937, 2016.
- [25] Randolph H Cabell, Michael A Kegerise, David E Cox, and Gary P Gibbs. Experimental feedback control of flow-induced cavity tones. *AIAA journal*, 44(8):1807–1816, 2006.
- [26] Saifon Chaturantabut and Danny C Sorensen. Nonlinear model reduction via discrete empirical interpolation. *SIAM Journal on Scientific Computing*, 32(5):2737–2764, 2010.
- [27] Kevin K Chen, Jonathan H Tu, and Clarence W Rowley. Variants of dynamic mode decomposition: boundary condition, Koopman, and Fourier analyses. *Journal of Nonlinear Science*, 22(6):887–915, 2011.
- [28] Xiuyuan Cheng and Amit Singer. The spectrum of random inner-product kernel matrices. *Random Matrices: Theory and Applications*, 2(04), 2013.

DISTRIBUTION A: Distribution approved for public release.

- [29] Jeesoon Choi, Tim Colonius, and David R Williams. Surging and plunging oscillations of an airfoil at low reynolds number. *Journal of Fluid Mechanics*, 763:237–253, 2015.
- [30] P Ghosh Choudhuri and DD Knight. Effects of compressibility, pitch rate, and reynolds number on unsteady incipient leading-edge boundary layer separation over a pitching airfoil. *Journal of Fluid Mechanics*, 308:195–217, 1996.
- [31] David James Cleaver, Zhijin Wang, Ismet Gursul, and MR Visbal. Lift enhancement by means of small-amplitude airfoil oscillations at low reynolds numbers. *AIAA journal*, 49(9):2018–2033, 2011.
- [32] David James Cleaver, Z Wang, and I Gursul. Bifurcating flows of plunging aerofoils at high strouhal numbers. *Journal of Fluid Mechanics*, 708:349–376, 2012.
- [33] DJ Cleaver, Zhijin Wang, and Ismet Gursul. Investigation of high-lift mechanisms for a flat-plate airfoil undergoing small-amplitude plunging oscillations. *AIAA journal*, 51(4):968–980, 2013.
- [34] T. Colonius and K. Taira. A fast immersed boundary method using a nullspace approach and multi-domain far-field boundary conditions. *Computer Methods in Applied Mechanics and Engineering*, 197:2131–2146, 2008.
- [35] Laurent Cordier, El Majd, B Abou, and J Favier. Calibration of pod reduced-order models using Tikhonov regularization. *International Journal for Numerical Methods in Fluids*, 63(2):269–296, 2010.
- [36] Laurent Cordier, Bernd R Noack, Gilles Tissot, Guillaume Lehnasch, Joël Delville, Maciej Balajewicz, Guillaume Daviller, and Robert K Niven. Identification strategies for model-based control. *Experiments in fluids*, 54(8):1–21, 2013.
- [37] J Dandois and PY Pamart. NARX modeling and extremum-seeking control of a separation. *AerospaceLab*, 6:1–13, 2013.
- [38] Scott T M Dawson, Steven L Brunton, and Clarence W Rowley. Nonlinear switched models for control of unsteady forces on a rapidly pitching airfoil. *66th Annual Meeting of the APS Division of Fluid Dynamics*, 2013.
- [39] Scott T M Dawson, Nicole K Schiavone, Clarence W Rowley, and David R Williams. A data-driven modeling framework for predicting forces and pressures on a rapidly pitching airfoil. In *45th AIAA Fluid Dynamics Conference*, page 2767, 2015.
- [40] Scott T. M. Dawson, Maziar S. Hemati, Matthew O. Williams, and Clarence W. Rowley. Characterizing and correcting for the effect of sensor noise in the dynamic mode decomposition. *Experiments in Fluids*, 57(42):1–19, 2016. ISSN 1432-1114. doi: 10.1007/s00348-016-2127-7. URL <http://dx.doi.org/10.1007/s00348-016-2127-7>.
- [41] AE Deane, IG Kevrekidis, G Em Karniadakis, and SA Orszag. Low-dimensional models for complex geometry flows: Application to grooved channels and circular cylinders. *Physics of Fluids A: Fluid Dynamics (1989-1993)*, 3(10):2337–2354, 1991.
- [42] Peter A Dewey, Antoine Carriou, and Alexander J Smits. On the relationship between efficiency and wake structure of a batoid-inspired oscillating fin. *Journal of Fluid Mechanics*, 691:245–266, 2012.

DISTRIBUTION A: Distribution approved for public release.

- [43] Daniel Duke, Damon Honnery, and Julio Soria. Experimental investigation of nonlinear instabilities in annular liquid sheets. *Journal of Fluid Mechanics*, 691:594–604, 2012.
- [44] Daniel Duke, Julio Soria, and Damon Honnery. An error analysis of the dynamic mode decomposition. *Experiments in fluids*, 52(2):529–542, 2012.
- [45] Reeve Dunne and Beverley J. McKeon. Dynamic stall on a pitching and surging airfoil. *Experiments in Fluids*, 56(8):1–15, 2015. ISSN 1432-1114. doi: 10.1007/s00348-015-2028-1. URL <http://dx.doi.org/10.1007/s00348-015-2028-1>.
- [46] Carl Eckart and Gale Young. The approximation of one matrix by another of lower rank. *Psychometrika*, 1(3):211–218, 1936.
- [47] J. D. Eldredge, C. Wang, and M. V. OL. A computational study of a canonical pitch-up, pitch-down wing maneuver. AIAA Paper 2009-3687, 39th Fluid Dynamics Conference, June 2009.
- [48] Brenden P Epps and Alexandra H Techet. An error threshold criterion for singular value decomposition modes extracted from piv data. *Experiments in fluids*, 48(2):355–367, 2010.
- [49] Thibault LB Flinois and Aimee S Morgans. Feedback control of unstable flows: a direct modelling approach using the eigensystem realisation algorithm. *Journal of Fluid Mechanics*, 793:41–78, 2016.
- [50] I. E. Garrick. On some reciprocal relations in the theory of nonstationary flows. Technical Report 629, NACA, 1938.
- [51] Morteza Gharib, Edmond Rambod, and Karim Shariff. A universal time scale for vortex ring formation. *Journal of Fluid Mechanics*, 360:121–140, 1998.
- [52] Bryan Glaz, Li Liu, and Peretz P Friedmann. Reduced-order nonlinear unsteady aerodynamic modeling using a surrogate-based recurrence framework. *AIAA journal*, 48(10):2418–2429, 2010.
- [53] Gene H Golub and Charles F Van Loan. *Matrix computations*, volume 3. JHU Press, 2012.
- [54] M. Goman and A. Khrabrov. State-space representation of aerodynamic characteristics of an aircraft at high angles of attack. *Journal of Aircraft*, 31(5):1109–1115, 1994.
- [55] F. Gómez, H. M. Blackburn, M. Rudman, B. J. McKeon, M. Luhar, R. Moarref, and A. S. Sharma. On the origin of frequency sparsity in direct numerical simulations of turbulent pipe flow. *Physics of Fluids*, 26(10):101703, 2014. doi: <http://dx.doi.org/10.1063/1.4900768>. URL <http://scitation.aip.org/content/aip/journal/pof2/26/10/10.1063/1.4900768>.
- [56] Paul J Goulet, Andrew Wynn, and David Pearson. Optimal mode decomposition for high dimensional systems. In *CDC*, pages 4965–4970, 2012.
- [57] Kenneth O Granlund, Michael V Ol, and Luis P Bernal. Unsteady pitching flat plates. *Journal of Fluid Mechanics*, 733:R5, 2013.
- [58] Muzio Grilli, Peter J Schmid, Stefan Hickel, and Nikolaus A Adams. Analysis of unsteady behaviour in shockwave turbulent boundary layer interaction. *Journal of Fluid Mechanics*, 700:16–28, 2012.

DISTRIBUTION A: Distribution approved for public release.

- [59] Jacob Grosek and J Nathan Kutz. Dynamic mode decomposition for real-time background/foreground separation in video. *arXiv preprint arXiv:1404.7592*, 2014.
- [60] M. S. Hemati, S. T. M. Dawson, and C. W. Rowley. Unsteady aerodynamic response modeling: A parameter-varying approach. *AIAA Aerospace Sciences Meeting*, 2015.
- [61] Maziar S Hemati, Jeff D Eldredge, and Jason L Speyer. Improving vortex models via optimal control theory. *Journal of Fluids and Structures*, 49:91–111, 2014.
- [62] Maziar S Hemati, Matthew O Williams, and Clarence W Rowley. Dynamic mode decomposition for large and streaming datasets. *Physics of Fluids (1994-present)*, 26(11):111701, 2014.
- [63] Maziar S Hemati, Clarence W Rowley, Eric A Deem, and Louis N Cattafesta. De-biasing the dynamic mode decomposition for applied Koopman spectral analysis. *arXiv preprint arXiv:1502.03854*, 2015.
- [64] Aurelien Hervé, Denis Sipp, Peter J Schmid, and Manuel Samuelides. A physics-based approach to flow control using system identification. *Journal of Fluid Mechanics*, 702:26–58, 2012.
- [65] B. L. Ho and R. E. Kalman. Effective construction of linear state-variable models from input/output data. In *Proceedings of the 3rd Annual Allerton Conference on Circuit and System Theory*, pages 449–459, 1965.
- [66] Philip Holmes, John L. Lumley, Gal Berkooz, and Clarence W. Rowley. *Turbulence, coherent structures, dynamical systems and symmetry*. Cambridge University Press, 2012.
- [67] Simon J Illingworth. Model-based control of vortex shedding at low reynolds numbers. *Theoretical and Computational Fluid Dynamics*, pages 1–20, 2016.
- [68] Simon J Illingworth, Aimee S Morgans, and Clarence W Rowley. Feedback control of flow resonances using balanced reduced-order models. *Journal of Sound and Vibration*, 330(8):1567–1581, 2011.
- [69] Simon J Illingworth, Aimee S Morgans, and Clarence W Rowley. Feedback control of cavity flow oscillations using simple linear models. *Journal of Fluid Mechanics*, 709:223–248, 2012.
- [70] Thierry Jardin and Yannick Bury. Lagrangian and spectral analysis of the forced flow past a circular cylinder using pulsed tangential jets. *Journal of Fluid Mechanics*, 696:285–300, 2012.
- [71] Mihailo R. Jovanović, Peter J. Schmid, and Joseph W. Nichols. Sparsity-promoting dynamic mode decomposition. *Physics of Fluids (1994-present)*, 26(2):024103, 2014. doi: <http://dx.doi.org/10.1063/1.4863670>. URL <http://scitation.aip.org/content/aip/journal/pof2/26/2/10.1063/1.4863670>.
- [72] J. N. Juang and R. S. Pappa. An eigensystem realization algorithm for modal parameter identification and model reduction. *Journal of Guidance, Control and Dynamics*, 8(5):620–627, 1985.
- [73] J-N Juang and Richard S Pappa. Effects of noise on modal parameters identified by the eigensystem realization algorithm. *Journal of Guidance, Control, and Dynamics*, 9(3):294–303, 1986.

DISTRIBUTION A: Distribution approved for public release.

- [74] J. N. Juang, M. Phan, L. G. Horta, and R. W. Longman. Identification of observer/Kalman filter Markov parameters: Theory and experiments. Technical Memorandum 104069, NASA, 1991.
- [75] Jer-Nan Juang, JE Cooper, and JR Wright. An eigensystem realization algorithm using data correlations (era/dc) for modal parameter identification. *Control-Theory and Advanced Technology*, 4(1):5–14, 1988.
- [76] Fabien Juliet, BJ McKeon, and Peter J Schmid. Experimental control of natural perturbations in channel flow. *Journal of Fluid Mechanics*, 752:296–309, 2014.
- [77] Eurika Kaiser, Bernd R Noack, Laurent Cordier, Andreas Spohn, Marc Segond, Markus Abel, Guillaume Daviller, Jan Östh, Siniša Krajnović, and Robert K Niven. Cluster-based reduced-order modelling of a mixing layer. *Journal of Fluid Mechanics*, 754:365–414, 2014.
- [78] Rudolph Emil Kalman. A new approach to linear filtering and prediction problems. *Journal of Fluids Engineering*, 82(1):35–45, 1960.
- [79] S. M. Kaplan, A. Altman, and M. Ol. Wake vorticity measurements for low aspect ratio wings at low Reynolds number. *Journal of Aircraft*, 44(1):241–251, 2007.
- [80] Dong-Ha Kim and Jo-Won Chang. Unsteady boundary layer for a pitching airfoil at low Reynolds numbers. *Journal of mechanical science and technology*, 24(1):429–440, 2010.
- [81] Bernard O Koopman. Hamiltonian systems and transformation in hilbert space. *Proceedings of the National Academy of Sciences of the United States of America*, 17(5):315, 1931.
- [82] Sun-Yuan Kung. A new identification and model reduction algorithm via singular value decomposition. In *Proceedings of the 12th Asilomar conference on circuits, systems and computers*, Pacific Grove, pages 705–714, 1978.
- [83] Jae Hwa Lee, Abu Seena, Seung hyun Lee, and Hyung Jin Sung. Turbulent boundary layers over rod- and cube-roughened walls. *Journal of Turbulence*, 13:N40, 2012. doi: 10.1080/14685248.2012.716157. URL <http://dx.doi.org/10.1080/14685248.2012.716157>.
- [84] DM Luchtenburg, BR Noack, and M Schlegel. An introduction to the POD Galerkin method for fluid flows with analytical examples and matlab source codes. *Berlin Institute of Technology MB1, Müller-Breslau-Strabe*, 11, 2009.
- [85] David J Lucia, Philip S Beran, and Walter A Silva. Aeroelastic system development using proper orthogonal decomposition and volterra theory. *Journal of aircraft*, 42(2):509–518, 2005.
- [86] John L Lumley. *Stochastic tools in turbulence*. Courier Dover Publications, 2007.
- [87] WJ McCroskey. Unsteady airfoils. *Annual review of fluid mechanics*, 14(1):285–311, 1982.
- [88] Igor Mezić. Spectral properties of dynamical systems, model reduction and decompositions. *Nonlinear Dynamics*, 41(1-3):309–325, 2005.
- [89] Igor Mezić. Analysis of fluid flows via spectral properties of the Koopman operator. *Annual Review of Fluid Mechanics*, 45:357–378, 2013.

DISTRIBUTION A: Distribution approved for public release.

- [90] Michele Milano and Morteza Gharib. Uncovering the physics of flapping flat plates with artificial evolution. *Journal of Fluid Mechanics*, 534:403–409, 2005.
- [91] Jeff Moehlis, TR Smith, Philip Holmes, and H Faisst. Models for turbulent plane couette flow using the proper orthogonal decomposition. *Physics of Fluids (1994-present)*, 14(7):2493–2507, 2002.
- [92] Arvind T. Mohan, Miguel R. Visbal, and Datta V. Gaitonde. *Model Reduction and Analysis of Deep Dynamic Stall on a Plunging Airfoil using Dynamic Mode Decomposition*. American Institute of Aeronautics and Astronautics, 2015/11/29 2015. doi: doi:10.2514/6.2015-1058. URL <http://dx.doi.org/10.2514/6.2015-1058>.
- [93] Tomas W Muld, Gunilla Efraimsson, and Dan S Henningson. Flow structures around a high-speed train extracted using proper orthogonal decomposition and dynamic mode decomposition. *Computers & Fluids*, 57:87–97, 2012.
- [94] Nathan E Murray and Lawrence S Ukeiley. Modified quadratic stochastic estimation of resonating subsonic cavity flow. *Journal of Turbulence*, 8:N53, 2007.
- [95] B. R. Noack, K. Afanasiev, M. Morzynski, G. Tadmor, and F. Thiele. A hierarchy of low-dimensional models for the transient and post-transient cylinder wake. *Journal of Fluid Mechanics*, 497:335–363, 2003.
- [96] Bernd R Noack and Helmut Eckelmann. A global stability analysis of the steady and periodic cylinder wake. *Journal of Fluid Mechanics*, 270:297–330, 1994.
- [97] Bernd R Noack, Marek Morzynski, and Gilead Tadmor. *Reduced-order modelling for flow control*, volume 528. Springer Science & Business Media, 2011.
- [98] Bernd R Noack, Witold Stankiewicz, Marek Morzynski, and Peter J Schmid. Recursive dynamic mode decomposition of a transient cylinder wake. *arXiv preprint arXiv:1511.06876*, 2015.
- [99] Jan Östh, Bernd R Noack, Siniša Krajnović, Diogo Barros, and Jacques Boré. On the need for a nonlinear subscale turbulence term in POD models as exemplified for a high-reynolds-number flow over an ahmed body. *Journal of Fluid Mechanics*, 747:518–544, 2014.
- [100] Chong Pan, Dongsheng Yu, and Jinjun Wang. Dynamical mode decomposition of gurney flap wake flow. *Theoretical and Applied Mechanics Letters*, 1(1):012002, 2011.
- [101] Chong Pan, Dong Xue, and Jinjun Wang. On the accuracy of dynamic mode decomposition in estimating instability of wave packet. *Experiments in Fluids*, 56(8):1–15, 2015.
- [102] Laurent Perret, Erwan Collin, and Joël Delville. Polynomial identification of POD based low-order dynamical system. *Journal of Turbulence*, 7:N17, 2006.
- [103] Bérengère Podvin. A proper-orthogonal-decomposition-based model for the wall layer of a turbulent channel flow. *Physics of Fluids (1994-present)*, 21(1):015111, 2009.
- [104] R. J. Praznica, P. H. Reisenthel, A. J. Kurdila, and M. J. Brenner. Volterra kernel extrapolation for modeling nonlinear aeroelastic systems at novel flight conditions. *Journal of Aircraft*, 44(1):149–162, 2007.

DISTRIBUTION A: Distribution approved for public release.

- [105] Joshua L Proctor, Steven L Brunton, and J Nathan Kutz. Dynamic mode decomposition with control. *arXiv preprint arXiv:1409.6358*, 2014.
- [106] Joshua L Proctor, Steven L Brunton, and J Nathan Kutz. Dynamic mode decomposition with control. *SIAM Journal on Applied Dynamical Systems*, 15(1):142–161, 2016.
- [107] M Provansal, C Mathis, and L Boyer. Bénard-von kármán instability: transient and forced regimes. *Journal of Fluid Mechanics*, 182:1–22, 1987.
- [108] Stanislav Pyatykh, Jürgen Hesser, and Lei Zheng. Image noise level estimation by principal component analysis. *Image Processing, IEEE Transactions on*, 22(2):687–699, 2013.
- [109] S Joe Qin. An overview of subspace identification. *Computers & chemical engineering*, 30(10):1502–1513, 2006.
- [110] Mojtaba Rajaei, Sture KF Karlsson, and Lawrence Sirovich. Low-dimensional description of free-shear-flow coherent structures and their dynamical behaviour. *Journal of Fluid Mechanics*, 258:1–29, 1994.
- [111] Dietmar Rempfer and Hermann F Fasel. Dynamics of three-dimensional coherent structures in a flat-plate boundary layer. *Journal of Fluid Mechanics*, 275:257–283, 1994.
- [112] C. W. Rowley. Model reduction for fluids using balanced proper orthogonal decomposition. *International Journal of Bifurcation and Chaos*, 15(3):997–1013, 2005.
- [113] Clarence W. Rowley and Scott T.M. Dawson. Model reduction for flow analysis and control. *Annual Review of Fluid Mechanics*, 49(1), 2017. doi: 10.1146/annurev-fluid-010816-060042. URL <http://www.annualreviews.org/doi/abs/10.1146/annurev-fluid-010816-060042>.
- [114] Clarence W Rowley and Jerrold E Marsden. Reconstruction equations and the Karhunen–Loève expansion for systems with symmetry. *Physica D: Nonlinear Phenomena*, 142(1):1–19, 2000.
- [115] Clarence W Rowley and David R Williams. Dynamics and control of high-reynolds-number flow over open cavities. *Annu. Rev. Fluid Mech.*, 38:251–276, 2006.
- [116] Clarence W Rowley, Tim Colonius, and Richard M Murray. Dynamical models for control of cavity oscillations. *AIAA paper*, 2126(2001):2126–34, 2001.
- [117] Clarence W Rowley, Ioannis G Kevrekidis, Jerrold E Marsden, and Kurt Lust. Reduction and reconstruction for self-similar dynamical systems. *Nonlinearity*, 16(4):1257, 2003.
- [118] Clarence W Rowley, Tim Colonius, and Richard M Murray. Model reduction for compressible flows using POD and Galerkin projection. *Physica D: Nonlinear Phenomena*, 189(1):115–129, 2004.
- [119] Clarence W Rowley, Igor Mezić, Shervin Bagheri, Philipp Schlatter, and Dan S Henningson. Spectral analysis of nonlinear flows. *Journal of Fluid Mechanics*, 641(1):115–127, 2009.
- [120] S. P. Sane. The aerodynamics of insect flight. *The Journal of Experimental Biology*, 206(23): 4191–4208, 2003.

DISTRIBUTION A: Distribution approved for public release.

- [121] Turgot Sarpkaya. Vortex-induced oscillations: a selective review. *Journal of Applied Mechanics*, 46(2):241–258, 1979.
- [122] Taraneh Sayadi and Peter J Schmid. Parallel data-driven decomposition algorithm for large-scale datasets: with application to transitional boundary layers. *Theoretical and Computational Fluid Dynamics*, pages 1–14, 2016.
- [123] Taraneh Sayadi, Peter J. Schmid, Joseph W. Nichols, and Parviz Moin. Reduced-order representation of near-wall structures in the late transitional boundary layer. *Journal of Fluid Mechanics*, 748:278–301, 6 2014. ISSN 1469-7645. doi: 10.1017/jfm.2014.184. URL http://journals.cambridge.org/article_S0022112014001840.
- [124] Taraneh Sayadi, Peter J Schmid, Franck Richecoeur, and Daniel Durox. Parametrized data-driven decomposition for bifurcation analysis, with application to thermo-acoustically unstable systems. *Physics of Fluids (1994-present)*, 27(3):037102, 2015.
- [125] P. J. Schmid and J. Sesterhenn. Dynamic mode decomposition of numerical and experimental data. In *61st Annual Meeting of the APS Division of Fluid Dynamics*. American Physical Society, 2008.
- [126] Peter J Schmid. Dynamic mode decomposition of numerical and experimental data. *Journal of Fluid Mechanics*, 656:5–28, 2010. ISSN 1469-7645. doi: 10.1017/S0022112010001217. URL http://journals.cambridge.org/article_S0022112010001217.
- [127] Peter J Schmid. Application of the dynamic mode decomposition to experimental data. *Experiments in fluids*, 50(4):1123–1130, 2011.
- [128] PJ Schmid, L Li, MP Juniper, and O Pust. Applications of the dynamic mode decomposition. *Theoretical and Computational Fluid Dynamics*, 25(1-4):249–259, 2011.
- [129] Abu Seena and Hyung Jin Sung. Dynamic mode decomposition of turbulent cavity flows for self-sustained oscillations. *International Journal of Heat and Fluid Flow*, 32(6):1098–1110, 2011.
- [130] Jeff S Shamma and Michael Athans. Gain scheduling: potential hazards and possible remedies. *IEEE Control Systems Magazine*, 12(3):101–107, 1992.
- [131] C Shih, L Lourenco, L Van Dommelen, and A Krothapalli. Unsteady flow past an airfoil pitching at a constant rate. *AIAA journal*, 30(5):1153–1161, 1992.
- [132] W. A. Silva and R. E. Bartels. Development of reduced-order models for aeroelastic analysis and flutter prediction using the CFL3Dv6.0 code. *Journal of Fluids and Structures*, 19: 729–745, 2004.
- [133] A Singer and H-T Wu. Two-dimensional tomography from noisy projections taken at unknown random directions. *SIAM journal on imaging sciences*, 6(1):136, 2013.
- [134] Troy R Smith, Jeff Moehlis, and Philip Holmes. Low-dimensional modelling of turbulence using the proper orthogonal decomposition: a tutorial. *Nonlinear Dynamics*, 41(1-3):275–307, 2005.
- [135] KR Sreenivasan, PJ Strykowski, and DJ Olinger. Hopf bifurcation, landau equation, and vortex shedding behind circular cylinders. In *Forum on unsteady flow separation*, volume 1, pages 1–13, 1987.

DISTRIBUTION A: Distribution approved for public release.

- [136] R. F. Stengel. *Optimal Control and Estimation*. Dover, 1994.
- [137] GW Stewart. Perturbation theory for the singular value decomposition. in *SVD and Signal Processing, 11: Algorithms, Analysis and Applications*, 1991.
- [138] Michael Stewart. Perturbation of the svd in the presence of small singular values. *Linear algebra and its applications*, 419(1):53–77, 2006.
- [139] K. Taira and T. Colonius. The immersed boundary method: a projection approach. *Journal of Computational Physics*, 225(2):2118–2137, 2007.
- [140] K. Taira and T. Colonius. Three-dimensional flows around low-aspect-ratio flat-plate wings at low Reynolds numbers. *Journal of Fluid Mechanics*, 623:187–207, 2009.
- [141] Terence Tao and Van Vu. Random covariance matrices: Universality of local statistics of eigenvalues. *The Annals of Probability*, 40(3):1285–1315, 2012.
- [142] T. Theodorsen. General theory of aerodynamic instability and the mechanism of flutter. Technical Report 496, NACA, 1935.
- [143] Gilles Tissot, Laurent Cordier, Nicolas Benard, and Bernd R Noack. Model reduction using dynamic mode decomposition. *Comptes Rendus Mécanique*, 342(6):410–416, 2014.
- [144] L. Tregidgo, Z Wang, and I Gursul. Frequency lock-in phenomenon for self-sustained roll oscillations of rectangular wings undergoing a forced periodic pitching motion. *Physics of Fluids (1994-present)*, 24(11):117101, 2012.
- [145] GS Triantafyllou, MS Triantafyllou, and MA Grosenbaugh. Optimal thrust development in oscillating foils with application to fish propulsion. *Journal of Fluids and Structures*, 7(2): 205–224, 1993.
- [146] MS Triantafyllou, GS Triantafyllou, and R Gopalkrishnan. Wake mechanics for thrust generation in oscillating foils. *Physics of Fluids A: Fluid Dynamics (1989-1993)*, 3(12):2835–2837, 1991.
- [147] Jonathan H Tu, Clarence W Rowley, Ehsan Aram, and Rajat Mittal. Koopman spectral analysis of separated flow over a finite-thickness flat plate with elliptical leading edge. In *49th AIAA Aerospace Sciences Meeting and Exhibit*, pages AIAA–Paper. AIAA, 2011.
- [148] Jonathan H Tu, Clarence W Rowley, J Nathan Kutz, and Jessica K Shang. Spectral analysis of fluid flows using sub-Nyquist-rate PIV data. *Experiments in Fluids*, 55(9):1–13, 2014.
- [149] Jonathan H Tu, Clarence W Rowley, Dirk M Luchtenburg, Steven L Brunton, and J Nathan Kutz. On dynamic mode decomposition: Theory and applications. *Journal of Computational Dynamics*, 1(2):391–421, 2014.
- [150] L Ukeiley, L Cordier, R Manceau, J Delville, M Glauser, and JP Bonnet. Examination of large-scale structures in a turbulent plane mixing layer. part 2. dynamical systems model. *Journal of Fluid Mechanics*, 441:67–108, 2001.
- [151] Michel Verhaegen and Patrick Dewilde. Subspace model identification part 1. the output-error state-space model identification class of algorithms. 56(5):1187–1210, 1992.

DISTRIBUTION A: Distribution approved for public release.

- [152] Mats Viberg. Subspace-based methods for the identification of linear time-invariant systems. *Automatica*, 31(12):1835–1851, 1995.
- [153] J. J. Videler, E. J. Samhuis, and G. D. E. Povel. Leading-edge vortex lifts swifts. *Science*, 306:1960–1962, 2004.
- [154] Miguel R Visbal and JS Shang. Investigation of the flow structure around a rapidly pitching airfoil. *AIAA journal*, 27(8):1044–1051, 1989.
- [155] H. Wagner. Über die Entstehung des dynamischen Auftriebes von Tragflügeln. *Zeitschrift für Angewandte Mathematic und Mechanik*, 5(1):17–35, 1925.
- [156] Z. J. Wang. Dissecting insect flight. *Annual Review of Fluid Mechanics*, 37:183–210, 2005.
- [157] Zhu Wang, Imran Akhtar, Jeff Borggaard, and Traian Iliescu. Two-level discretizations of nonlinear closure models for proper orthogonal decomposition. *Journal of Computational Physics*, 230(1):126–146, 2011.
- [158] Zhu Wang, Imran Akhtar, Jeff Borggaard, and Traian Iliescu. Proper orthogonal decomposition closure models for turbulent flows: a numerical comparison. *Computer Methods in Applied Mechanics and Engineering*, 237:10–26, 2012.
- [159] Matthew O Williams, Clarence W Rowley, and Ioannis G Kevrekidis. A kernel approach to data-driven koopman spectral analysis. *arXiv preprint arXiv:1411.2260*, 2014.
- [160] Matthew O Williams, Ioannis G Kevrekidis, and Clarence W. Rowley. A data-driven approximation of the Koopman operator: Extending dynamic mode decomposition. *Journal of Nonlinear Science*, pages 1–40, 2015. ISSN 0938-8974.
- [161] Matthew O Williams, Clarence W Rowley, and Ioannis G Kevrekidis. A kernel-based method for data-driven Koopman spectral analysis. *Journal of Computational Dynamics*, 2(2), 2015.
- [162] Matthew O. Williams, Maziar S. Hemati, Scott T. M. Dawson, I. G. Kevrekidis, and Clarence W. Rowley. Extending data-driven Koopman analysis to actuated systems. In *IFAC Symposium on Nonlinear Control Systems*, 2016.
- [163] Charles HK Williamson. Vortex dynamics in the cylinder wake. *Annual review of fluid mechanics*, 28(1):477–539, 1996.
- [164] A. Wynn, D. S. Pearson, B. Ganapathisubramani, and P. J. Goulart. Optimal mode decomposition for unsteady flows. *Journal of Fluid Mechanics*, 733:473–503, 2013. ISSN 1469-7645. doi: 10.1017/jfm.2013.426. URL http://journals.cambridge.org/article_S0022112013004266.
- [165] Serhiy Yarusevych, Pierre E Sullivan, and John G Kawall. Coherent structures in an airfoil boundary layer and wake at low reynolds numbers. *Physics of Fluids (1994-present)*, 18(4): 044101, 2006.
- [166] Serhiy Yarusevych, Pierre E Sullivan, and John G Kawall. On vortex shedding from an airfoil in low-reynolds-number flows. *Journal of Fluid Mechanics*, 632:245–271, 2009.
- [167] John Young and Joseph CS Lai. Vortex lock-in phenomenon in the wake of a plunging airfoil. *AIAA journal*, 45(2):485–490, 2007.

DISTRIBUTION A: Distribution approved for public release.

- [168] Mohamed Y Zakaria, Haithem E Taha, Muhammad R Hajj, and Ahmed A Hussein. Experimental-based unified unsteady nonlinear aerodynamic modeling for two-dimensional airfoils. In *33rd AIAA Applied Aerodynamics Conference*, page 3167, 2015.
- [169] Zhizhen Zhao and Amit Singer. Fourier-bessel rotational invariant eigenimages. *JOSA A*, 30(5):871–877, 2013.

DISTRIBUTION A: Distribution approved for public release.



Academy of Model Aeronautics

The Landing Area Penalty Rule

Gordy Stahl, GordySoar@aol.com

Since I have the DerbySoar coming up in a week or so, and I knew there were some AMA Rule changes, I figured I'd take a look. (Likely all you CD's are up to speed on the new rules but I was out of commission for a few months, so got behind).

<<https://www.modelaircraft.org/files/RCSOaring2017-2018final.pdf>> / <<http://tinyurl.com/ya6dqega>>

What I found was that CD's currently don't seem know the rules or are ignoring them. At a recent ALES event I flew, the CD said, "Touch yourself, zero landing, touch your timer or anyone else zero flight." That's wrong.

At another event I was not at, a pilot was in his landing spot retrieving his plane when another pilot flew over that pilot's landing spot, touching the retrieving pilot with his model, at which time that pilot claimed he was hindered and should be allowed a second landing attempt. That's wrong too. Regardless of where a person is on the flying field, any contact by a model will result in a zero flight score for the pilot.

I have copied/pasted the new rule below:

6.5.4. Landing area penalty rule | Academy of Model Aeronautics Competition Regulations | Radio Control Soaring | pp. 17-18:

“If the model aircraft touches either the competitor or his helper during the landing maneuver, no landing points will be given.”

Bet you guys didn't realize this one! Open season on timers!

“If the model aircraft touches any other person during the landing maneuver, no landing or flight points will be awarded for that round.”

This is where it gets kind of ugly....

Here's a for instance: A pilot's model touches any person on the field other than himself or his timer, regardless of the reason for the “touch,” it's a zero flight. Not a reflight or a second chance at a landing.

From what I could find and after asking the rules guys: There are no exceptions including no “CD discretion,” since it is a safety issue. It is the pilot's responsibility to avoid contact by his model with a person. It is not a “fair” rule... But it is THE AMA Rule.

To explain it in an extreme way: During a flight, a nut pulls a trampoline into the landing area and begins doing backflips. The pilots, on their way into the landing area must avoid making contact with guy by their models ...or receive a zero flight score.

(Common sense would dictate that it was unfair, and not the pilot's “fault,” but the rule says make contact with a person other than yourself or your timer, loose the flight.)

Here's another silly example:

A visitor's dog breaks loose, runs into the area where models are landing and the owner follows. Touch the owner with your model, receive a zero flight. Again, not fair, but the rule.

So:

If you got a zero flight for your model touching your timer during a landing or a launch, it was incorrect.

If you got a re-flight or re-land because your model touched a pilot retrieving his model, you got a score you didn't deserve. (Had you avoided the touch, you would have been correct in calling “hinder” for a re-flight.)

The Catch 22: If a CD decides to use his discretion to ignore the rules and a protest is filed with the AMA, that CD could lose his CD status. (I asked).

Gordy

From Fabien Gagné <fabien.gagne@saintremi.ca>

Thanks Gordy,

This situation just happened at one of our contests this weekend. The pilot slightly touched himself on the landing (he was standing too close to the pin). We gave him his flight time, but no landing points.

The rule is actually ill-written:

“If the model aircraft touches any other person during the landing maneuver, no landing OR flight points will be awarded for that round.”

If the rule would be to attribute zero to the pilot's round, semantically “and” would have been written. But it's an OR, open for interpretation. With an OR, my read is that it's up to the CD to decide WHICH of the flight score or landing score to award. We chose landing points = 0.

Since blocking the slide by a few inches does qualify as a big safety hindering, IMO the rule is not only badly written, it is also ill conceived relative to safety.

Fab



Slope Soaring Candidate

Northrop YA-9A

The Northrop YA-9A had its first flight at the end of May 1972. Designed as an attack aircraft, two prototypes were built. It was in competition with the Fairchild Republic YA-10. The YA-10 was chosen over the YA-9A in the Air Force competition, with the YA-10 going into service as the A-10 Thunderbolt II/Warhog.

The YA-9 was a high-wing monoplane of aluminum-alloy construction. Honeycomb internal structures and chemically milled skins were features. Two Lycoming YF102 engines were placed in nacelles on either side of the fuselage.

The aircraft had large vertical and horizontal stabilizers to improve stability in low-level flight. The split ailerons could be used as airbrakes and differential deployment could be used to yaw the aircraft without banking. This improved weapon aiming.

Following the fly-off with the YA-10, both YA-9 prototypes were provided to NASA for further flight testing. After being retired in April 1973, the engines were removed, but both prototypes were retained otherwise intact.

71-1367 is currently in a storage yard awaiting restoration at Edwards AFB, California.

71-1368 is on display at March Field Air Museum, March Air Reserve Base, California.

Specifications:

Length:	53' 6"	16.31 m
Height:	17' 10"	5.44 m
Wingspan:	57'	17.37 m



<https://media.defense.gov/2017/Jun/01/2001755807/-1/-1/0/170601-F-ZZ999-999.JPG>



https://upload.wikimedia.org/wikipedia/commons/c/c6/Northrop_A-9A_parked.jpg



<http://www.aereo.jor.br/wp-content/uploads/2010/01/A-9A-c.jpg>



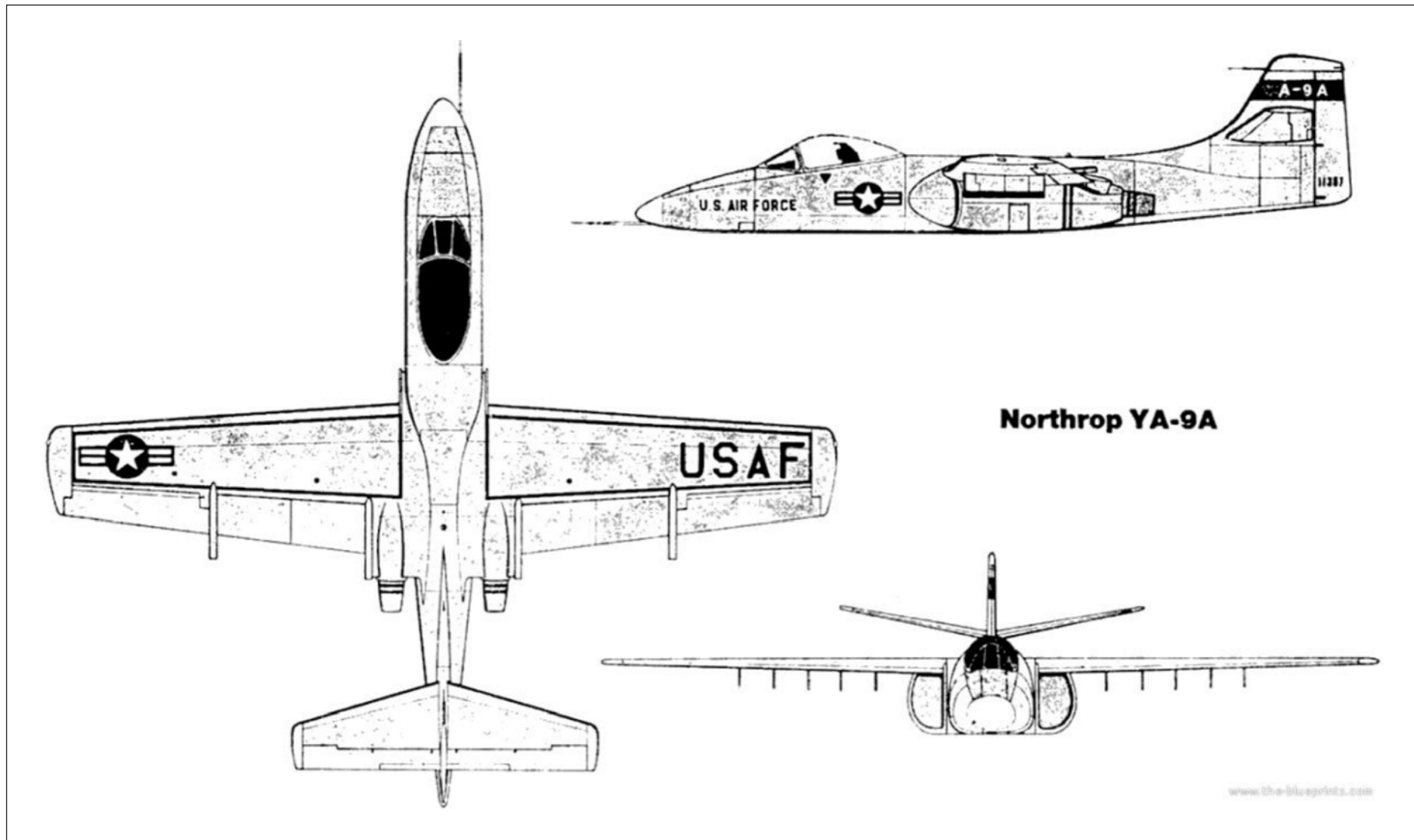
[https://upload.wikimedia.org/wikipedia/commons/8/8f/Desktop_folders/RCSD-2017-07/Northrop_YA-9A/*Northrop_YA-9A_'11368'_\(26683410563\).jpg](https://upload.wikimedia.org/wikipedia/commons/8/8f/Desktop_folders/RCSD-2017-07/Northrop_YA-9A/*Northrop_YA-9A_'11368'_(26683410563).jpg)



https://upload.wikimedia.org/wikipedia/commons/5/5e/Northrop_A-9A_prototype.jpg



https://upload.wikimedia.org/wikipedia/commons/c/cb/Northrop_A-9A_at_touchdown.jpg



https://www.the-blueprints.com/blueprints/modernplanes/northrop/75945/view/northrop_ya_9/

